Mehmet Doğancan Ecemiş

Strength Analysis of Membrane Structures for the Support of Future Solar Islands

Master's thesis in Marine Technology
Supervisor: Prof. Svein Sævik
Co-supervisors: Sr. Res. SC. Virgile Delhaye
                 Assoc. Prof. Yanlin Shao
June 2023

Norwegian University of Science and Technology
Technical University of Denmark
Nordic Master's in Maritime Engineering

NTNU
Norwegian University of
Science and Technology

DTU Technical
University of
Denmark

Abstract

The report provides a comprehensive overview of membrane materials, including their mechanical and structural properties, as well as their applications in various industries. It discusses the behavior of membrane structures and their response to hydrodynamic loads, while also exploring testing procedures. Membrane technology, known for its lightweight and customizable nature, emerges as a promising solution for achieving sustainable operations. The report emphasizes the importance of enhancing membrane performance and conducting strength analysis to support future solar island projects.

In the context of the Master's thesis, a computational model is developed to analyze membrane specimens using ABAQUS software. The thesis describes the experimental setup conducted at the SINTEF Material Laboratory and highlights the subsequent comparison between the computational model and real experiment results. By validating the model through empirical data, the thesis aims to provide a comprehensive understanding of membrane behavior and improve the accuracy of computational predictions.

Moving forward, the thesis focuses on expanding the strength analysis of membranes by incorporating detailed explanations and results from the real experiments. It highlights the significance of integrating experimental data to refine the computational models and enhance their predictive capabilities. The thesis serves as a valuable contribution to the existing literature on membrane structures and materials, offering insights into the mechanical behavior and performance of membranes under various loading conditions.

Additionally, the thesis presents the results of two different types of membrane experiments conducted in the laboratory. The first set of experiments focuses on uni-axial tensile tests, while the second set involves dynamic mechanical analysis experiments at varying stress rates within a specific frequency range. Calibration of the elastoplastic model required additional time due to the limited information available regarding the behavior within the thickness. Experimental and simulated results are compared to assess the computational model's accuracy and reliability in capturing membrane material behavior.

Together, the Master's thesis contribute to the understanding of membrane materials, their behavior under different loading conditions and the development of computational models for analyzing and predicting their mechanical response for the support of future solar islands.

Preface

This report constitutes my Master's thesis, completed in the spring semester of 2023 as part of the Nordic Master in Maritime Engineering program, specializing in the Ocean Structures track. It builds upon the project report I previously prepared for the Marine Structures Specialization Project (TMR 4500). The aim of this thesis is to expand upon and provide a analysis and evaluation of the research topic.

I am deeply grateful to my thesis supervisors, Professor Svein Sævik and Senior Research Scientist Virgile Delhaye, for their exceptional guidance, support, and insightful comments throughout the entire process of my thesis. Their expertise, mentorship, and dedication have been instrumental in shaping the quality and success of my research.

I would like to extend my heartfelt appreciation to my mother, Hülya Ecemiş, my father, Mahmut Ecemiş, and my sister, Makbule Doğa Ecemiş, for their constant love, encouragement, and unwavering support. Their presence in my life has been a constant source of strength and motivation.

Special thanks go to my uncle, Ecevit Kaya, for his invaluable help and support during this journey. His guidance and encouragement have been truly inspiring.

I would also like to express my sincere gratitude to İlayda Karayazı for her unwavering support, willingness to help, and positive influence. Her presence has brought joy and positivity to my life, and I am grateful for her constant encouragement, and I am immensely grateful for his presence in my life.

To everyone who has contributed to my academic and personal growth, I extend my heartfelt thanks. Your support has played an integral role in making this chapter of my life a truly enriching and rewarding experience.

<center>

Trondheim, June 2023

Mehmet Doğancan Ecemiş

</center>

Nomenclature

List of Abbreviations

$ASTM$	American Society for Testing and Materials
BC	Before Christ
DIC	Digital Image Correlation
DMA	Dynamic Mechanical Analysis
$DMTA$	Dynamical Mechanical Thermal Analysis
DP	Dynamic Positioning
$ETFE$	Ethylene Tetrafluoroethylene
FEM	Finite Element Method
FEP	Fluoroethylenepropylene
FPV	Floating Photovoltaic
$HDPE$	High Density Polyethylene
$MIRARCO$	Mining Innovation in Sudbury, Canada
PA	Nylon
PE	Polyethylene plastic

PET	Polyethylene terephthalate
PP	Polypropylene
$PTFE$	Polytetrafluoroethylene
PV	Photovoltaic
PVC	Polyvinyl Chloride
$PVDF$	Polyvinylidene fluoride
SLS	Service Limit State
SWL	Standing water level
TMS	Tensile Membrane Structure
TMS	Tensile Membrane Structures
ULS	Ultimate Limit State
$UMAT$	User Material
UTM	universal testing machine
UV	Ultraviolet
$VLFS$	Very Large Floating Structure
WEC	Wave Energy Converter

List of Symbols

$\bar{\varepsilon}_0^{pl}$	Initial value of the equivalent plastic strain
$\bar{\varepsilon}_f^{pl}$	The strain at failure
β	Reliability Index
$\dot{\varepsilon}$	Constant strain rate
η	Linear surface correction

γ_f	Partial factors 1
γ_L	Load factor
γ_M	Partial factors 2
γ_{stress}	Stress reduction coefficient
γ_t	Safety coefficient
λ	Wavelength
ν	Poisson's ratio
ω	Angular frequency
ω_d	Damage parameter
ρ	Density
σ	Stress
σ_t	True Stress
$\sigma_{\alpha\beta}$	The stress condition in a two-dimensional material
τ_{xy}	Shearing stress
ε	Strain
ε_t	True Strain
$\varepsilon_{\mu\nu}$	The second-rank tensor shear deformation
A	Elastic energy density
A_i	Cross Section of the member i
c^2	Speed of wave
D	Flexural rigidity
E	Young's Modulus

E'	Storage modulus
E''	Loss modulus
E^*	Complex modulus
$E_{\alpha\beta\mu\nu}$	A tensor describing the material property
f	Frequency
g	Gravitational constant
$G(t)$	Relaxation elastic modulus
H	Wave height
h	Water depth
h_t	Thickness of the plate
k	Angular wave number
k_e	Scaling factor
k_q	Quality factor
L_0	Initial length
L_t	Life cycle factor
M_{xy}	Moment of twisting
M_x	Moment of bending
$N_{x,y}$	Normal Forces
N_{xy}	Shearing force
$N_x ds_y$	Total force
p	Dynamic pressure
Q_x	Transverse force

r	Radius
T	Period
T	Wave period
T_C	Tensile force
T_D	Permissible strength
$tan\delta$	Loss factor
u	Velocity of horizontal water particle
v	Velocity of vertical water particle
$Y(t)$	Relaxation modulus matrix
$\Delta\bar{\varepsilon}^{pl}$	An increment of the equivalent plastic strain

List of Tables

List of Figures

Table of Contents

Chapter 1

Introduction

The world is changing rapidly with a continuous increase in population and energy consumption. People consume enormous amount of energy on daily basis. The increasing demand of energy needs to be compensated with the new technologies. Due to the fossil fuels pollution and the climate change, novel technologies are tend to be designed to obtain sustainable energy for a better world and satisfy the demand.

Those demands would be covered by development of new technologies and usage of sustainable energy sources. Over the past two decades, researches has been conducted in the field of sustainable energy including solar, hydropower, ocean and geothermal wind energy. The sustainable energy sources will keep producing renewable energy for future generations. Each type of these sustainable energy have their own qualification, demands and feasibility. Especially, the solar energy has several opportunities to produce energy.

The solar panels can be positioned on the land or the sea. The efficiency of the solar energy panels are differentiated by location. According to measured data from different locations which are located on the land in Netherlands and on the North Sea shows that the annual average energy output value is 13-18% higher on the sea [16]. According to the installation of solar panels procedures, it requires large space on the land which could also be fertile lands. Therefore, several new concepts are constituted for installation the solar panels on the sea such as offshore solar islands. The floating solar panels are placed on the reservoir or the lakes which are isolated from the sea for avoiding the significant wave effects on the structures. In consideration of the waves and current effects on the structures, the industrial applicability of the design is changing due to the different loads

influence.

In this report, a preliminary research and literature reviews are fulfilled for the membrane materials which are used in the concept of future solar islands.

1.1 Objective and Scope

This report gives an overall perspective of membrane structures which was used material behaviours, structural models which include combination of loads with preliminary models and the explanation of the experiment of the material selections.

Main objectives of the report can be summarised as below:

1. The membrane structures in general.

2. Develop preliminary strength analysis of the experimental setup with the help of the non-linear model in ABAQUS.

3. Perform a physical material experiments needed to evaluate suitable materials.

4. Investigate the effects of combinations of different loads on the membrane materials.

5. Determine the appropriate material behaviours from the different material testing in regards of suggested operational limits.

6. Suggest or\and unveil important parameters that may be needed for further investigation and material tests to improve and develop better solar islands.

Chapter 2

Background of The Membrane Structure

There are several different names of membrane structures such as tension membrane structures, tensile fabric structures, thin-shell structures, etc. All of these names indicate same type of light-weight structures which are based on fabric or\and metal materials. These structures contains a framework which could be steel or aluminium. Tensile membranes stretch on the frame structure.

2.1   Overall Perspective of Membrane Structures

Whichever structures built with the purpose of being light to a bare minimum for supporting the live loads. Almost on all structures, there are unnecessary but also necessary loads can be called as the dead loads. The ratio of the dead loads and the live loads should be small for lightweight structures such as tensile membrane structures [17].
The tensile membrane structures offer functional structural adjustment, economic viability and quick constructibility. They are built with the support of resistant elements such as beam, truss member, girder enduring the tensile loads. The load-carrying capacity of the used membrane materials depends on the shape and the surface geometry of the structure.
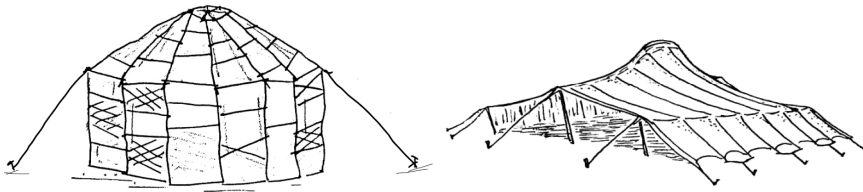
Figure 2.1: (a) Made of animal skin ; (b) Tent with internal and external supports.

2.2 History of the Membrane Structures

Membrane structures have been used for a long period since the ancient times. They were used for mostly safety purposes such as temporary shelter and sun shade [18]. The maidenhead of the membrane structures can be dated about 40.000 B.C. as a tent from the made of animal skins with the support of tree saplings in Figure 2.1(a). Over the years, the animal skins were replaced with woven fabric which are wool or canvas weaving. In regards of technological developments, modern materials are being taken into account such as steel, aluminum, polyester with supports of internal and external members 2.1(b) and complex fabrics. One of the important developers of steel lightweight building techniques was Vladimir Grigorevic Shukhov [19].

The industrial production processes develop day by day, producing fabric, rope or other membrane structure components is downhill all the way. Frei Otto was the leader of his time where the majority of tension structures were created in the late nineteenth century, and during the twentieth century, they were largely found in buildings [20]. Circus tents and the demand for larger structures with the advent of the industrial period were credited with the development of such structures in the early twentieth century [21]. However, compared to earlier tensile membrane constructions, modern ones are much more sophisticated in terms of design, construction method, and material characteristics. Tensile membranes are a well-liked option because of its shape flexibility, light weight, free flow, and appealing appearance. Application of tensile membrane has increased along with better materials, computer modeling tools and construction methods. Usage of tensile membrane, however, has not been utilized frequently when compared to other widely used materials, such as concrete or steel [18].

2.2.1 Fabrication

Tensile fabric constructions require huge clear span spaces to be manufactured because a single piece of the material might have a surface area of hundreds of square meters, unlike the materials of conventional building, brick and concrete.

One must go back to a knowledge of their physical qualities as produced by the modelling tools when thinking about the design and production of lightweight surfaces.

The details are what make a suitable solution for tensile membrane structures. The issue with the detailing occurs when the fabric or net meets the boundary system, which is often a lot more rigid and robust than the surface parts. The boundary element must be allowed to move independently of the surface or the stresses in the boundary region must be arranged such that they are consistent with the motions of the natural surface. Reduced surface wrinkling is crucial when a fabric surface is restricted at the edges by rigid components, such as cables or rigid structures. Surface wrinkling can cause the fabric to deteriorate over time [22].

The models are created using specialized FEM softwares based on the geometry needed by the static circumstances and/or desired project necessities. The tensile strength of the given material must first be evaluated prior to this. The expansion behaviour of the material employed must be assessed using biaxial testing. Obtaining official clearances and ensuring that the structure can be tensioned as planned after installation depend on this [23].

The most often used connecting method for textile membranes is sewing. However, there are already other bonding techniques available, including gluing, laser welding, and ultrasonic welding. All of these technologies have the benefit of being automatable [24]. The understanding of the processes for creating and joining materials, as well as their technical specification, is becoming increasingly crucial for the engineers. This is involved in design as a result of advancements in the creation of building materials and components. Therefore, the processes of manufacturing and erecting structures should be taken into consideration with being essential for the evolution of structural systems.

Welding

Radio frequency welding is used to connect the majority of exterior-use textiles and interior-use materials. This entails softening and joining the two layers of fabric together by heating the thermo-plastic element in the fabric coating using electromagnetic waves. The welds could be produced by an even strength over their whole length and a bond that can endure extraordinarily high tensile loads through the advanced welding technology.

The seam is intended to have the same tensile strength as the fabric itself. However, not all textiles can be welded readily, and a number of textiles need an additional layer of binding tape to guarantee a weld satisfying the strength and stability necessary for this kind of application [25].

Sewing

Industrial sewing machines are used to put layers of cloth together. The machines utilize UV stable thread for smaller projects and reinforce the patches on certain larger membranes.

Gluing

Welding or stitching are ineffective connecting methods for several applications and varieties of fabric membrane, including silicon coated glass cloth. Additionally, gluing with a high-bond glue will give a junction sufficient strength and endurance [24].

2.2.2   Structure of the Membrane Material

A tensile membrane's fabric, which is typically formed of woven or laid yarns, serves as its structural component. The yarns in cloth alternately go over and beneath one another. The illustration can be seen in Figure 2.2a. This weaving technique can be made with a single fibre or paired fibres. The yarns in a fabric illustration can be seen in Figure 2.2b. Also, for laid fabrics, the yarns are lapped on each others and bonded together with a third diagonal yarn. This third yarn do not have any structural purpose, just holding the fibres together. Each of these approaches have advantages and disadvantages according to area of utilization [19]. First PVC coated membrane was used in mid-sixties. Since the 1970s, this material has evolved into a standard for the tensile membrane systems [26].

The warp and fill directions of the membrane's tensile strengths must be identified. The strength of the material should be tested before using the material on the structure. The material can change the behaviour against the conditions of the environment.
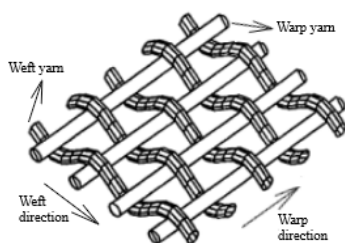
(a) Illustration of Yarn Weaving Process   **(b)** Illustration of Coated Fabric
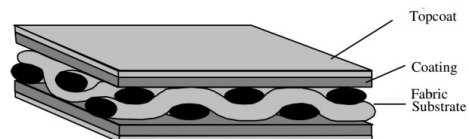
Figure 2.2: Reinforced Fabric

Figure 2.3 shows the membrane structure layers of silicon coated glass weave (2.3a) and coated polyester weave (2.3b). Except for glass, every one of these layers is a polymer. All these layers come together to offer the excellent characteristics that tensile membrane systems require. Membrane becomes solid and long-lasting form by covering up for each other's shortcomings. Without these components, it is impossible to think of a TMS.

(a) Silicon coated glass weave
(b) Coated polyester weave
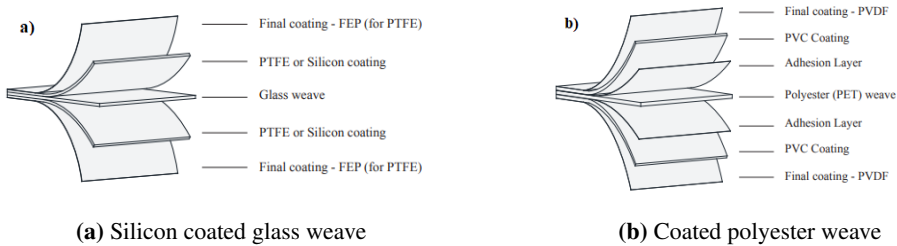
Figure 2.3: Layers of PTFE and PVC Membrane Materials

2.3   Design Standards of Membrane Structures

Consideration must be given to both strength and suitability when designing tensile membrane structures. TMS must be made to prevent an unproportional collapse or safety threat in case of membrane or its supporting elements failure. The support structure's designer must make sure that a local failure of the TMS does not result in the collapse of the TMS. Also, the support structure by either losing the capacity of the individual member of the support structure or by excessive movement of the TMS where the support structure depends on the TMS to provide stability to components or individual members of the support structure. The right circumstances should be provided to meet the structure's strength criteria. The material's life cycle modifies the member capacity involving aging effects formed by the environment or by wear and tear on membrane protective coatings. The life-cycle factor L_t should be chosen so that the member resistance is never less than what is specified by this standard at any point during the structure's planned service life. The metal part of the material should be chosen wisely without affecting each other against corrosion. According to the structural type, the load combinations also should be taken into account [27]. All these design requirements are related every membrane structures. Therefore, for specific usage area of membranes, there are several different points to take into consideration such as using membrane at fish farms.

While the recommended load combinations and the method of applying utilization factor vary between the various standards and guidelines, they may generally

be compared to the process stated in Equation 2.1 below, which adds the relevant coefficients and factors to the overall stress factor. The aforementioned standards concur on comparable "levels of uncertainty," which are reflected in the various stress variables. These standards can be also considered as the safety standards for testing for membrane structures. The allowable stress of membrane materials can be calculated with the Equation 2.1 [28]. Table 2.1 shows a schematic representation of these reducing strategies; in addition these three design standards guides are created in three different countries:

$$T_C \leq T_D = \frac{k_q \cdot k_e}{\gamma_t} \cdot T_{rm} = \frac{T_{rm}}{\gamma_{stress}} \tag{2.1}$$

Assuming typical values for the actions, the design strength T_D denotes the permitted strength that is finally evaluated against the estimated tensile force T_C under the specific load combination. The scaling factor k_e shows the elevated probability of critical defect with growing surface area; "the quality factor k_q shall adjust the member capacity to the execution quality. The separate factors (k_q, k_e, and γ_t) can be combined into one stress reduction coefficient γ_{stress} (often referred to as "stress factor") with respect to comparison, as shown in Equation 2.1.

The majority of these standards and recommendations are built on a stress factor method, which contrasts the findings of an analysis with typical loads to an allowable strength [1].

While designing an offshore fish farm to ensure that various standards' require-

Table 2.1: Different stress factor ranges among three different standards [1]

Standard	Symbol of factors	Included Factors	γ_{stress}
ASCE 55-16 [27]	L_t, β	life cycle factor and strength reduction based on various load combinations	4.0-7.8
ITBTP Design Guide [29]	γ_t, k_e, k_q	environmental degradation, scale factor, execution quality	5.0-7.0
DIN 4134 [30]	γ_f, γ_M, A_i	temperature, test scaling, time impact, environment deterioration, loading uncertainty	2.9-6.4

ments are satisfied in a consistent manner and also should be preserved in fish welfare. In order to account for the extremely flexible structures interacting with fluid forces in a hydroelastic way; linearized techniques are inapplicable because typical fish farm structures deflect too much when confronted to wave and current loads. These hydrodynamics effects should be taken into consideration. Hence, for a fish farm, the mooring loads of the fish farm are also important while calculating the loads. The membranes on the sea are facing a more tougher conditions than the membranes on the land. Thus, the design standards are became comprehensive for the membranes which are used in tougher environment [31].

Chapter 3

Offshore Applications

Tensile membranes are being used in various areas for offshore applications such as floating solar islands, aquaculture applications, inflatable structures which are used for gas storage, and wave energy converters which have flexible body such as attenuator, point absorber, etc. All these applications need high tensile membrane strength to resist wave load and environmental conditions.

In the past years, tensile membrane structures' development was taking into consideration, because of its appealing qualities, such as low cost, quick assembly, mobility, and effectiveness in handling environmental stresses through direct tensile stress without bending. However, several drawbacks including the potential for high deflections, stress concentrations balance out these advantages [32].

In order to prevent the marine structures from damage caused by rough seas, researchers have been working for years to create a reliable type of wave absorber that is also flexible, affordable, ecologically friendly, reusable, swiftly deployed, and durable. Along with its primary use in defending coastal shorelines, floating breakwaters can also be used to preserve aquaculture facilities [4].

3.1   Form of the Membrane Structures

The membrane material can be used on every type of structures. Membrane structures are mostly used in civil engineering industry. Also, the circular shape, rectangular shape, porous and net-type membranes are used on the marine structures. These membrane types will be mentioned on the following pages in different offshore applications.

3.1.1 Membrane on Circular Geometry

This type of membrane geometry is used on the aquaculture cages mostly. There is also one circular floating PV system which was designed by Ocean Sun in Figure 3.1. It is not on the sea but at the Banja reservoir in Albania. So, this is kind of prototype for future solar island which will be made from thin membrane materials. The membrane geometry is circular but the material of the membrane is changing according to environmental conditions and types of fish which are breeded inside the cages for the fish farms.
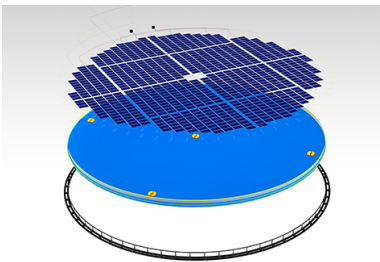
(a) The layers of the Solar Island

(b) The Solar Island on the Sea

Figure 3.1: Ocean Sun Floating Solar Island[Credit:Ocean Sun]

Circular geometry is chosen for offshore seas applications, as seen in Figure 3.2. The circular cages can be wider and they are more durable against the higher waves. The smaller rectangular type of fish farms are also used for offshore applications but the cages need to be smaller than the circular ones. That's why, the rectangular cage applications are not common in the industry. The fish farms are mostly made from the nets and other porous membranes. These nets types depend on the environmental conditions but without tracing the extra weight. Some fish farms have copper-alloy net cage system instead of lighter nylon or synthetic fiber net material cages. Also, the membrane materials are used on the closed cage fish farms.

3.1.2 Membrane on Rectangular Geometry

This type of membrane geometry is used on the aquaculture cages closer to the shore and floating solar islands made from thin film membranes. Also, in the rectangular cages. The permeability of the net cages are also important to resist environmental loads and wave forces. The flow goes through nets and the flexibility also allows the net to fluctuate under current forces. Rectangular fish farm
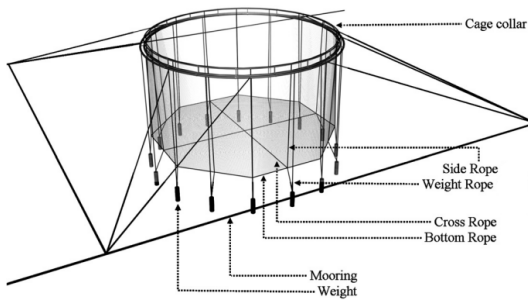
(a) Most common type of Circular Cage [33]   **(b)** Floating Farm with Collar[31]

Figure 3.2: Circular Floating Fish Farm
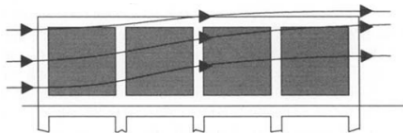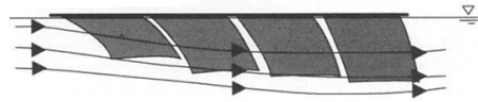
(a) Top View   **(b)** Side View

Figure 3.3: Illustration of the Rectangular Fish Cage [3]

behaviour under external current loads can be seen in figure 3.3b. Changing shape under the loads also helps to survive the structure under tough conditions [3].

There are various prototypes of rectangular floating solar panels around the world. Using thin film as a solar panel can be easy to install and maintain however the material resistance against the environmental load needs to be developed under sea conditions. Figure 3.4a shows the floating thin film PV system which was built by MIRARCO. In Figure 3.4b, the submersible floating solar island was designed by Prof. Marco Rosa Clot. The concept design shows the membrane solar panel is supported with the floaters [9].

3.1.3 Porous Membranes and Net-type Structures

Porous membranes and nets have recently received a lot of attention as a viable option because of their advantages over rigid and nonporous types of structures. This is because the porosity of the structure assistance in the dissipation of a significant amount of energy obtained from wave motions for shore protection works. The fact that fish farming likewise uses net-like structures and water within fish cages is significantly calmer than the water outside fishnets, demonstrating that porous membranes can provide tranquillity zone for fish farming [4].

The shape and material type of the nets can be vary. Several net types can be seen
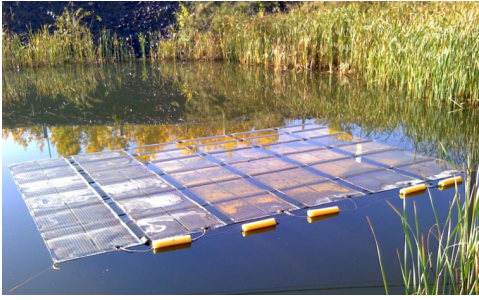
(a) Floating PV Prototype by MIRARCO
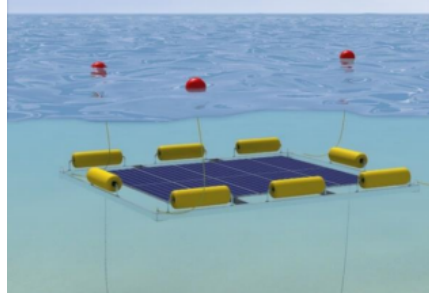
(b) Submersible Floating PV

Figure 3.4: Prototypes of Floating PV Islands

in Figure 3.5. Choosing a material for net-cage system, material bonding and anti fouling properties are taken into account. The polyester can not resist highest level of breaking loads but it has strong elongation at break. It also has longer time of life against the other material types. On the other hand, the nylon is lighter than the polyester. More weight on the structure also increases the working load, therefore nylon has better elongation at break but in long time use polyester is more effective. Also, for HDPE net type, the fouling is less than the other net types because it contains fewer fibres than the other. So, the fouling can not stick to the net [34].
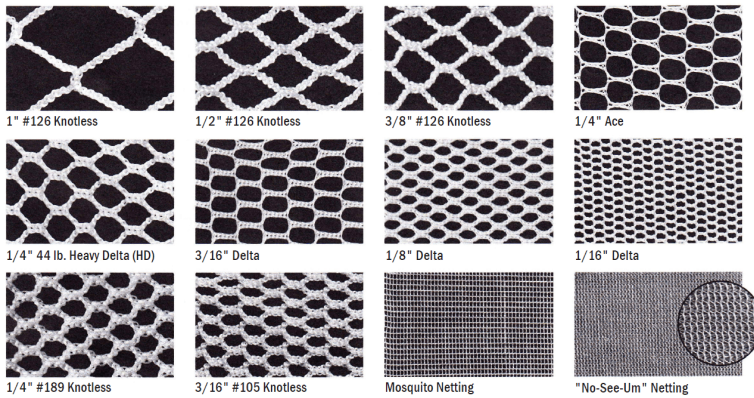
Figure 3.5: Different types of fish nets [4]

3.2   Applications of Membrane on the Water

There are several applications of membranes on the sea such as fish farms, floating solar islands, WEC prototype devices, inflatable structures. For the WEC proto-

types, these devices have been used just for creating new renewable resources and also to see the probability of working. WEC prototypes have not been used yet as a real project. Apart from solar and wind energy, wave energy can be used to produce $10\% - 20\%$ of the world energy supply. Global practices of these prototypes in the UK, the USA, France, Australia are seen in Figure 3.6. All these WEC prototypes contain flexible membrane on their specific parts [5]. In addition, the

Anaconda (Towing Tank, Solent University, UK)
(a)

AWS-III Cassette Structure (Orkney, UK)
(b)

M3 Wave DMP (Oregon, USA)
(c)

Bombora mWave (Model Test Basin, AMC, Australia)
(d)

Poly-A-OWC (FloWave Ocean Energy Research Facility, UK)
(e)

SBM S3 (Ecole Centrale de Nantes, France)
(f)

Wave Carpet (Berkeley TAFLab, University of California, USA)
(g)

SQ1 (Plymouth COAST Laboratory, UK)
(h)

Circular Sea-Clam (Loch Ness, UK)
(i)

Figure 3.6: Different WEC Prototype Types All Around the World [5]

use of inflatable structures is restricted to narrow spans and small radius of curvature. Temporary or permanent enclosure in the utilization of inflatable membrane structures are promising advances in the field of underwater building technology. The fundamental benefit of using these structures in a fluid environment is that the stresses imposed by the environment are effectively borne by direct tensile stress without the need of bending moment. The internal pressurized gas, a component of the habitable environment itself, serves as the main load-bearing mechanism. As a result of their light weight and collapsible design, they are easy in transportation and mounting [32].

Also, flexible porous membranes can be utilized as floating or submerged breakwa-

ters dissipating wave energy to protect from wave action since they are lightweight, recyclable, affordable, environmentally friendly, and don't hinder ocean waves. In addition to this, it has an importance in using horizontal flexible porous structures for preserving coastal infrastructures and fish farming to offer a calm atmosphere in coastal zones due to the growth in marine and human activities [6]. The membranes are used both vertically and horizontally, seen in Figure 3.7. Besides these applications, detailed explanations of floating solar islands and several aquaculture applications are hereinbelow.
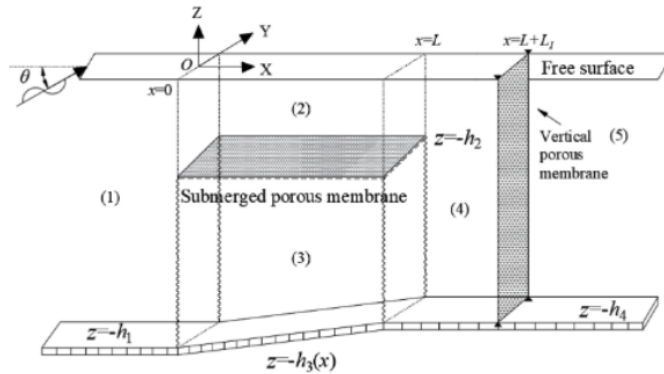
Figure 3.7: Illustration of the Submerged Membrane Breakwater [6]

3.2.1 Floating Solar Islands

The production of photovoltaic electricity has escalated in the last several years, and it is seen to be one of the most important methods for achieving carbon neutrality. PV consumes a lot of space and has a low power density, which may prevent further growth. As a result, installing PV on water has developed as an intriguing alternative site strategy [7].

There are several types of offshore solar systems all around the world such as fixed pile-based PV systems, wave proof PV systems, floating platform PV sytems, floating thin film PV systems. Just floating thin film PV systems contains membranes on its structure, but also wave proof PV system can be built with membrane structure. The two systems are explained below:

Wave Proof Floating PV Systems

Floating PV provides greater potentials than fixed piled PV, which is far more expensive and challenging to construct in deeper areas, particularly in areas of

high population density and limited accessible land. Due to the shadowing effect of the PV panels, floating PV could be applied to decrease the rate of evaporation. Additionally modular, floating PV makes installation simpler and quicker. Floating PV is more suited to offshore situations. Figure 3.8a shows the main parts of a typical floating PV system. To preserve offshore PV waters, breakwaters which
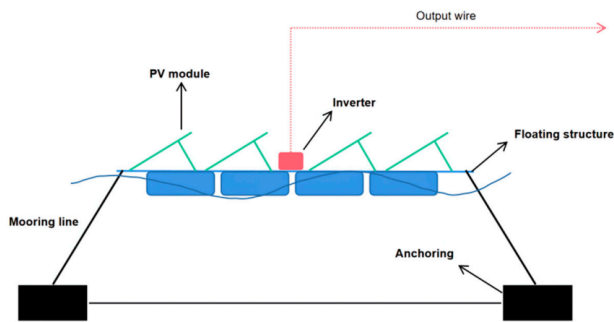
(a) Main Parts of Floating PV System
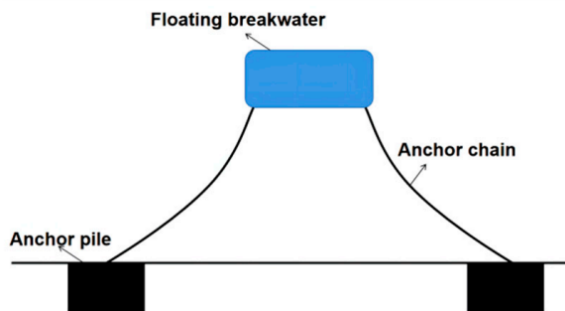
(b) Floating wave breaker

Figure 3.8: Demonstration of Wave Proof Floating PV System [7]

is shown in Figure 3.8b and other wave-attenuating structures must be built. To guard the PV modules, floating breakwaters are placed all around the PV platform. More than 50% of the waves can be blocked at once by various types of floating breakwaters.

Floating Thin Film PV Systems

A floating thin-film photovoltaic system has been presented by Norwegian Ocean Sun that carrying the customized PV modules on a thin polymer membrane that is mounted on a circular floater. The membrane system does not affect the water's surroundings and has a longer lifespan than the other systems [7]. The parts of the floating thin film PV system are shown in Figure 3.9a below.

(a) The layers of the Thin Film [7]   (b) Thin Film PV Concept Design [9]
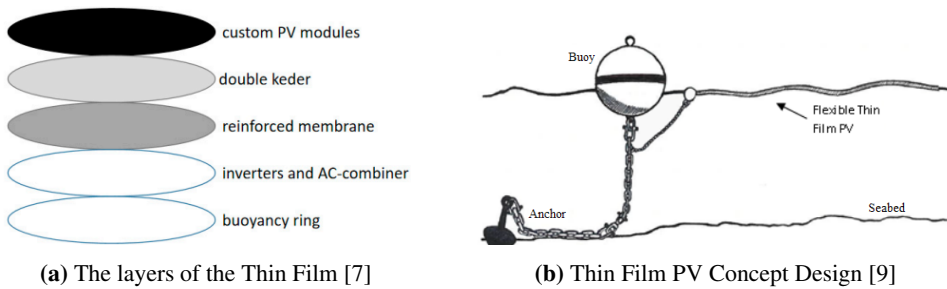
Figure 3.9: Floating Thin Film PV

It is a system with a number of advantages due to its unique design. The system reduces the risk of vessel collision with help of the deformability and bendability features [8]. Additionally, the installation of the system in marine environments is simplified and time-efficient. The direct water cooling mechanism implemented in the system effectively dissipates heat from the membrane, ensuring optimal performance. Moreover, the flexible body of the system exhibits remarkable strength, enabling it to withstand various environmental impacts. These advantages, as highlighted in a review by Wang et al. [7], contribute to the appeal and viability of thin film photovoltaic panels over traditional silicon solar panels.

Thin film photovoltaic panels offer numerous benefits compared to their silicon counterparts. Notably, they are lighter in weight and feature a simplified design with fewer components, enhancing their overall dependability. These panels also demonstrate exceptional safety even in collision scenarios and eliminate the need for a pontoon structure. Furthermore, their flexibility provides additional advantages in system integration and installation. Overall, the utilization of thin film photovoltaic panels represents a promising and efficient approach to harnessing solar energy [35]. When compared to pontoon-based PV systems, thin film-based FPV has less energy absorption per unit area and lacks the ability to align panels for maximum radiation, which is an additional advantage in self-cooling and self-cleaning of the PV panel [36] [37].

Thin film FPV is an excellent option for distant places with substantial installation, such as offshore installations. It is crucial to take into account during the design phase of offshore FPV projects the external environmental influences acting on the PV array. Figure 3.10 depicts the main environmental forces on the thin Photovoltaic film on the water. If the FPV system's mooring mechanism is pontoon-based, these forces will have a significant impact on it. Thin film solar
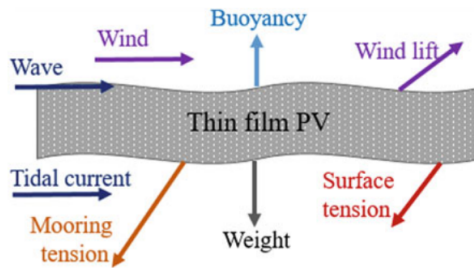
Figure 3.10: Influences on Thin Film PV System [8]

panels have absorbing layers 350 times thinner than silicon photovoltaics. Thinner layer makes the solar panel incredibly light, and the durability is also strongly maintained [8].

3.2.2 Aquaculture Applications

There are several types of cages on aquaculture applications. The buoyant collar or, in certain situations, a frame supports a floating cage. The owner can choose from a huge variety of sizes and shapes for floating cages, which is by far the most frequently used. In terms of site requirements, floating cages are likewise less constrained than the majority of other designs. Some floating models include rotatable designs to reduce fouling. The more popular non-rotating floating variants can have either wide or narrow collars built into them. The first type is typical in larger cages and is used as a work platform. Although some broad collars are flexible so they can be utilized in more exposed places, most wide collars are stiff in form. Rope and buoys can be used to create easy, affordable flexible-collar narrow cages [2]. The several types of aquaculture cages listed in Table 3.1.

Table 3.1: Aquaculture Cage Types [2]

Fixed	Floating					Submersible		Submerged
	Non-Rotating		Rotating			Suspended from surface	Adjustable Buoyancy	
	Wide Collar	Narrow Collar	With Central Axis	Without Central Axis		Rigid	Flexible	
Rigid Collar		Flexible Collar		Rotating by adjustment of float buoyancy	Rotating by adjustment of float position			
Rigid Bag	Flexible Bag							
	Net Floor	Solid Floor						

Closed Cage Fish Farms

Utilizing adaptable closed-cage technology, fish may grow from smolt to post-smolt stages before being harvested without risk of sea lice, death from predators,

or fish escape.

The closed cage system is more suitable for some types of fish such as salmon. In the closed cage, the current movement in the cage enables salmon exercise [38]. On the closed cage structures, flexible membranes, reinforced materials or concrete can be used. There are several types of membrane materials used on flexible cages.

(a) Flexible Closed Cage. Courtesy: Fi-iZK
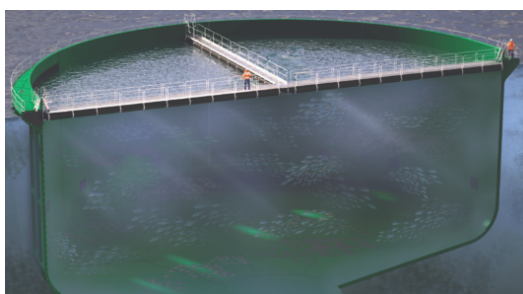
(b) Glass Fiber Reinforced Polyester Cage. Courtesy: CSUB

Figure 3.11: Closed Cage System Examples

All companies must follow the specific standards and guidelines for using different materials such as 'EN ISO 1421', 'EN ISO 2286-2' and 'DIN 53.363'. These standards specify the requirements of the the proper material such as strength, design rules, the conditions in particular environment. High quality membranes are used as flexible closed cage materials such as PVC-coated textile membranes, polyester fabric, cable woven into fabric reinforced textile membranes.

Open-Net Fish Farms

In the aquaculture application, the traditional way to produce fish is in open nets cages. The open-net provide clean water circulation when the current pass through the cage. There is no need in using water circulating pumps. On the other hand, open-net fish farms has low safety against the predators. Also, the net can break and it causes fish escaping. Diseases of fish can spread easily infecting other healthy fish [38].

The material types of the cage-net should be changed according to design requirements of the project. Polyethylene plastic (PE), High Density Polyethylene (HDPE), Polypropylene (PP), Nylon (PA) are most common net materials of the open-net cage system.

(a) Open-net Cage. Courtesy: Blue Farm   **(b)** Semi-submersible Open-net. Courtesy: SalMar

Figure 3.12: Open-net Cage Systems

3.2.3 Horizontal and Vertical Membrane Structures

Membranes are physically incapable of significantly growing under some stresses, such as those caused by bending, due to their thinness relative to their span. Membranes are consequently mostly impacted by tensile stresses, making them ideal as building materials since they primarily support tension pressures.

Typically the floating solar island use horizontally, membrane is basically laying on the top of sea, see in Figure 3.10. For the fish farms, in close-caged systems, the membrane is used vertically, as can be seen in Figure 3.11a. Therefore, it takes much more direct forces from the environmental loads.

There are several researches about the vertical membrane breakwater systems. The wave interaction, the reflection and transmission coefficients, wave forces are found and developed which are associated with the submerged porous membrane breakwater. Also, there are different experiments of three types of floating breakwaters which are made from porous membrane and mesh cage material. On the other hand, in the literature, little has been learned about how waves interact with a horizontal submerged flexible membrane that is utilized as a breakwater [6].

3.3 Hydrodynamic Loads

For the closed membrane fish farms, the net-cages, and other uses of membrane structures in the water, hydroelasticity can be a significant factor. Hydroelasticity means a interaction between the fluid and the flexible structure. It explains the impact of the body's structural response on the fluid surrounding the structure [31]. The structure on the sea is a highly intricate hydroelastic issue with several moving parts that interact with one another to affect how each part behaves.

Stronger currents and more intense waves will affect the fish farms. The size of the fish farms is also anticipated to grow. Large net deformations are a result of strong currents. The distortion of the net has a significant impact on the current forces. Additionally, a specific minimum volume within the fish cage is necessary for fish welfare. There are further problems that deserve attention. A trustworthy evaluation of the current and wave forces on the entire system is necessary for mooring line design. It is necessary to take into account the possibility of contact between the net and the chains or ropes supporting the bottom weights or the ring weight as wear and tear increases [39].

In order to acquire accurate estimates of extreme values in a stochastic sea, several realizations of a sea state are required. For a net-cage system, since there are really multiple net cages operating close together, it is unclear how the current and wave environment differs spatially and how the net cages interact hydrodynamically [31]. There are couple of principle loads on the floating cages, the forces are
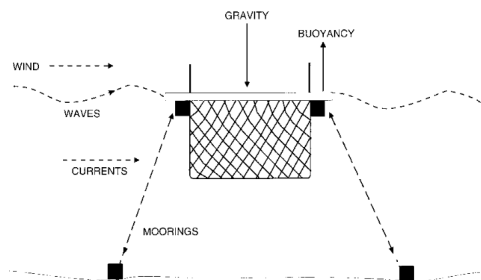
Figure 3.13: The Main Force Components on a Cage System. [2]

shown in Figure 3.13, also solid lines shows static forces, dashed line shows dynamic forces. While the mooring forces are responses, the wave, wind, and current forces may be seen as mostly horizontal loads placed on the cage collar. Similar to this, buoyancy forces may be seen as responses to gravity's imposed vertical load. The vertical loads tend to be static, whereas the horizontal loads are dynamic in nature, but the cage system's inertia and damping forces impose certain dynamic loadings in the vertical plane, particularly with regard to waves.

In various regions across the globe, the concept of deploying floating solar panels in large bodies of water, such as lakes, has already been implemented for offshore solar farms. This innovative approach allows for the integration of solar energy generation in open water environments. When conducting structural analyses and assessing environmental forces exerted by the water, it is essential to utilize the Linear Wave Theory. This theory enables the modeling of first-order, small-amplitude gravity waves, known as "airy waves," with sinusoidal shapes in deep water, thereby facilitating accurate analysis of wave dynamics [2].

A linear wave theory is essential for analysis offshore applications. To do this, it is necessary to provide the coordinate system and the variables that will be utilized to create the wave theories [40]. The coordinate system is shown in Figure 3.14 with x measured in the direction of wave propagation, and y measured upward from the ground surface. It is supposed that the waves are two-dimensional in the x-y plane and that they move continuously along an undisturbed route through water over a smooth horizontal bed [41].

Analytical formulations for the water particle's velocity, trajectories, accelera-
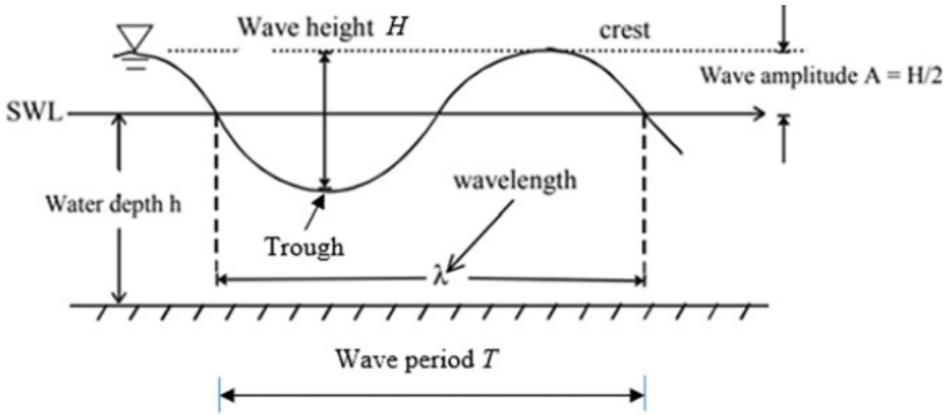
Figure 3.14: Characteristics of Linear Wave Theory

tions, and pressure are established based on this theory. A preliminary calculations are made to identify the fundamental properties of wave-induced water motion with the help of the Linear 'Airy' Wave Theory. The following equations represent an expression for the horizontal and vertical water particle velocities at (x, y) and time, t: The velocity of horizontal water particle, u:

$$u = \frac{\pi H}{T} \frac{\cosh ks}{\sinh kd} \cos(kx - \omega t) \tag{3.1}$$

The velocity of vertical water particle ν,

$$\nu = \frac{\pi H}{T} \frac{\sinh ks}{\sinh kd} \sin(kx - \omega t) \tag{3.2}$$

In linear dispersion, which is related to wave number and wave angular frequency:

$$\omega^2 = gk \tanh kd \tag{3.3}$$

with the help of linear dispersion, the speed of wave:

$$c^2 = \left(\frac{g}{k} \tanh kd\right) \tag{3.4}$$

For calculating the accelerations of the water particles in x and y directions, the second derivatives of Equations 3.1 and 3.2 is used:

$$\text{Horizontal} \longrightarrow u = \frac{\partial u}{\partial t} = \frac{2\pi^2 H}{T^2} \frac{\cosh ks}{\sinh kd} \cos(kx - \omega t)$$

$$\text{Vertical} \longrightarrow \nu = \frac{\partial \nu}{\partial t} = -\frac{2\pi^2 H}{T^2} \frac{\sinh ks}{\sinh kd} \cos(kx - \omega t) \tag{3.5}$$

The $y = d$ limit of the inherent assumption used to derive the linear airy wave theory prevents computations above the SWL (i.e., $y > d$). The linear surface correction, η provides a solution to this problem [40]:

$$\eta = \frac{H}{2} \cos(kx - \omega t) \tag{3.6}$$

Dynamic pressure, p also can be calculated as follow:

$$p = \rho g \frac{H}{2} \frac{\cosh ks}{\sinh kd} \cos \theta \tag{3.7}$$

On the other hand, for the floating thin membrane photovoltaic panels installation is challenging in open sea. The environmental loads are complicated for these thin panels. As can be seen in Figure 3.15, there are several environmental loads from wind, waves and currents. Researches are necessary to better understand how these thin floating platforms respond dynamically to environmental loads.

Larger solar panel systems are being considered for future advancements as poten-
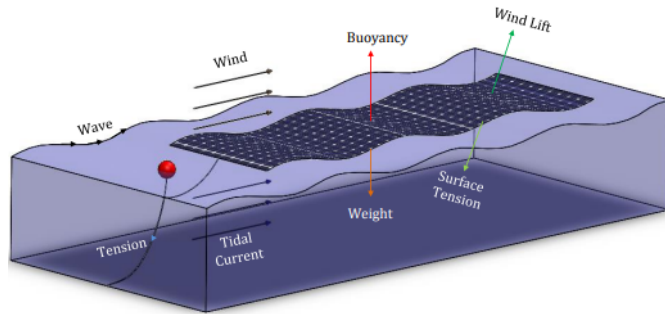
Figure 3.15: 3D Illustration of Forces on the Thin Film PV [9]

tial sites for the application of this technology. This would imply that the harsher sea wave conditions would subject such an equipment to greater stresses. The concepts suggested for such circumstances include inflexible traditional PV arrays that may be immersed in rough ocean conditions, or flexible thin film structures capable of undulating with the waves.

Due to the laminates' lack of flexural stiffness and lack of design to capture mechanical energy from the waves, the motion of a floating thin film PV array should not deviate considerably from that of the approaching waves. Any floating thin film array mooring system would only experience a little load as a result of the array, as will be explained [9].

3.3.1 Hydrodynamic Forces on Floating Thin Membrane PV

Trepani [9] gives the detailed explanation of the forces on the thin film PV arrays. The main reason for concentrating on the hydrodynamic of such floating constructions is the impact they have on the wave environment, which implies additional loading on the mooring systems as a result of these interactions. An analysis to support the floating thin film PV array's low-energy interaction with the waves. The flexural rigidity equation for a plate serves as the foundation for this methodology. The force pair needed to bend a non-rigid structure to a unit of curvature is known as the flexural rigidity, D.

$$D = \frac{E_y \cdot h_t^3}{12(1 - \nu^2)} \tag{3.8}$$

where E_y is the Young's Modulus for this equation and E indicates the bending energy, h_t is the thickness of the plate and ν is the Poisson's ratio of the membrane material.

If the array were moving in regular waves, this would suggest that the motion is sinusoidal. Therefore, the bending motion of the thin film PV array could be similar to a sinusoidal motion [42]. A factor of the force can be used to compute the energy taken from the waves or needed to bend the array when it modulates in response to approaching wave fronts:

$$E = \frac{L \cdot d}{\lambda} \cdot 2F \tag{3.9}$$

where,

$$F = \frac{D}{r} \left(\frac{\Theta}{360^o} \right) \tag{3.10}$$

and where L is the array's length, d is its breadth, λ is the wavelength of the waves, r is the sinusoidal wave curvature's radius, and θ is the curvature's angle. The following summary of the reduction in wave energy caused by the floating arrays can be derived from the combination of Equations 3.8, 3.9 and 3.10:

$$E = \frac{1}{6} \left(\frac{E_y \cdot h^3}{1 - \nu^2} \right) \left(\frac{L \cdot d}{\lambda \cdot r} \right) \left(\frac{\Theta}{360^o} \right) \tag{3.11}$$

The negligible impact of the floating thin film PVs on the wave environment is demonstrated, and it is predicted that their hydrodynamical motion will be nearly identical to that of the waves [9].

3.4 Failure Criteria

To confirm the changes in hydrodynamics, the dynamics of the demonstration should also be assessed and compared with those of the approaching waves. Determining dependability data for this sort of failure would be helpful because the mobility of the panels would ultimately lead to fatigue failures. Accelerated techniques can be used to complete fatigue failure testing, as is typical for mooring line reliability testing. This exposes the mooring system under test regularly and often to significant loading events that occur within a given year (apart from moderate environmental circumstances, which would have a reduced influence), allowing response to numerous years of harsh conditions to be characterized quickly [9].
Also, for all offshore renewable energy systems, including the unique offshore floating PVs as well as wave and tidal energy converters, failure of the station keeping system (i.e. mooring system or dynamic positioning system) via fatigue or excessive loading poses substantial design challenges. The main cause of mooring failure in wave energy converters is the large stresses that the device must endure in order to convert wave energy into mechanical power to operate the on-board generators [43]. The loads transmitted onto the mooring system may be noticeably reduced in an energy conversion system where the provision of the mechanical power is not necessary (as is the case with a solid state system like the floating PV), and consequently, the risk of station keeping system failure may be reduced accordingly [9].

3.4.1 Shear Failure

As it combines dynamic and shear stress conditions, the topic of dynamic shear failure of materials is fairly broad. The dynamic environment involves the formation and propagation of stress waves inside the structure (or specimen), therefore shear failure is to be regarded not only as a microscopic failure process but also from a macroscopic perspective [44].
Many materials, including the majority of metals, can deform at high strain rates when used with the shear model. It measures failure using the corresponding plastic strain. It can be used in conjunction with the Johnson-Cook plasticity model or the Mises model. Additionally, it can be applied along with the tensile failure model. The corresponding plastic strain value at the element integration points serves as the foundation for the shear failure model, which assumes failure when

the damage parameter reaches 1. The definition of the damage parameter, ω_d, is

$$\omega_d = \frac{\bar{\varepsilon}_0^{pl} + \sum \Delta \bar{\varepsilon}^{pl}}{\bar{\varepsilon}_f^{pl}} \qquad (3.12)$$

where, $\bar{\varepsilon}_0^{pl}$ indicates the initial value of the equivalent plastic strain, $\Delta \bar{\varepsilon}^{pl}$ indicates an increment of the equivalent plastic strain and $\bar{\varepsilon}_f^{pl}$ indicates the strain at failure, and the analysis's summation is carried out across all incremental steps .

The assumption is that the pressure-deviatoric stress ratio, $\frac{p}{q}$, (where q is the Mises stress and p is the stress of the pressure), temperature, and present field factors all affect the strain at failure, $\bar{\varepsilon}_f^{pl}$. The strain at failure can be described in two different ways. Using direct tabular data is one option, where the dependencies are provided in a tabular format. As an alternative, Johnson and Cook's analytical form can be used.

The strain at failure, must be presented as a tabular function of the equivalent plastic strain rate, the pressure-deviatoric stress ratio, temperature, and established field variables when direct tabular data are utilized to create the shear failure model. The Mises plasticity model must be applied in order to apply this strategy [45].

3.5 Challenges

Lightweight constructions push the limits of static and dynamic theory, achieving lightness is a difficult task. The sophisticated materials challenge the technology, and the intricate three-dimensional structures challenge the production processes [17]. Extreme out-of-plane flexibility, leaves membranes susceptible to wrinkle. It might be difficult to successfully get rid of wrinkles in a membrane. While cables tied to the edges are useful at preventing wrinkles, but they caused a weight gain. Designing a floating solar project to ensure buoyancy and structural integrity is the primary challenge [46] [47]. The offshore PV system is exposed to harsh sea conditions such as high humidity, salt fog, corrosion, lightning, and typhoons. Conventional inland water PV system technology is unsuitable for these conditions, posing potential risks [7].

Maintenance challenges in floating solar systems include microbial adhesion and salt deposition. The accumulation of algae, marine invertebrates, and other aquatic organisms on submerged structures can increase the risk of corrosion, affecting the overall stability and increasing operational and maintenance costs [48]. Additionally, the high salinity of seawater promotes the buildup of sea salt, accelerating the corrosion process on the structure's surface [49].

The installation of floating photovoltaic systems can affect the underwater environment by reducing the amount of sunlight reaching the water column, potentially impacting the growth of algae and aquatic life. The solar panels themselves may experience negative thermal drift due to lower humidity and temperature, resulting in reduced overall efficiency. Depending on the location, fishing and transportation activities may be affected. Moreover, the panels require waterproofing and lightweight materials, which can increase costs. Overall, offshore installation is more complex and expensive compared to land-based installations due to additional considerations [7].

The criteria used by the EU to assess the possibility of certain environmental problems are listed under the environmental impact assessment. These standards can be mentioned as distance from the shore D, the station keeping systems (mooring or DP), blocking to the PV panel $\frac{z}{d}$, blocking to the sea surface $\frac{w}{a}$ and power take off system; where the draft of the energy device shows with z, the water depth shows with d, the device area shows with w, and the solar floating farm footprint shows with a.

Floating solar plants are susceptible to stress and vibration issues caused by wind, waves, and external factors. Vibration-induced microcracks in the modules can reduce power output and lead to durability concerns. If the system is located near the shore, involving the public and relevant organizations in the planning phase is crucial to ensure public acceptance and approval.

Chapter 4

Materials Behaviour

The choice of membrane is a crucial decision in the entire design process since tensile membrane designs naturally have large membrane surfaces supported by light cables and stiff supports. The science of coatings and weaving has advanced significantly over the past 40 years, and today there are several possibilities for fabrics, coatings and polymers each with their own advantages and distinctive qualities [19].
Finding acceptable membrane materials that can withstand high tensile stresses is one of the issues with membrane constructions on the sea. When building low profile or long span membrane structures, cable reinforcement is extremely helpful. The right material choice and well constructed seams and joints have a significant role in the strength of membrane constructions. The anchoring, stabilizing strategies, transport, erection, safety, and maintenance of these structures are additional important factors that must be taken into account during the design process [32].

4.1 Properties of the Material Types

The types, amounts, processing forms, and orientation of the fibers utilized determine the load-bearing capability and stress distribution in fiber-reinforced polymers and textile membranes. The stiffness, or more precisely the elastic modulus, of a component—and consequently the alignment of the flow of forces—is determined by the orientation of the fibers. For instance, a larger stiffness can be anticipated in the fibers' longitudinal direction. The utilization of semi-finished textile items always takes the form of a composite, where they are coated with a thermoplastic material or encased in a polymeric resin. Together, the two elements

carry out various structural tasks. Under load, the protective polymer must not be overstretched since it could rip, leaving the fibers exposed to the elements. The strength and elastic modulus of synthetic fabrics and polymer fibers are directly influenced by the length of the fibers, temperature, and environmental conditions. However, when employing textile membranes and fiber-reinforced polymers, it is also crucial to take into account how the fibers and the polymer interact because, in contrast to other materials, the behavior of components with integral fibres is greatly influenced by load direction. Depending on the direction and density of the fibers, the component's characteristics and the distribution of stresses change [26].

4.1.1 Textile Membranes

It is a composite material made up of a protective coating layer on top of a textile weave that serves as a load-bearing component. The term "textile" refers to the materials created from fibers. Various materials can be used to create textiles. Animal, plant, mineral, and synthetic fibers are the four main sources of these materials. The textiles membrane materials are fabrics that are produced primarily for functionality rather than aesthetics. Coated polyester Polyvinyl chloride (See Figure 2.3b) and coated glass cloth polytetrafluoroethylene (See Figure 2.3a) are two of the most often used coated fabrics. These type of composite materials are more complicated than the traditional structural materials, i.e. concrete, metals etc. [26]. PVC Coated and PVC laminated textile membranes are given in Figure 4.1 for showing the materials.
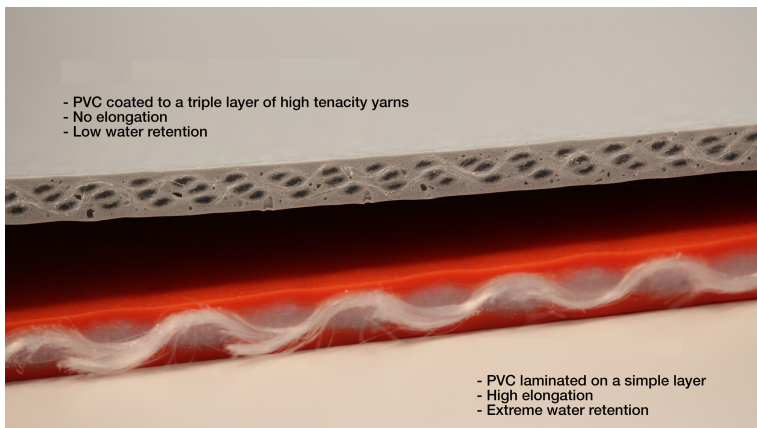
Figure 4.1: PVC Coated and PVC Laminated Membranes [10]

PVC-Polyester

PVC-polyster membranes are used more frequently than PTFE-glass membranes. This is a result of the materials' high cost. The fabric, which is made from polyester strands, is coated with PVC. Both materials are not resistant to the effects of the environment. The final lacquering layer on PVC offers this resistance [28].

It is a flexible substance. This feature offers benefits in terms of manufacturing and installation. It can be applied to any kind of membrane construction, whether it is detachable, reusable, or foldable. Depending on the climate and the material's characteristics, the service life ranges from 15 to 20 years [28]. The elongation range is between 20–30% is presented at the break stage [50].

PTFE-Glass

It is made by coating a fabric made of glass filaments with PTFE. The PTFE-Glass membrane becomes brittle and hard due to the high temperature used during the PTFE coating process, despite the fact that PTFE and glass filaments are naturally flexible. Usually, solid structures employ it. It is not appropriate for movable or temporary structures. It is delicate when folded. Its production, delivery, and installation processes demand special consideration. The PTFE coating is harmed in the event of a forceful folding. Due to exposure to water, this causes glass filaments to lose their strength. Additionally, if it folds too little, the weave's threads might break. When compared to PVC membranes, it requires more pretension, and PTFE-Glass has a higher shear strength [51].

4.1.2 Polymer Membranes

A structural material's microstructure affects its mechanical response under load. Understanding a material's microstructure is essential to comprehending how it will behave when subjected to mechanical and environmental forces. An artificial or natural types of polymer are possible to find. Natural polymers are readily accessible structures found in nature, such as cellulose, silk, etc. Plastic and artificial polymer are frequently used interchangeably. The plastics we encounter every day are made of polymers. The molecular structure, chemical family, chain shape, mechanical properties, and thermal properties of polymers are all categorized. The polymer-forming chains might take the shape of a network that is linked, branching, or straight. The polymers are classified into three categories in the classification that was created by taking into account their mechanical and thermal properties. These are elastomers, thermosets, and thermoplastics. Compared to traditional materials like concrete, metal, or wood; polymers have a much wider

range of qualities besides the stiffness and strength of the polymers are lower than the traditional materials. Particularly for fibre-reinforced polymers, a wide range of strength, elastic modulus, and elongation values can be observed, it is depending on the fiber types, e.g. glass fibers are cheap but they have lower mechanical performance while carbon fibers have higher performance but also high cost. Based on the mechanical, chemical, and processing requirements, select an appropriate polymer.

The atoms that make up the polymer's properties determine the polymer's characteristics. High resilience to external impacts is a property of flor-containing polymers. Fluoropolymers are polymers that include fluorine atoms. The membrane constructions use fluoropolymers such as PTFE, ETFE, PVDF, and FEP [52].

Elastomers

Long molecular chains with little cross-links make up its structure. Chains' geometry can take the form of a zigzag or helical spiral. Under a tensile load, elastic deformation can surpass 200%. The shape of the chains straightens when a load is applied, and it returns to its original shape when the load is removed. When heated, they become softer but do not melt; in addition, under the low temperatures, they become brittle. Silicone rubber is an elastomer and is utilized as a covering for the glass membrane [53].

Thermosets

Three-dimensional networks of its polymer chains are joined together by rigid cross-links. Both straight and branching chains are possible. Although delicate, it is more durable than thermoplastic [52]. They burn at a high temperature and do not soften when heated. They are extremely heat resistant. Its production methods are unique, and recycling is not a option for the thermosets such as epoxy [54].

Thermoplastic

Long molecular chains make up its structure. The chains could either be unbranched or branched. Despite being intertwined, the chains are not physically connected. Their primary trait is that when they are heated, they melt. Thermoplastics that have been melted can be utilized again. Heat molds them, and they are temperature-sensitive. Once they reach a particular temperature, they lose their mechanical qualities. Typically, thermoplastic materials are utilized to create membrane structures [52].

The entangled polymer chains open and straighten when a tensile load is applied to the thermoplastic material during the manufacture phase. The crystalline areas

take on a position in the direction of the applied load at the conclusion of this operation. This procedure is specifically carried out to enhance the fibers' mechanical qualities [54]. The location and crystallinity of the molecular chains affect the toughness of polyester yarn. The crystalline area is positioned in the direction of the filament axis after cooling by extending the filament. This procedure causes the other axis to collapse while the strength of the filaments increases in the direction of the applied tensile load axis [52].

Temperature has an impact on how thermoplastics behave mechanically. The molecules chains move more readily as the temperature rises. As the temperature drops, the substance solidifies and becomes brittle. The glass transition temperature is the point at which thermoplastics become brittle and lose their flexibility. Depending on the structure of the material, this temperature may be below or above room temperature. The loose chains begin to rotate and flex as the temperature rises [52] [54].

4.1.3   Reinforced Membranes

Reinforced membranes are useful for fish farming nowadays, but there are several quality issues to be aware of in order to guarantee longevity and dependability in the particular use of semi-closed cages. The lifespan of the seams depends on the adherence between the coating and the underlying fabric. Here, fatigue might occur due to stresses from waves and current. Delamination is a possibility, particularly with calendered coatings. The membrane must behave with very little elongation and maintain its predetermined form if you assume that a positive pressure will keep the cage's shape tensioned. If not, it will be challenging to sustain the overpressure [55].

According to information from the producers of reinforced materials, the breaking stress of these materials is determined by their loading history and the ensuing creep. Operational loadings should not exceed 25% of nominal strength in order to prevent creep from restricting membrane lifetimes [56]. In reaction to in-plane compression, a thin film on a flexible substrate experiences either surface wrinkles or delamination which is shown in Figure 4.2.

Cable-Reinforced Membranes

A system of cable reinforcement is advantageously incorporated in these constructions since it is feasible to get suitable membrane materials that can withstand such high tensile strains. Construction of structures with bigger cross-sectional areas, lower profiles, and longer spans are made possible by the reinforcement because it can serve the twin purposes of allowing for increased flexibility in the shape of the structure and adding strength to the structure. Due to the interaction between the
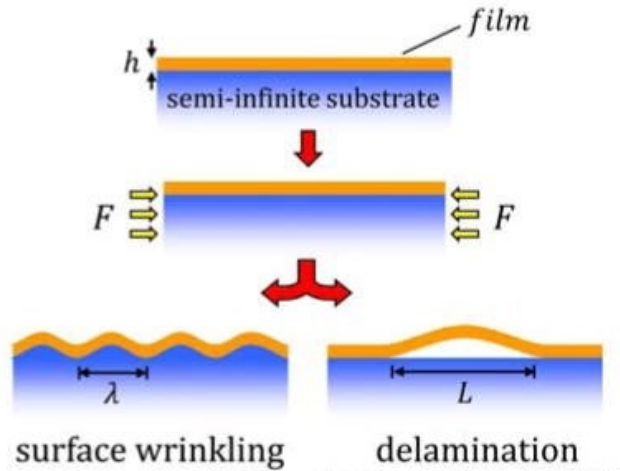
Figure 4.2: Surface Wrinkling and Delamination [11]

cables and the membrane, the analysis of cable-reinforced membrane structures is a challenging task. However, if it is considered that the membrane's only function is to transport the pressure load to the wires, the problem can be substantially simplified. This allows for the evaluation of the cables alone in addition to being a conservative assumption. While working on membranes, it is needed to be sure that the membrane does not fail. All other loads are believed to be concentrated at nodes, while the pressure load is dispersed along cable elements [32].

Fibre-Reinforced Membranes

In planar form with relatively thin walls, fiber-reinforced polymers are employed similarly to unreinforced polymers. Particular focus should be placed on the fiber reinforcing itself, which is typically in the form of several plies, to achieve a kind of construction that does honor to the material. In general, a laminate is a composite material composed of fibers and a polymer matrix. In reality, thermosets, sometimes referred to as (synthetic) resins, make up the vast majority of laminates. The hand lay-up technique and technologies dependent on it, including resin infusion, are used to create free-form fiber composites [26]. The fibre-reinforces membranes are more rigid structures than the others, therefore these membranes are out of scope of the thesis.

4.2 Mechanical Properties

4.2.1 Non-linearity

The ratio of stress to strain is not constant when there is nonlinearity. The amount of load applied to a material per unit area is known as stress. The amount of elongation of the material under the load is indicated by strain. A linear elastic material has a constant ratio of stress to strain. Until a particular point or when the material is ready to break, this constant rate can be applicable.

(a) Stress Strain Relationship of Linear

(b) Stress Strain Relationship of Nonlinear
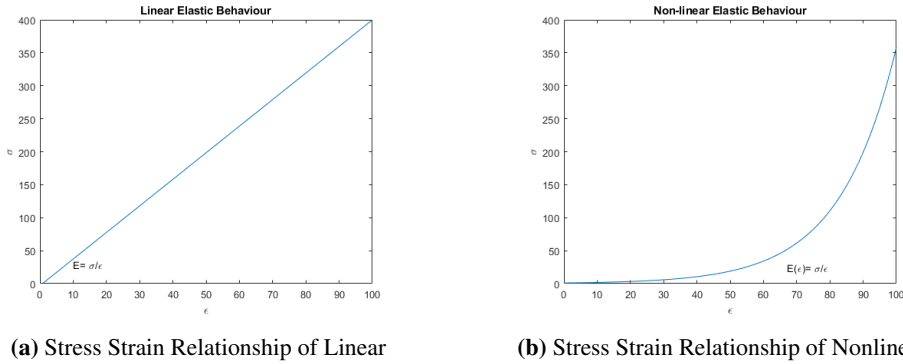
Figure 4.3: Linear and Non-linear Materials Elastic Behaviour

4.2.2 Orthotropic Material

An orthogonal anisotropic or orthotropic material is one such example. Establishing a linear approximation for the stress-strain behavior is a mathematical strategy for assessing the symmetry conditions of an orthotropic material.

An isotropic material exhibits variable mechanical behavior depending on the direction of the applied load since the connection between stress and strain is the same in all directions. A tensor of second rank n with the components $\sigma_{\alpha\beta}$ can be used to describe the stress condition in a two-dimensional material.

$$\sigma_{\alpha\beta} = \begin{pmatrix} \sigma_{11} & \sigma_{12} \\ \sigma_{21} & \sigma_{22} \end{pmatrix} \tag{4.1}$$

The second-rank tensor is also able to explain the deformation:

$$\varepsilon_{\mu\nu} = \begin{pmatrix} \varepsilon_{11} & \varepsilon_{12} \\ \varepsilon_{21} & \varepsilon_{22} \end{pmatrix} \tag{4.2}$$

The different expressions can be easily understood by choosing the first axis in the warp direction and the second axis in the fill direction. Here, n_{11} represents

the stress in the warp direction, n_{22} represents the stress in the fill direction, and n_{12} represents the shear stress. Similarly, ε_{11} represents the elongation in the warp direction, ε_{22} represents the elongation in the fill direction, and ε_{12} represents the shear deformation. In the linear approximation, a relationship between stresses and deformations can be established:

$$\sigma_{\alpha\beta} = E_{\alpha\beta\mu\nu}\varepsilon_{\mu\nu} \tag{4.3}$$

where the double-named indices must be added. In order to clarify, we could also write:

$$\begin{pmatrix} \sigma_{11} \\ \sigma_{22} \\ \sigma_{12} \end{pmatrix} = \begin{pmatrix} E_{1111} & E_{1122} & E_{1112} \\ E_{2211} & E_{2222} & E_{2212} \\ E_{1112} & E_{2212} & E_{1212} \end{pmatrix} \begin{pmatrix} \varepsilon_{11} \\ \varepsilon_{22} \\ \varepsilon_{12} \end{pmatrix} \tag{4.4}$$

The deformations can be expressed as a function of the elastic energy density A as follows:

$$\pi = \pi(\varepsilon_{\alpha\beta}) \longrightarrow n_{\mu\nu} = \frac{\partial \pi(\varepsilon_{\alpha\beta})}{\varepsilon_{\mu\nu}} \tag{4.5}$$

If the stresses-strain relation is linear, then the energy density must be approximated to the second order:

$$\pi = \frac{1}{2} E_{\alpha\beta\gamma\delta}\varepsilon_{\alpha\beta}\varepsilon_{\mu\nu} \tag{4.6}$$

The deformation is symmetric because of the symmetry of the stress tensor:

$$\sigma_{\mu\nu} = \sigma_{\nu\mu}, \varepsilon_{\mu\nu} = \varepsilon_{\nu\mu} \tag{4.7}$$

Also, the condition of symmetry for the tensor of elasticity:

$$E_{\alpha\beta\gamma\delta} = E_{\beta\alpha\gamma\delta} = E_{\alpha\beta\delta\gamma} = E_{\gamma\delta\alpha\beta} \tag{4.8}$$

The symmetry group's requirements are now put into practice. A rotation causes the deformation ab to change to mn:

$$\varepsilon'_{\mu\nu} = \Omega_{\mu\kappa}\Omega_{\nu\lambda}\varepsilon_{\kappa\lambda} \tag{4.9}$$

The following will provide the requirements of invariance:

$$E_{\alpha\beta\gamma\delta}\varepsilon_{\alpha\beta}\varepsilon_{\gamma\delta} = E_{\alpha\beta\gamma\gamma}\varepsilon'_{\alpha\beta}\varepsilon'_{\gamma\delta} = \\ = E_{\kappa\lambda\mu\nu}\Omega_{\kappa\alpha}\Omega_{\lambda\beta}\Omega_{\mu\gamma}\Omega_{\nu\delta}\varepsilon_{\alpha\beta}\varepsilon_{\gamma\delta} \tag{4.10}$$

The following results for any deformation tensor:

$$E_{\alpha\beta\gamma\delta} = E_{\kappa\lambda\mu\nu}\Omega_{\kappa\alpha}\Omega_{\lambda\beta}\Omega_{\mu\gamma}\Omega_{\nu\delta} \tag{4.11}$$

This condition can only be satisfied if all components with an uneven number of components vanish since the group of the symmetry rotations only contains components with (+1) and (-1):

$$E_{1112} = E_{2221} = E_{1211} = E_{1222} = 0 \tag{4.12}$$

Therefore, the final version of the equation:

$$\begin{pmatrix} \sigma_{11} \\ \sigma_{22} \\ \sigma_{12} \end{pmatrix} = \begin{pmatrix} E_{1111} & E_{1122} & 0 \\ E_{2211} & E_{2222} & 0 \\ 0 & 0 & E_{1212} \end{pmatrix} \begin{pmatrix} \varepsilon_{11} \\ \varepsilon_{22} \\ \varepsilon_{12} \end{pmatrix} \tag{4.13}$$

E_{1111} denotes the stiffness along the warp direction, E_{2222} the stiffness along the fill direction and E_{1212} indicates the shear stiffness.

A membrane has orthotropic behaviour. The fact that a membrane is made of weave is the main explanation for this. Two perpendicular threads are used to create the weave. In the context of a weave, the yarns possess distinct geometries [53].

4.2.3   Viscoelastic Material

Viscoelasticity, a phenomena of time-dependent strain, is visible in glasses and other amorphous materials. As opposed to crystalline metals, polymers and amorphous materials do not undergo atomic displacements on certain crystallographic planes during deformation. Instead, a steady load causes an ongoing displacement of atoms or molecules over time [57].

Numerous studies have demonstrated that membrane materials, such as coated textiles and thin films made of polymer, primarily possess viscoelastic-plastic properties that fall in the range of optimum elasticity and ideal viscosity, as shown in Figure 4.4. The uniaxial tensile tests are one of the most popular techniques used to evaluate the stress-strain curves for further evaluating the crucial mechanical parameters in order to comprehend the mechanical behaviors of membrane materials. The connections between the responsive stress and strain when an external force with changing strain rates is applied to a membrane material are typically linear for the ideal elastic solid, but nonlinear and viscoelastic-plastic for actual membrane materials, it can be seen in Figure 4.4a. The responsive strain and time relationships for the ideal viscous fluid and real membrane materials are linear and nonlinear, respectively, whereas the loading external force is the constant stress and the responsive strain of the ideal elastic solid is also constant, it can be seen in Figure 4.4b. Therefore, it is believed that by combining these two simplest materials, including the ideal elastic solid and ideal viscous fluid, the viscoelastic properties of this type of genuine membrane materials can be represented and described with a more complicated model [58].

(a) Stress-Strain Curve   (b) Strain-Time Curve
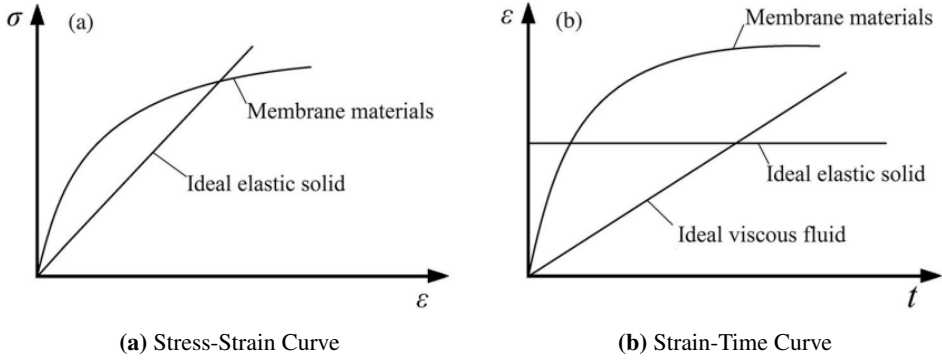
Figure 4.4: Viscoelastic Properties of Membrane Materials

Viscoelastic Constitutive Law For Coated Fabrics

A plane stress anisotropic model is presumed for coated fabrics. The stress vector $\sigma(t)$ can be represented in the integral form as follows by taking into account arbitrary history of $\varepsilon(t)$:

$$\sigma(t) = \int_0^t [\mathbf{Y}(t-\tau)]\frac{\partial \varepsilon(\tau)}{\partial \tau}d\tau \tag{4.14}$$

where

$$\sigma(t) = (\sigma_x(t)\sigma_t(t)\tau_{xy}(t))^T$$
$$\varepsilon(t) = (\varepsilon_x(t)\varepsilon_y(t)\gamma_{xy}(t))^T$$
$$\mathbf{Y(t)} = \begin{bmatrix} Y_{11}(t) & Y_{12}(t) & 0 \\ Y_{21}(t) & Y_{22}(t) & 0 \\ 0 & 0 & Y_{33}(t) \end{bmatrix} \tag{4.15}$$

The membrane material's fill and warp directions' tensile stresses, x and y, and its shear stress are represented. The strains ε_x, ε_y, and γ_{xy} correspond to the aforementioned stresses. The relaxation modulus matrix $\mathbf{Y(t)}$ can be described in a number of ways based on various material models, including an exponential function, a power law, etc. The elastic shear modulus is about equivalent to $Y_{33}(t)$ in this study and is constant throughout time [12].

The basic Maxwell model, in which just one fundamental spring element and one fundamental dashpot element are joined in the series connection, is one of the most fundamental models. The other model is Kelvin-Voigt model, here, the Maxwell model is considered [58].

The loading strain rates are homogeneous and adjustable for the majority of
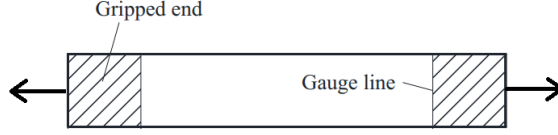
Figure 4.5: Illustration of Uniaxial Test [12]

experimental studies of the uniaxial tensile stress-strain characteristics of membrane materials by programming the testing apparatus. As a result, the generalized Maxwell model's overall strain may be stated as follows. The general Maxwell model is also shown in Figure 4.22 below [59]:

$$\varepsilon(t) = \int \dot{\varepsilon} dt = \dot{\varepsilon} t \tag{4.16}$$

where, in uniaxial tensile tests, $\dot{\varepsilon}$ is the constant strain rate. The initial strain is zero for uniaxial tensile testing, as shown in the following:

$$\varepsilon_0 = \dot{\varepsilon}|_{t=0} = 0 \tag{4.17}$$

Therefore, for these two equations 4.16 and 4.17 are going to substitute into the stress response equation of the Maxwell Model, in Equation 4.18:

$$\sigma(t) = \varepsilon_0 G(t) + \int_0^t G(t-\zeta) \frac{d\varepsilon(\zeta)}{d\zeta} d\zeta \tag{4.18}$$

where E_0 and E_i are the elastic modulus of the fundamental spring element and the fundamental spring element in the i_{th} Maxwell model, respectively. $G(t) = E_0 + \sum_{i=1}^n E_i e^{\frac{-t}{\tau_i}}$ is the relaxation elastic modulus of the Maxwell model, which is equal to the total stress reacting to the unit strain of $\varepsilon = 1$.

$$\sigma(t) = \varepsilon_0 G(t) + \int_0^t G(t-\zeta) \frac{d\varepsilon(\zeta)}{d\zeta} d\zeta = \int_0^t G(t-\zeta) \dot{\varepsilon} d\zeta \tag{4.19}$$

and

$$\sigma(t) = \int_0^t E_0 \dot{\varepsilon} d\zeta + \sum_{i=1}^n \int_0^t E_i e^{\frac{-(t-\zeta)}{\tau_i}} \dot{\varepsilon} d\zeta = E_0 \dot{\varepsilon} t + \dot{\varepsilon} \sum_{i=1}^n \eta_i (1 - e^{\frac{-t}{\tau_i}}) \tag{4.20}$$

Thus, it is possible to derive the constitutive equation for modelling the uniaxial tensile stress-strain behaviors of viscoelastic membrane materials under fixed load

and strain rates [58]:

$$\sigma(t) = E_0\varepsilon(t) + \dot{\varepsilon}\sum_{i=1}^{n}\eta_i(1 - e^{-\frac{\varepsilon(t)}{\dot{\varepsilon}\tau_i}})$$ (4.21)

For coated textiles, the General Maxwell solid model in Equation 4.22 is a popular viscoelastic constitutive law. In this approach, the substance is represented as a collection of several Kelvin-Voigt components linked in series. Each component is made up of two parallel dashpots and springs, which stand in for the elastic and viscous behaviors, respectively. The model presupposes that a distribution of relaxation durations governs the material response. The General Maxwell solid model can properly represent the viscoelastic behavior of coated textiles, including their time-dependent deformation and stress relaxation properties, by altering the number and distribution of these components.

$$\sigma + \left(\sum_{i=1}^{N}\tau_i\right)\frac{\partial\sigma}{\partial t} + \left(\sum_{i=1}^{N-1}\left(\sum_{j=i+1}^{N}\tau_i\tau_j\right)\right)\frac{\partial^2\sigma}{2} + \cdots +$$

$$\left(\sum_{i_1=1}^{N-n+1}\cdots\left(\sum_{i_a=i_a-1+1}^{N-(n+a)+1}\cdots\left(\sum_{i_n=i_{n-1}+1}^{N}\left(\prod_{j\epsilon i_1,\ldots,_n}\tau_j\right)\right)\cdots\right)\cdots\right)\frac{\partial^n\sigma}{\partial t^n} + \cdots + \left(\prod_{i=1}^{N}\tau_i\right)\frac{\partial^N\epsilon}{\partial t^N} =$$

$$E_0\epsilon + \left(\sum_{i=1}^{N}(E_0 + E_i)\tau_i\right)\frac{\partial\epsilon}{\partial t} + \left(\sum_{i=1}^{N-1}\left(\sum_{j=i+1}^{N}(E_i + E_0 + E_j)\tau_j\tau_i\right)\right)\frac{\partial^2\epsilon}{\partial t^2} + \cdots +$$

$$\left(\sum_{i_1=1}^{N-n+1}\cdots\left(\sum_{i_a=i_a-1+1}^{N-(n+a)+1}\cdots\left(\sum_{i_n=i_{n-1}+1}^{N}\left(E_0 + \sum_{j\epsilon i_1,\ldots,i_n E_j}\right)\left(\prod_{k\epsilon i_1,\ldots,_n}\tau_k\right)\right)\cdots\right)\cdots\right)\frac{\partial^n\epsilon}{\partial t^n} + \cdots +$$

$$\left(E_0 + \sum_{j_i}^{N}E_j\right)\left(\prod_{i=1}^{N}\tau_i\right)\frac{\partial^N\epsilon}{\partial t^N}$$

(4.22)

4.3 Testing of the Materials

Comparing membranes to conventional building materials, more sophisticated mechanical behavior can be seen. The design, analysis, production, and assembly processes are influenced by the behavior of the membranes under load. Membranes that solely carry tensile loads exhibit bidirectional tensile behavior. The numbers for elongation and breaking points discovered by doing a tensile test in one direction do not offer the information needed for analysis. The two-directional weave and the bidirectional interplay of these directions complicate the mechanical behavior of membranes. Additionally, temperature and time have an impact on the mechanical behavior of membranes. The membrane's mechanical behavior in this situation is not entirely under control [60]. The structural modeling of a membrane structure uses the material's elasticity parameter and the Poisson ratio. To ascertain the mechanical characteristics of the membrane materials, various ex-

periments are carried out. Biaxial can be seen in Figure 4.7a and unaxial tests can be seen in Figure 4.5. There are the two fundamental examinations needed for analysis and manufacture.

Table 4.1: Pros and Cons of Uniaxial and Biaxial Test Methods

Methods	Pros	Cons
Uniaxial Testing	Simple to execute	Distribution of non-homogeneous strain, a shear angle that is difficult to detect, and a rough estimate of the shear modulus
Biaxial Testing	Uniform Shear Stress	The results are sensitive to the stress ratio, the biaxial tensile machine is necessary, and a reasonable loading spectrum is required.

4.3.1 Tensile Testing

A fundamental mechanical test that is frequently used to ascertain the mechanical characteristics of materials is the tensile test. In this test the load-displacement information is captured when a specimen is exposed to a uniaxial tensile stress until it cracks. The load-displacement data may be used to calculate the material's tensile characteristics including the ultimate tensile strength, yield strength and elongation (%) at break. Tensile testing is a vital component of material characterization and is frequently employed to determine if a material is suitable for a certain application. The mechanical characteristics of the membrane material which will be utilized to design the solar island structure are being ascertained in the context of the solar island project by the tensile test.

It is employed to ascertain how a membrane and connection specifics would behave under a strain. The test sample is subjected to a force until it breaks in the longitudinal and transversal directions. In this technique, the membrane's maximum tensile strength and the length of the break point are discovered.

This test method, according to ASTM International, includes the measurement of fabric's uniaxial elongation when applied to a specific force. The amount of force used depends on the material mass and the intended application. One end of a specimen is subjected to a single-direction force while the other end is fixed vertically. The uniaxial elongation under the specified stress is measured after a predetermined amount of time [61].

The Hook's spring element and the fundamental dashpot element are employed, respectively, in continuum mechanics to describe the ideal elastic solid and ideal viscous fluid. As was already established, membrane materials' mechanical reactions are substantially more complicated and cannot be described by a single simple spring or dashpot element. One basic spring element and one basic dashpot element combined in two permutation modes results in the definition of the two most fundamental models among them [58]. Also, in practice; while making the uniaxial tensile tests, the viscoelastic part can not be calibrated. The Dynamical

Mechanical Analysis, or a relaxation/creep test, is used to do such. Therefore, for simulating the experiment on FEM software, two different material models are needed. The reason of that is elastoplastic and viscoelastic behaviour can not combine in the same model.

Dynamical Mechanical Analysis

The DMTA approach is a crucial tool for assessing the viscoelastic characteristics of materials under cyclic stress, incorporating temperature effects. It determines the material's mechanical properties at different temperatures and frequencies, revealing the storage modulus G', loss modulus G'', and loss factor $tan\delta$, which are vital for understanding viscoelastic behavior. In the solar island project, DMTA is used to evaluate the membrane material's viscoelastic properties, aiding in the development of a comprehensive model for its behavior under cyclic stress and temperature fluctuations. Dynamic Mechanical Analysis, a broader technique, analyzes the dynamic properties of materials, including polymers, utilizing a Dynamic Mechanical Analyzer. Frequency response diagrams with storage and loss moduli values are generated, and the oscillation pattern is achieved using adjustable and fixed clamps as shown in Figure 4.6. DMTA expands upon DMA by incorporating thermal analysis to explore how temperature variations impact material mechanics, making it relevant in industries with temperature fluctuations, such as automotive, aerospace, and construction [13].
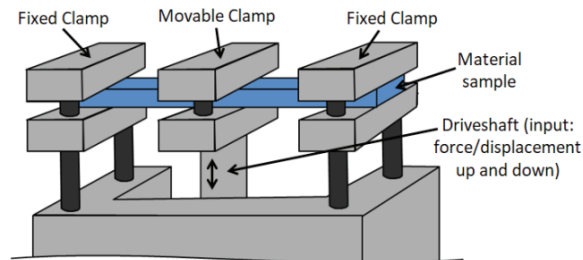
Figure 4.6: Dynamical Mechanical Analyzer [13]

4.3.2 Biaxial Testing

In comparison to uniaxial mechanical qualities, biaxial mechanical properties require more sophisticated tools, specimens, and analytical techniques. In fact, due to stress concentration in specimen arm locations, biaxial research is only now available up to a particular ultimate strength. Multiple slits added to the speci-

men arm still can't alleviate stress concentration, and as a result, the breaks in the findings that are now accessible are not in or close to the specimen center. The differences between the outcomes of the experiment and the numerical analysis can be attributed to this, in part [62].

A biaxial machine (see Figure 4.7b) with computer control and acquisition is

| (a) Illustration of Biaxial Test Setup[12] | (b) Biaxial Test Machine [63] |
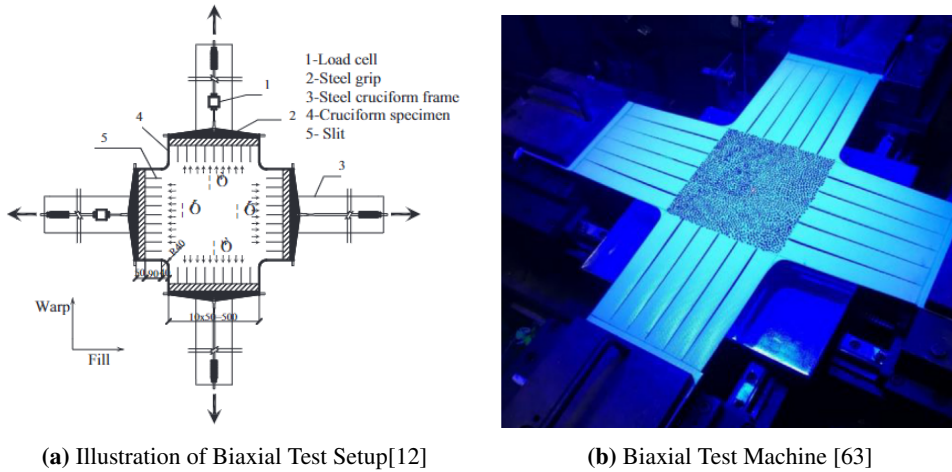
Figure 4.7: Biaxial Testing

used to conduct mechanical tests. The platform-mounted biaxial apparatus has four arms constructed of steel structures. To ensure that the material slack is removed, specimens are clamped at gripping ends and preloaded. While loads are recorded by a typical force transducer, displacements are measured using DIC. The calculation area in reference pictures is defined and segmented into virtual grids with equal spacing in order to compute stresses and apply DIC method. To determine deformation, digital grid displacements are computed. Tracking the same spots between two images taken before and after distortion is the fundamental tenet of the DIC approach. A square reference subset from the reference picture is chosen, and it is then utilized to monitor its location in the image captured since the subset in order to calculate displacements [62].

4.4 Material Durability

The system's economic performance depends on long membrane lifetimes. This is possible by meeting a number of strict requirements, including the selection of materials for environmental robustness and the combination of vertical strength and horizontal elasticity for several million buckle-free operational cycles [56].

The resilience of the membrane fabric has a significant impact on the lifespan of the membrane structure. Its capacity to withstand deterioration from UV rays and wicking, assaults from organic matter, and the preservation of seam strength all have a significant impact on its longevity, accelerated weather testing under various climatic circumstances, as well as tests for strain resistance and cleanability can be used to determine the endurance of advanced materials [64]. A membrane's physical strength (resistance to wear and tear) and permeability are two crucial properties that influence how long it will function (especially irreversible fouling versus long-term recoverability). The entire performance of a membrane is influenced by a variety of design and operational factors, and over time, particular study areas have concentrated on enhancing pre-treatment and cleaning to reduce membrane fouling. The influence of membrane characteristics on its overall performance in underwater environments is a significant factor that has received limited research attention. Understanding the role of membrane properties in underwater conditions is crucial for optimizing their functionality in such environments [65].

4.4.1 Degradation Mechanism of the Material

The deterioration of the materials over the design life of the structure must be accounted for by setting an appropriate life-cycle factor in order to determine the resistance of the structural elements [27]. Thin shells or membranes with constricted boundaries frequently deform or deflect, which is a common material behavior applicable to various engineering situations. The development of new products and the testing of materials both greatly benefit from a thorough understanding of the deformation mechanisms of various materials and structures with various Poisson's ratios [66]. Different load patterns, such as cyclic wind loads, are difficult for coated textiles to withstand as structural components. One type of multi-component architectural fabric is called PET-PVC, or polyethylene terephthalate textiles covered with polyvinyl chloride. The specific characteristics of the various PET-PVC layers, such as the PET fiber fabric, PVC main coat, adhesive layer, top and primer coating. With regard to these layers, PET exhibits great optical transparency, high strength and ductility, and good weathering resistance, whereas PVC resins show a transparent material with low strength and extreme flexibility and fair weathering resistance [67].

Different weathering processes (photodegradation, discoloration, hydrolytic, and thermal degradations) that might, directly or indirectly, lessen the tensile strength of PET woven textiles were reviewed and assessed. They offered proof that the primary cause of the chain separation mechanism's decline in tensile strength is photodegradation. They also understood that photodegradation is accelerated by temperature, although temperature by itself (without UV) has little impact on the

degradation of PET yarns' tensile strength under ambient circumstances. When there is oxygen present, UV radiation, high temperatures, and mechanical strains all cause PVC to breakdown [5]. Because of this, thermal, oxidation, and UV light stabilizers are used to combat weathering issues; additional additives may be used as a softener or to lessen the amount of dirt that sticks to the PVC coating. Dehydrochlorination (the successful removal of HCl) and the creation of lengthy conjugated polyene sequences, cross-linking, and thermooxidation are all aspects of PVC aging [68][69].

For PTFE-coated fiberglass fabric, the case studies have shown that a life expectancy of over 30 years is reasonable. Due to wear and deterioration, structures that have been assessed at 30 years duration do not require replacement. The fabric is almost durable to any UV radiation, and large temperature variation damage thanks to the several coatings of PTFE [64].

Chapter 5

Structural Theory

5.1 Shell Theory

It has become vital to distinguish between two sorts as the mathematical theory of such structural elements has developed: All walls that have curved surfaces are referred to as shells, while all plane walls are referred to as plates. After taking all of these factors into account, we can describe a shell as a physical object that, when it comes to stress analysis, may be thought of as the materialization of a curved surface. According to this description, a shell's thickness is rather minor in comparison to its other dimensions.

A shell is often limited by two curving surfaces called the faces. The thickness of the shell may be uniform throughout or it may differ from place to place. We refer to the surface that is halfway between the two faces of such a shell as its middle surface. The shell can be fully represented geometrically if we know the shape of the main surface and the thickness of the shell at each point [14].

5.1.1 Stresses on a Shell

A point's location on the middle surface requires two coordinates because it extends in two dimensions. Let's suppose that on the center surface, a system of coordinates x, y, has been established such that the lines x is constant and the lines y is constant intersect at right angles. This system is known as a Gaussian coordinate system. Then, as illustrated in Figure 5.1, removing an element from the shell by removing it along two sets of nearby coordinate lines. The cuts are performed such that the element's four sides are parallel to the shell's center surface.
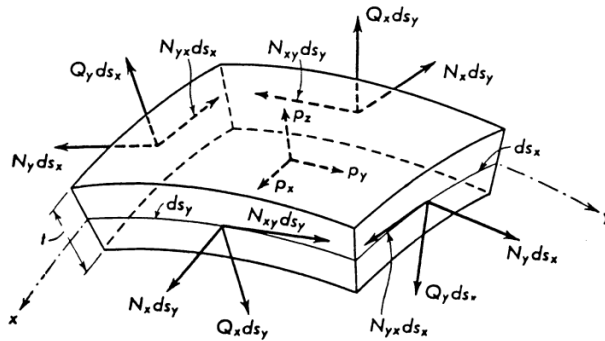
Figure 5.1: Stresses and Loads on a Shell Element [14]

The element's front side is a cross sectional piece, with x being constant throughout the shell and having the area $ds_y \cdot t$. The resultant of the stresses operating on this region based on the length ds_y. The resultant falls correspondingly as ds_y gets closer to zero, and the ratio of force to section length has a finite upper limit. Therefore, it seems sense to refer to this quotient as the "stress resultant".

We must decompose the stress resultant into components for all analytical work. The tangent to the line element ds_y, another tangent to the center surface at right angles to ds_y which is normal to the cross section, and a normal to the shell are the three reference frames we decide to use. We provide the following definitions for the force components in these directions:

The force in direction x transmitted by a unit length of section (measured on the center surface) in a section where x is constant is referred to as the normal force N_x. If it is tensile, it is positive; if it is compressive, it is negative. In a section where y is defined as constant, appropriately, the normal force N_y [14].

The force transmitted by a unit length of this section and directed tangent to ds_y is known as the shearing force N_{xy} in a section where x is constant. If it indicates toward increasing y on the side of the shell element where a tensile force Nx would point toward increasing x, it is regarded as positive. In accordance with this, a similar approach is used to define the shearing force N_{yx} in the portion where y is constant. The choice of the coordinates affects the sign of both shear forces.

The force normal to the center surface transmitted across a unit length in a section where x is constant is known as the transverse force Qx. Every shell meets within the parameters above, including those with unspecified faces and thickness. It can be described that the stress resultants as integrals of the stresses acting on a section in the typical example of a shell with solid material sandwiched between its faces. Then, these integral expressions that are generated from the aforementioned definitions may be thought of as the definitions themselves. The derivations are

in below. The total force normal to the region in Figure 5.2 where x is constant is, by definition, $N_x ds_y$. It is the outcome of the stresses σ_x that are applied to this region. We can ignore a potential variation in this direction because the width ds_y is of differential magnitude, but we must take into account a variability of all stresses throughout the thickness of the shell. When this expression is integrated within the boundaries $-\frac{t}{2}$ and $+\frac{t}{2}$, the total normal force for the element $ds_y \cdot t$ is discovered:

$$N_x ds_y = \int_{-\frac{t}{2}}^{+\frac{t}{2}} \sigma_x ds_y \frac{r_y + z}{r_y} dz \tag{5.1}$$

This is the equation that links the normal force and the normal stress when the component ds_y on both sides is removed. The forces N_{xy} and Q_x must also be obtained by integrating the shearing stresses τ_{xy} and τ_{xz}. In total, we have:

$$N_x = \int_{-\frac{t}{2}}^{+\frac{t}{2}} \sigma_x \frac{r_y + z}{r_y} dz$$

$$N_{xy} = \int_{-\frac{t}{2}}^{+\frac{t}{2}} \tau_{xy} \frac{r_y + z}{r_y} dz \tag{5.2}$$

$$Q_x = -\int_{-\frac{t}{2}}^{+\frac{t}{2}} \tau_{xz} \frac{r_y + z}{r_y} dz$$

Using the same logic, develop three additional equations for the other three stress resultants in a region where y is constant:

$$N_y = \int_{-\frac{t}{2}}^{+\frac{t}{2}} \sigma_y \frac{r_x + z}{r_x} dz$$

$$N_{yx} = \int_{-\frac{t}{2}}^{+\frac{t}{2}} \tau_{yx} \frac{r_x + z}{r_x} dz \tag{5.3}$$

$$Q_y = -\int_{-\frac{t}{2}}^{+\frac{t}{2}} \tau_{yz} \frac{r_x + z}{r_x} dz$$

It is not implied from the equality of the shearing stresses, $\tau_{xy} = \tau_{yx}$, that the shearing forces are also equal. Only when τ_{xy} does not depend on z or when $r_x = r_y$, which is visible for a sphere, does the difference between N_{xy} and N_{yx} vanish. When t and z in a thin shell are small in relation to the radius r_x, r_y, the difference between the two shearing forces is not significant and is frequently disregarded [14].

Some stresses have moments with regard to the center of the section when the
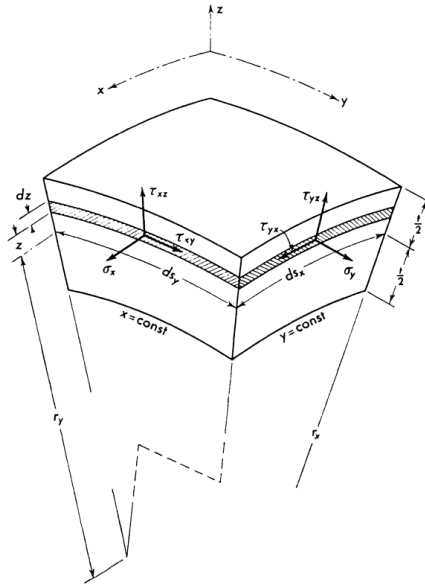
Figure 5.2: Stresses Acting on a Shell Element [14]

stresses are not distributed evenly over the thickness t. We must take into account these moments since they affect the equilibrium of the shell element:

$$M_x = -\int_{-\frac{t}{2}}^{+\frac{t}{2}} \sigma_x \frac{r_y + z}{r_y} z dz$$

$$M_{xy} = \int_{-\frac{t}{2}}^{+\frac{t}{2}} \tau_{xy} \frac{r_y + z}{r_y} z dz$$

(5.4)

It might be viewed as the definitions of the moments of bending and twisting. The minus signs set right the sign convention and they are arbitrary. Another bending moment and another twisting moment are derived when the same concepts are applied to a section where y is constant [14]:

$$M_y = -\int_{-\frac{t}{2}}^{+\frac{t}{2}} \sigma_y \frac{r_x + z}{r_x} z dz$$

$$M_{yx} = \int_{-\frac{t}{2}}^{+\frac{t}{2}} \tau_{yx} \frac{r_x + z}{r_x} z dz$$

(5.5)

5.2 Membrane Theory

The membrane theory is also called theory of membrane shells. The internal stresses are replaced by their resultants in shell modeling, same like for beams and plates. These are forces and bending moments for a unit length, which are sometimes referred to as "internal forces" or "stress resultants" [15].
The mathematical definition of the membrane forces (or in-plane forces) is

$$N_x = \int_h \sigma_x dz, \, N_y = \int_h \sigma_y dz, \, N_z = 0, \tag{5.6}$$

for the bending moments,

$$M_x = \int_h z\sigma_x dz, \, M_y = \int_h z\sigma_y dz, \, M_z = 0. \tag{5.7}$$

The stress resultants of τ_{xz} and τ_{yz}'s out-of-plane shear stresses are given below:

$$V_x = \int_h \tau_{xz} dz, \, V_y = \int_h \tau_{yz} dz, \tag{5.8}$$

In Figure 5.3(a) shows bending moments, (b) shows out-of-plane shear forces on a element. On the left part of the Figure 5.3, just the three in-plane forces are taking into consideration. This theory reflects the fundamental behavior of shells, therefore it is obviously applicable to tents (membranes without bending resistance), but it may also be applied to other shells (such reinforced concrete).
The 'static theorem' of plasticity states that a conservative estimate for the plastic
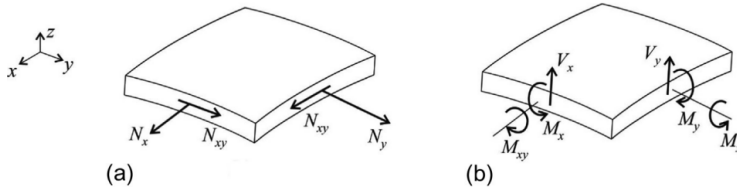
Figure 5.3: Membrane forces on a element [15]

failure load may be achieved by assuming a "statically acceptable" internal force distribution (where only the equilibrium equations are met). Consequently, membrane theory provides a reliable approximation for structures constructed of ductile materials (where the bending moments are omitted but the equilibrium equations are met) [15].

5.3 Form Finding

It is more challenging to solve the issue with prestressed reinforced tensile membrane structures. Physical models may be used to predict a wide range of complicated structures. The prestress and surface geometry information necessary to manufacture and stress the membrane shape cannot be correctly provided to the manufacturer without the use of unique procedures [20]. Generally speaking, the form-finding process should provide optimal structural shapes, or shapes that would meet the functional needs and accompanying durability and strength criteria at a low cost. The tension structures' capacity to produce aesthetically pleasant, even dramatic effects, is one of their most attractive qualities [70].

The original, equilibrated shape of the structure is established using the form-finding procedure. The initial form of a membrane construction depends on the boundary conditions, the stress ratio in the warp and fill directions, and the stress ratio; external loads are not taken into account at this point. The membrane arrangement in the three-dimensional space is the result of correct calibration of the various parameters and cannot be imposed a priori [71].

5.3.1 Methodologies

The method of determining the form of membranes with surface stress typically entails:

- Building small-scale physical models out of materials like fabric and paper.

- The improvement of computational models utilizing a range of numerical methods [70].

Physical Models

Physical models are still employed throughout the design process, mostly as a form of members of the design and as a means of validating computational results. However, when multiple modifications or improvements to the surface shape are required, computational approaches are increasingly used instead of pricey physical models due to the limits of physical modelling [70].

Computational Models

The shape, stresses, and deformations of tension structures are represented by a set of numerical and graphical data in computational models of tension structures. The information is derived from numerical algorithms that outline an iterative process of tensioned surface geometry adjustment until a static equilibrium—i.e., the

equilibrium of all forces operating on the surface—is reached. As with any numerical techniques, the approach involves a creative assumption as to "how the surface should look like equally." Iterations are required to arrive at the desired shape because the projected form is unlikely to satisfy the requirements of static equilibrium When referring to computational modeling, the word 'form discovery' might refer to any of the following [70]:

- Finding the ideal tension membrane form

- Finding a tension membrane design that is statically balanced but does not need have a constant surface stress

- Identifying a shape that is close to the state of complete static equilibrium (combining form finding and patterning)

In the first case, the structure's limits are set, and the numerical method is built in a way that permits the surface to choose its own geometric configuration in accordance with the basic law of constant surface stress. In the later case, the state of ongoing tension is relieved. Although the resulting structural form is static equilibrium, as was already said, the surface stress is not always constant.

Lastly, case is an effort to simplify the design route by using the same mesh, or at least a portion of it, for both form-finding and the generation of the cutting pattern. Mesh distortions that occur throughout the form-finding process are managed in order to accomplish that. There are several ways to accomplish this. The locations of the seam lines in the x-y plane must be known at the beginning and must not change as a result of form-finding in one approach.

As a result, during the actual form-finding process, the nodes cannot move in the x-y plane. This approach guarantees equilibrium solely in the z-direction. Although the generated surface may resemble the final surface rather closely, cutting patterns should not be created using the even lines on the surfaces since they do not represent the lines of complete static equilibrium [70].

The various computing techniques available each have their own difficulties that must be taken into account, such as computational time, stability, and simplicity. Any numerical scheme must include computational time, which can sometimes be expensive. Better descriptions of the initial shape close to the developed shape help the dynamic relaxation method. For surfaces with complicated forms and boundary conditions, this might not always be understood. To manage the stability and convergence of dynamic equilibrium approaches, different parameters are needed [18].

Chapter 6

Experiment

6.1 Introduction

The membrane material used in this study is composed of an PVC coated fabric and is intended for use on a solar island, which is a floating platform containing solar panels. The membrane material is expected to be exposed to various environmental factors, including UV radiation, moisture, and temperature fluctuations. The purpose of this study is to investigate the mechanical behavior of the membrane material under tensile and dynamic mechanical loading conditions.

The shear test was not performed on the membrane material because these materials do not experience significant bending forces. Shear testing is typically conducted on materials that are subjected to shearing or twisting forces, which are not applicable in the case of membrane materials. Therefore, the focus of the testing and analysis was primarily on the tensile behavior of the material, which is more relevant for membrane applications.

By understanding the mechanical properties of the material, we can better understand its potential durability and suitability for use in a solar island. The tests will be conducted using standard testing protocols, and the data obtained will be used to develop a computational model for the membrane material.

To gain a better understanding of the mechanical behavior of the membrane material for the solar island projects, two experiments were conducted which are the tensile test and the dynamic mechanical analysis. Section 4.3 provides short explanations of each of these tests. This chapter presents the experimental setups, specimen preparation, and the results obtained in the study.

The experiment was conducted in the Material Test Laboratory at SINTEF, with the

assistance of Kristian Aamot, the senior research engineer. The research involved experimental analysis on a previously uncharacterized membrane material. Small samples were obtained by cutting sections from a larger piece of the membrane and these samples were used for conducting tensile tests and DMA experiments. All the necessary experimental equipment utilized in the study was provided by SINTEF.

6.2   Testing Equipments

6.2.1   Tensile Test

A UTM (Figure 6.1a) is the main component of the experimental setup and is used to apply a tensile force to the specimen for testing the strength of a membrane material can include the following components:

Load Frame: The load frame is the main structural component of the universal testing machine that supports the clamping system and the test specimen. It is designed to withstand the force generated during the tensile test.

Crosshead: The crosshead is the movable part of the testing machine that applies the tensile load to the specimen. It is driven by a motor and moves in a vertical direction.

Load Cell: The load cell is a device that measures the force applied to the specimen during the tensile test. It is typically located on the crosshead and measures the load generated by the test specimen.

Grips: The grips are the components of the clamping system that hold the specimen securely in place and ensure that the load is applied uniformly along the length of the specimen. They can be designed for different types of specimens, such as flat or round, and can be customized to suit the material being tested.

Control panel: The control panel is the interface that allows the operator to set the testing parameters and record the test data. It typically includes a display screen, buttons or a touchscreen, and software that controls the motor and load cell.

Image Capturing System: A camera is used to capture images of the specimen during the test. The camera is mounted on a tripod and positioned so that it can capture the entire length of the specimen. The camera has been aligned and calibrated.

Image analysis software: The images captured by the camera are analyzed using eCorr software, a DIC software. eCorr is capable of tracking the movement of the specimen and measuring its elongation. It achieves this by calculating the strain field from a speckled pattern applied on the specimen. This allows for accurate and detailed analysis of the deformation and strain distribution in the material.

Spray paint: The specimen is prepared by cutting it to the appropriate dimensions and marking with dots on the membrane material using black spray paint. This is done to improve the accuracy of the measurements obtained using the camera.

(a) UTM at Material Lab   (b) UTM Illustraion
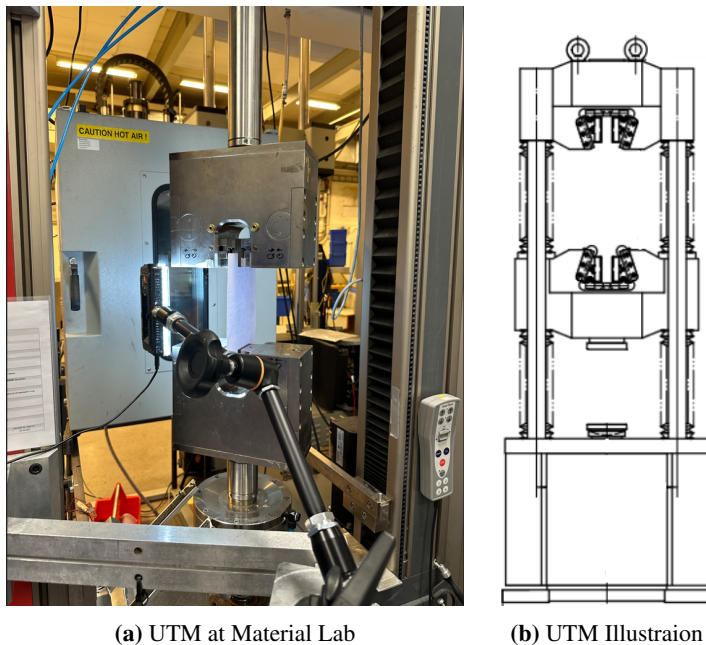
Figure 6.1: Universal Test Machine

The specimen is held firmly in the clamping system's grips during the tensile test, and the crosshead provides a tensile load to the specimen. Nevertheless, a camera capturing system is used rather than an extensometer to measure the elongation of the specimen. The camera is on a tripod and placed to record the whole length of the specimen. The camera was calibrated and positioned to achieve an accurate assessment of the elongation.

Using eCorr software, to analyze the collected pictures from the experiment, it is possible to follow the movement of the specimens and calculate its elongation. The strain in the specimen may also be determined using the program. The specimen

is coated with black spray paint, and dots are made on the membrane material because eCorr needs the speckle pattern for the DIC analyses. increase the precision of the measurements taken with the camera. As reference marks, these dots enable highly accurate tracking of the specimen's movement.

The eCorr software records the load-displacement data, which may be used to calculate the material's tensile parameters such ultimate tensile strength, yield strength, and elongation at break. Instead of using an extensometer, a camera capturing system can offer several advantages including improved accuracy and the capacity to record more precise data regarding the specimen's deformation behavior. The validation process ensures that the measurements obtained using the camera and software are accurate and reliable.

Also, in practice, while making the uniaxial tensile tests, the viscoelastic part cannot be calibrated. The Dynamical Mechanical Thermal Analysis test is used to do so. Therefore, for simulating the experiment on a FEM software, two different material models are needed. This limitation arises from the fact that commercial software does not provide a built-in capability to combine elastoplastic and viscoelastic behavior within the same model. To incorporate both behaviors, one would need to utilize UMAT code or implement a custom material model.

6.2.2 Dynamic Mechanical (Thermal) Analysis

The Dynamic Mechanical Thermal Analysis test is a technique used to study the viscoelastic behavior of materials under varying mechanical and thermal conditions. A sample is put through a dynamic mechanical test in which a sinusoidal force (stress) is applied at a certain frequency to it. The result of this is a sinusoidal deformation (strain) in the material. The delay between stimulation and response is known as the phase shift (δ), and in theory, it has a value of $0°$ for totally elastic samples and $90°$ for entirely viscous materials. In practice, depending on the ratios of elastic and viscous properties, most materials display a phase shift value between $0°$ and $90°$ [13]. Several parameters are produced by mathematically processing the measured data from a DMA test. These include the complex modulus E*, the loss modulus E", the storage modulus E', and the loss factor tanδ. The stiffness of the material and the elastic component of the response are described by the storage modulus E', which is the real portion of the complex modulus E*. The lost oscillation energy is represented by the loss modulus E", which is the imaginary component. The relation between the storage and loss modulus can be seen in Figure 6.2. A viscoelastic system's mechanical damping or internal friction is described by the loss factor (tanδ), which is the ratio of E' to E'.

The values of the storage modulus E' and loss modulus E", as well as the frequencies where the analysis was conducted, are frequently displayed in the findings as

frequency in horizontal axis and both of the modulus are in vertical axis graphs. These graphs are also known as frequency sweeps. For quality assurance or product development, DMTA identifies transition zones in plastics such as the glass transition and melting point. Little regions of transition can be detected by DMTA. [72]

The test procedure is as follows, after being clamped between the mobile and sta-
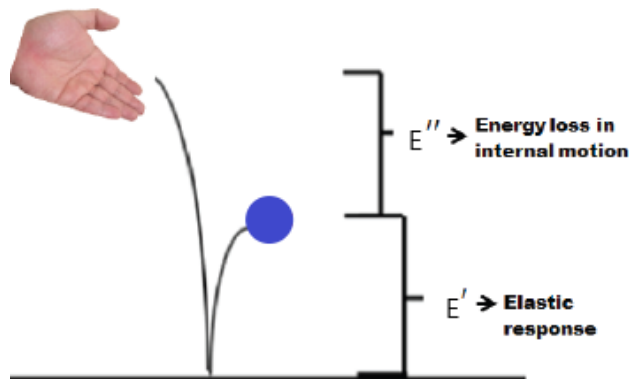
Figure 6.2: Storage and Loss Modulus Explanation

tionary fixtures, the test specimen is placed inside the thermal chamber in Figure 6.3b. A temperature range suitable for the material being evaluated, together with frequency and amplitude, are input. The analyzer slowly moves across the designated temperature range while applying tensional oscillation to the test sample. The testing machine contains following components:

Dynamic Mechanical Analyzer: A dynamic mechanical analyzer is used to measure the mechanical properties of a material as a function of time, temperature, and frequency. The dynamic mechanical analyzed consists of a sample holder, a load cell, a temperature-controlled chamber, and an oscillator. In the material laboratory, Gabo Eplexor 150N model DMA machine was used, in Figure 6.3a.

Film Gripper: A film gripper is used to hold the membrane securely in place during the DMA test. The film gripper is designed to apply a controlled amount of tension to the sample without causing any damage to the sample.

Temperature Controller: The temperature controller is used to regulate the temperature of the sample during the DMTA test. The temperature controller ensures that the sample remains at a constant temperature throughout the test.
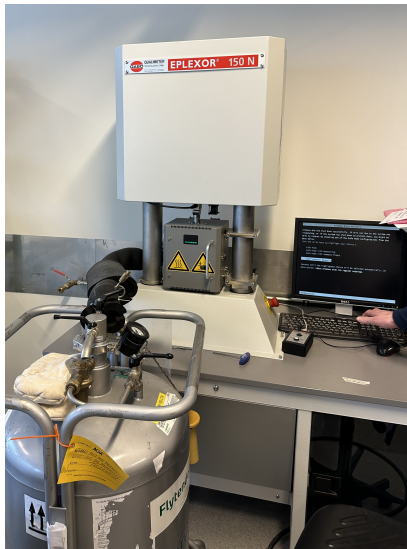
(a) DMTA Test Machine at the lab   (b) The Film Gripper inside the chamber
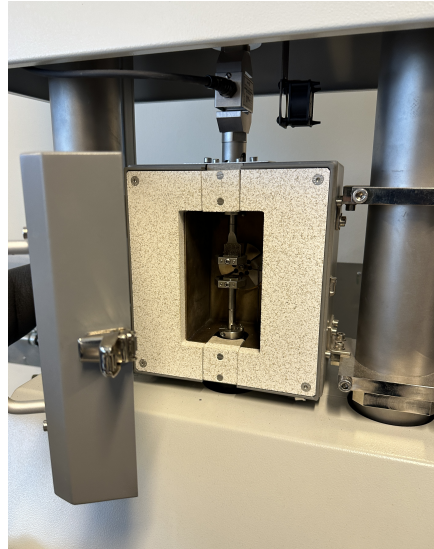
Figure 6.3: DMTA Machine

Oscillator: The oscillator is used to apply a small sinusoidal deformation to the sample at a specified frequency. The deformation is applied to the sample in either tension or compression mode.

Load Cell: A load cell is used to measure the force applied to the sample during the DMA test. The load cell is capable of measuring both the static and dynamic forces acting on the sample.

Amplifier: The amplifier is used to amplify the signal from the load cell and send it to the data acquisition system.

Data Acquisition System: The data acquisition system is used to collect and analyze the data from the DMA test. The system is capable of recording the temperature, frequency, and deformation data from the dynamic mechanical analyzer and the load data from the load cell.

Software: The software is used to control the analyzer and collect, analyze, and plot the data from the DMA test. The software is also used to calculate the viscoelastic properties of the membrane, such as storage modulus, loss modulus, and loss factor.

6.3 Specimens Preparation

6.3.1 Tensile Test

A total of 14 specimens were cut from the membrane(See in Figure 6.4a) for using in the tensile test to obtain statistical data. For the test, the rectangular specimens with dimensions of 150 mm length, 50 mm width, and 0.80 mm thickness were prepared. The specimens were cut by hand with a snap blade utility knife. After cutting, all specimens were measured with a caliper and a digital micrometer one-by-one to ensure correct dimensions. Table 1 was created to present the combined dimensions of all specimens. Prior to mounting the specimens onto the grips, they were uniformly coated with black spray paint (see Figure 6.4b) for the DIC analysis on Simlab eCorr software. The specimens were clamped onto the grips of a universal testing machine with a pneumatic clamping system, ensuring that the clamps were aligned and securely fastened. A pre-load of 10 N was applied to the specimen to eliminate any slack in the material, and then the tensile test was carried out at the velocity of 0.15, 1.5, 15 mm/s for the different strain rates until the sample broke. The UTM was equipped with a load cell that recorded the force applied to the specimen during the test, and a video camera was used to capture the deformation of the specimen.

There are three different specimen configuration as can be seen in Figure 6.4a: total eight longitudinal specimens and total six transversal specimens along the fiber direction. For describing the specimens' name shortly in the Table 6.2, "S" indicates the specimen, "A" indicates longitudinal direction, "T" indicates transversal direction and lower case "p" and "a" indicates pattern on the backside and 3° degrees tilted angle to the axis, respectively. Also, as the results for specimen S9Tp were missing, its successor in the analysis is considered to be S13Tp.

The experiment plan in Table 6.1 for the tensile test must be strictly followed to ensure that the specimens are tested under correct values. In addition, it is crucial to input the dimensions of the specimens into the UTM software on the laboratory computer before running the experiment for a specific specimen. Before painting the specimens, each side of the specimens was wrapped with tape to prevent dye from getting on the side where the grips clasp, as shown in Figure 6.5a. After the painting process was completed, the specimen was placed between the grip clamps in Figure 6.5b. Care should be taken while adjusting the membrane to ensure that it is parallel to both ends. Instead of clamping down both sides at the same time, it is more suitable to clamp down one side first while adjusting the ends.

In Table 6.1, measurements were taken at three different points on the specimens to determine their dimensions. The measurements were taken along the length-wise of the specimens, with d1a, d2A, and d3A indicating the dimensions at the top, center, and bottom points, respectively. The thickness of the same points were

Table 6.1: Tensile test experiment plan

Specimen Number	Strain Rate of the UTM	Dimensions (mm)					
		Top -50	Center	Bottom +50	Top -50	Center	Bottom +50
		d1A,a1	d2A,a2	d3A,a3	d1B,b1	d2B,b2	d3B,b3
S1A	10E-3	49.68	49.68	49.55	0.80	0.80	0.80
S2A	10E-2	49.65	49.69	49.69	0.80	0.80	0.80
S3A	10E-1	49.46	49.52	49.66	0.80	0.80	0.80
S4A	10E-2	49.82	49.80	49.95	0.80	0.80	0.80
S5A	10E-1	49.70	49.51	49.38	0.80	0.80	0.80
S6A	10E-3	49.78	49.73	49.77	0.80	0.80	0.80
S7Tp	10E-2	49.60	49.46	49.61	0.80	0.80	0.80
S8Ta	10E-2	49.87	49.57	49.57	0.80	0.80	0.80
S9Tp (Missing)	10E-2	49.65	49.38	49.18	0.80	0.80	0.80
S10Ta	10E-2	49.51	49.50	49.35	0.80	0.80	0.80
S11Tp	10E-2	49.68	49.53	49.24	0.80	0.80	0.80
S12Ta	10E-2	49.66	49.48	49.59	0.80	0.80	0.80
S13Tp	10E-2	49.16	49.32	49.31	0.80	0.80	0.80
S16A (Dogbone)	10E-2	30.50	30.60	30.57	0.80	0.80	0.80
S17A (Dogbone)	10E-3	30.30	30.59	30.30	0.80	0.80	0.80

(a) Cutting the specimens

(b) Painting Process

Figure 6.4: Specimen Preparation

indicated by d1B, d2B, and d3B, and they were also measured at the same locations as the lengthwise dimensions.

(a) Wrapping both ends
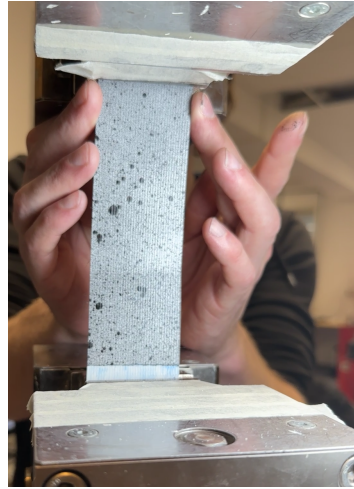
(b) Placing a specimen

Figure 6.5: Specimen preparation and placing

6.3.2 DMA

For the DMA test, the dimensions of the specimens are smaller than those used in the tensile test due to the size of the testing machine. The grips used in the DMA test are smaller and the dimensions of the specimens are determined accordingly. Typical specimen length should be 50 mm, with a width of 10 mm and a material thickness was 0.80 mm. The membrane piece used to cut out a total of 9 specimens can be seen in Figure 6.6. Dummy specimens were used to calibrate the machine and observe its effect with different frequencies. The DMTA test results do not includethe data from dummy specimens. Also, the machine do have a decent static capacity but the dynamical force amplitude could be in the range from 0-2 Mpa. Initially, we intended to conduct the test using the following static stress: 10 MPa, 40 MPa, and 70 MPa. However, we discovered that 70 MPa was excessively high since it led to the fibers being pulled out from the polymer sheath it can be seen in Figure 6.7b. The highest stress was then changed to 50 MPa. To manage with the low friction, we employed double-layered grit paper in Figure 6.7a, which had no effect on L0 or stiffness. With three samples each division, a total of nine valid samples were used in the test. The experiment plan is given in Table 6.2.

 Five measurements were made per decade during the typical test scenarios, which were conducted between 0.1 Hz and 50 Hz. However, a prolonged run was conducted using three samples, starting at a frequency of 0.01 Hz. The fibers were packed together in tiny clusters with space between them in the samples. This in-
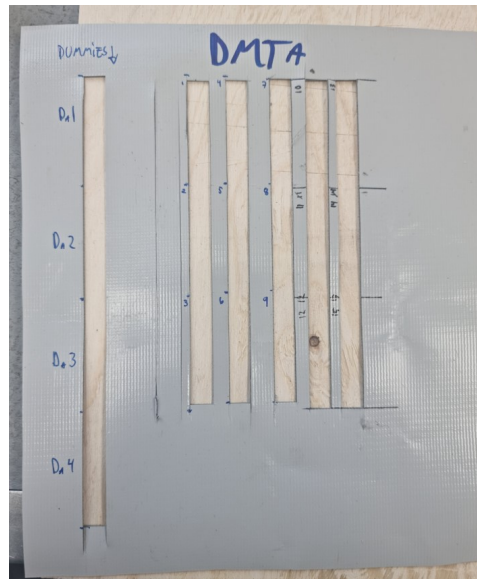
Figure 6.6: All the DMTA specimens cut out

Table 6.2: Dynamic Mechanical Thermal Analysis experiment plan

Specimen	Width [mm]	Thickness[mm]	Static Stress[MPa]
1	10.31	0.80	10E+-2
2	10.34	0.80	40+-2
3 (Failed)	10.40	0.80	70+-2
4	9.98	0.80	10+-2
5 (Failed)	9.95	0.80	40+-2
6 (Failed)	9.63	0.80	70+-2
7 (Failed)	10.08	0.80	70+-2
8	9.95	0.80	40+-2
9	9.92	0.80	50+-2
10	10.04	0.80	50+-2
11	9.98	0.80	50+-2
12	9.85	0.80	40+-2
13	9.93	0.80	10+-2

dicates that the cross-section strength is mostly determined by the integer of group members about 7 bundles at 10 mm in Figure 6.7b.

Small width changes that have no impact on the bundles are most likely insignif-
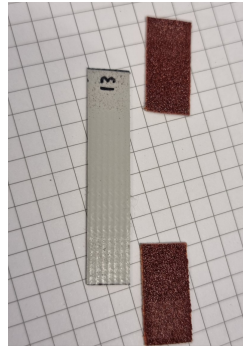
(a) Increasing friction   (b) Fibers came out
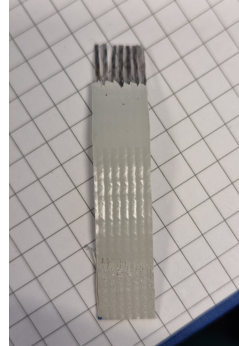
Figure 6.7: Specimen Preparation of DMTA Test

icant. The DMA cycles may cause a slight temperature increase in the material, however polymers are temperature sensitive. The temperature on the specimen rises as the frequency rises. The temperature in the data is the ambient temperature. The DMA test, also known as DMTA, was conducted at room temperature without considering different temperature levels. Hence, in this case, it can be referred to simply as DMA. The samples were tested starting from the lowest frequency. The specimens inside the chamber with and without sandpaper are shown in Figure 6.8.
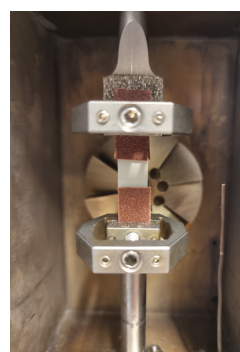
(a) Without sandpaper   (b) With sandpaper

Figure 6.8: The specimens are placed between the grips in the DMTA machine chamber

6.4   Experiment Results

The results obtained from the tensile test and DMA experiments are depicted in Figure 6.10 and Table 6.3, respectively. The presentation of the tensile test results is in graphical form due to the larger quantity and extended length of the result tables. Following the elucidation of the actual experimental data, these results will be compared with the simulation findings.

6.4.1   Tensile Test

The stress-strain curve of the membrane material showed an initial linear region, followed by a non-linear region up to the point of fracture. The modulus of elasticity was found to be 1331.56 MPa, the ultimate tensile strength was 94.57 MPa, and the elongation at break was 20.28%. The data obtained from the five specimens showed low variability, with a standard deviation of less than 5%. After analyzing the behavior of different specimens, the most representative one was selected based on the stress-strain graph 6.9. The chosen specimen is S2A with a strain rate of $10^{-2}s^{-1}$. Additionally, only the longitudinal specimens' stress-strain curve comparison can be seen in Figure A.1.

In longitudinal specimens at strain rates of $10^{-1}s^{-1}$ and $10^{-2}s^{-1}$, failures occurred primarily close to the grips, as depicted in Figure 6.10. At a strain rate of $10^{-1}s^{-1}$, some failures occurred inside the grips, resulting in higher stress at fracture. Additionally, we conducted extra axial specimens with a dogbone shape to determine if it was possible to reach higher stress and fracture for 10^{-2} and 10^{-3}. While this method is commonly used theoretically, it proved unhelpful for the membrane material, and other specimens achieved similar levels with the dogbone shapes.

In the Abaqus model, the data for the elastic and plastic regions are required to be input separately. Therefore, in Figure 6.9, the elastic and plastic regions are separated. The elastic region and yield strength are shown in yellow and are pointed out, respectively. The membrane material exhibits non-linear behavior as evident from the graph. Consequently, the elastic region of the material is narrower compared to linear behavior materials. The precise yield strength point is indicated on the graph and fracture occurs at the top of the curve as depicted. The yield strength is the stress at which the material begins to deform plastically. It is typically determined as the stress at which the curve deviates from the linear portion of the curve. This can be done by identifying the point on the curve where the slope changes. As previously stated, the stress-strain curve of specimen S2A was identified as the most representative. Hence, the Abaqus model was developed based on the properties of this particular specimen.

In the stress-strain curve of the most representative specimen shown in Figure 6.9,
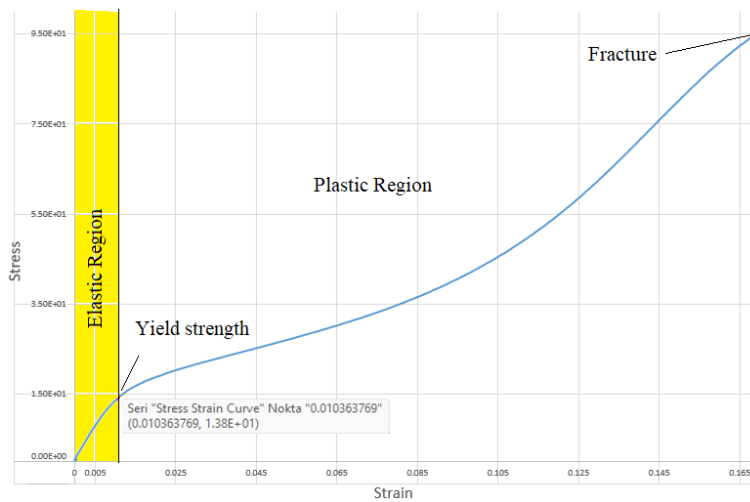
Figure 6.9: Stress Strain Curve of the most representative specimen S2A

the plastic behavior of the material is considered beyond the yield strength point. Accurate material behavior data is crucial in ABAQUS to accurately represent the material's response in the model. Therefore, true stress and true strain values were utilized in the tensile test model to ensure the model captures the correct material behavior instead of the engineering stress and strain curve. Using true stress-strain values is recommended because the model gives a realistic behaviour of the material properties. The difference between the curves can be seen in Figure A.2.

Figure 6.10: All the tensile test specimens (Left to right: S1A to S17A)

By dividing F by the cross-sectional area A_0 of the deformed specimen, the engineering stress σ is calculated in Equation 6.1. After yield has begun, the engineering stress in ductile materials becomes obvious and is inversely related to the force (F) decreasing throughout the necking phase. It is noticed that the true stress σ_t (Equation 6.2), which is proportional to F and inversely related to A, keeps rising until the specimen ruptures. By dividing the tensile load by the instantaneous area, engineering strain is calculated. The natural logarithm of the difference between the instantaneous length and the initial length is true strain. The non-uniform deformation that takes place in a material at high strain rates is taken into account by true strain.

$$\underline{\text{Engineering}} \rightarrow \text{Stress} = \sigma = F/A_0 \textbf{ and } \text{Strain} = \varepsilon = \delta/L_0 \qquad (6.1)$$

$$\underline{\text{True}} \rightarrow \text{Stress} = \sigma_t = F/A \textbf{ and } \text{Strain} = \varepsilon_t = \ln(L/L_0) \qquad (6.2)$$

For the pattern on the back side specimen configuration did not show any differ-
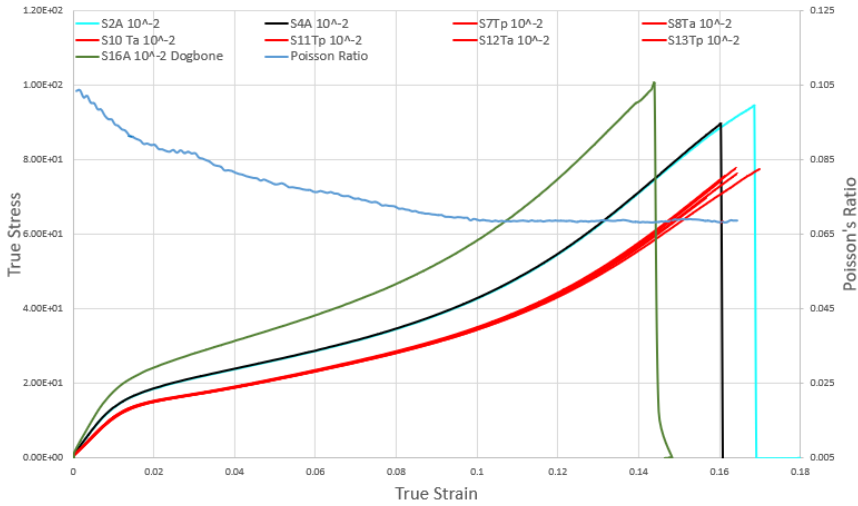
Figure 6.11: Stress-Strain for Longitudinal and Transversal Specimens at $10^{-2} \ s^{-1}$

ence with the normal transversal specimens. For the tilted specimen has negligible difference. It can be seen in graph for all the $10^{-2}s^{-1}$ strain rate specimens in Figure 6.11.

Digital Image Correlation

The Digital Image Correlation (DIC) method is used instead of an extensometer. In eCorr software, two vectors are identified on the specimens using high-quality photos taken during the tensile test experiment. These vectors function as a virtual

extensometer, providing all the necessary information about the tensile test. The figure with the DIC vectors is shown below 6.12b, and for reference points comparison with the point in the numerical model, the figure 6.12c is given below.

Virtual extensometers were used in DIC software to measure the strain of the membrane specimens during the tensile test. Only two vectors were needed to calculate displacement and vector elongation in the software. In the ABAQUS model, a total of four reference points were marked on the surface of the specimens to define a consistent region of interest for strain measurements. The reference points were selected as accurately as possible in the exact location for measuring the strains in the simulated tensile test.

The comparison between the model and the tensile test experiment results can be observed in Figure 8.1. This figure provides a comprehensive overview of the six sequential figures, showcasing the alignment between the simulation and experimental data. The figures represent results obtained from three specific points, which were simultaneously captured during both the simulation and the tensile test experiment. The exact locations of these points are indicated in Figure 8.2. This comparison allows for a detailed analysis of the consistency and agreement between the model predictions and the experimental observations, providing valuable insights into the accuracy and reliability of the model in simulating the mechanical behavior of the material under tensile loading conditions. The element type of the ABAQUS model is 'M3D4R' which means a 4 node quadrilateral machine, reduced integration, hourglass control.

(a) Without mesh   (b) Virtual extensometer   (c) Abaqus model
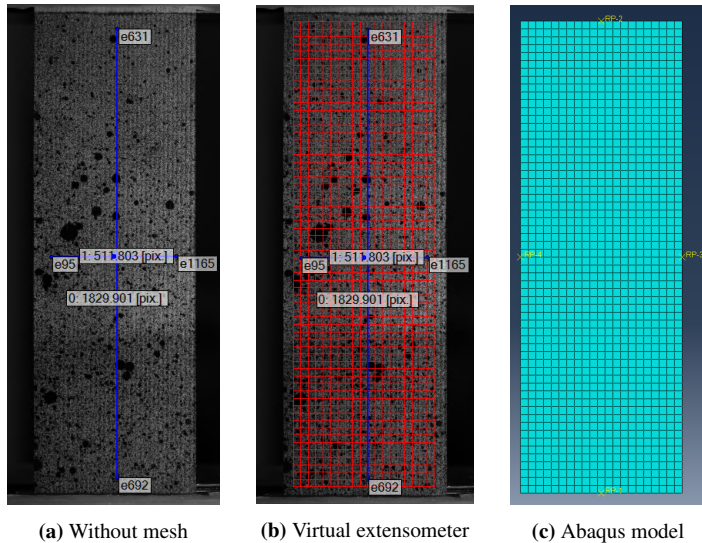
Figure 6.12: Virtual extensometer on DIC and Reference Points on ABAQUS Model

6.4.2 DMTA

The results from the DMTA test is obtained directly from the Gabo Eplexor 150
DMTA machine software. After every experiment run, the software creates the
table for the necessary values such as initial and final length for every steps, fre-
quency, temperature, tan δ, storage modulus (E'), loss modulus (E") and complex
modulus (E*). There are more values in table that creates by software but these
values are not necessary for the current model.

Table 6.3 presents the results of the most reliable specimen, while the results of
the remaining specimens will be presented in Appendix A. It is worth noting that
when comparing the chosen specimen with others, caution must be exercised due
to potential errors encountered at high static stress values. To ensure an accurate
demonstration of the DMA material model, a static stress level of 10 MPa was
selected.

  Figure 6.13 shows that 4 out of 13 specimens, which are number 3, 5, 6 and
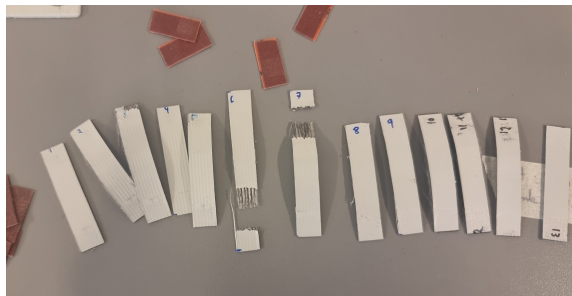
Figure 6.13: All DMA specimens after the test runs

7, were failed due to the high static stress applied. Therefore, only nine speci-
mens were taken into account. As shown in Table 6.3, the static stress represents
the initial stress load applied to the specimen. The dynamic stress values, on the
other hand indicate the incremental and decremental cyclic loading at each peak
and trough point of the sinusoidal curve, simulating the cyclic loading behavior of
material. For a clearer comparison of the material behavior in Figure 6.14 display
the frequency values and the normalized storage modulus for showing the curves
more clearly in logaritmic scale. The normalized storage modulus is calculated by
dividing each storage modulus value by the highest storage modulus value for the
corresponding specimen. This normalization allows for a better understanding of
the relative differences in storage modulus across different specimens.

Table 6.3: DMA Test Results of the most representative specimen S1L

No	Stress Static [MPa]	L_0 [mm]	L_m [mm]	Stress Dynamic [MPa]	f [Hz]	T [^oC]	tanδ	E' [MPa]	E'' [MPa]	$|E^*|$ [MPa]
1	9.96875	30.0861	30.3581	1.98661	0.01	24.5448	0.057085	1.05E+03	60.02376	1.05E+03
2	9.99331	30.2497	30.4963	2.03276	0.01585	24.5449	0.061708	1.05E+03	64.7678	1.05E+03
3	10.0075	30.3001	30.5535	1.99631	0.02512	24.7577	0.057175	1.08E+03	61.52502	1.08E+03
4	9.98685	30.3244	30.5816	2.00152	0.03981	24.4991	0.05437	1.10E+03	59.78685	1.10E+03
5	9.99073	30.3365	30.5953	1.99507	0.0631	24.53	0.050699	1.12E+03	56.67392	1.12E+03
6	9.99202	30.3439	30.6036	1.9972	0.1	24.5144	0.04873	1.13E+03	55.26762	1.14E+03
7	9.99202	30.3492	30.6081	1.99173	0.15849	24.53	0.047464	1.15E+03	54.50606	1.15E+03
8	9.98168	30.3523	30.6106	1.99684	0.25119	24.5148	0.045713	1.16E+03	53.13671	1.16E+03
9	9.98556	30.3529	30.6118	1.99441	0.39811	24.3785	0.045522	1.18E+03	53.48978	1.18E+03
10	9.98943	30.3534	30.6128	1.9974	0.63096	24.4384	0.045152	1.19E+03	53.59182	1.19E+03
11	9.98426	30.3535	30.6128	1.99297	1	24.4232	0.044883	1.20E+03	53.7899	1.20E+03
12	9.99202	30.3536	30.6131	2.00386	1.58489	24.408	0.044339	1.21E+03	53.63255	1.21E+03
13	9.98168	30.3527	30.6126	1.99432	2.51189	24.4844	0.04424	1.22E+03	54.00259	1.22E+03
14	9.99202	30.3512	30.6123	1.99581	3.98107	24.4841	0.044747	1.23E+03	55.13223	1.23E+03
15	9.98814	30.3508	30.6117	1.9993	6.30957	24.469	0.044021	1.24E+03	54.74326	1.24E+03
16	9.98556	30.3502	30.6111	1.9949	10	24.4844	0.045318	1.25E+03	56.85243	1.26E+03
17	9.98685	30.3489	30.6101	1.99362	15.8489	24.5901	0.047533	1.27E+03	60.17096	1.27E+03
18	9.99202	30.3477	30.6094	1.99323	25.1189	24.5904	0.051134	1.28E+03	65.32157	1.28E+03
19	9.99073	30.3447	30.6079	1.98852	39.8107	24.6056	0.055975	1.29E+03	72.1709	1.29E+03
20	9.97651	30.3445	30.607	2.00461	50	24.56	0.060194	1.30E+03	77.95807	1.30E+03
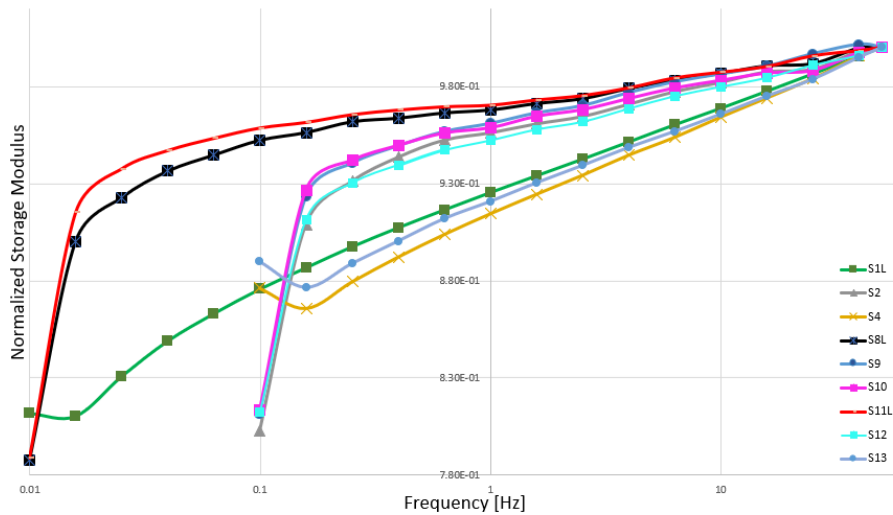
Figure 6.14: All the DMA specimens in logaritmic scale

6.4.3 Regression Study Between Experimental Results

Regression study is a process of comparing and analyzing data from two or more sources to determine the degree of similarity or agreement between them. In the context of the membrane experiment test, a regression study would involve comparing the experimental data of alt the specimens that have collected.

The stress-strain curve was calculated by dividing the recorded load by the initial cross-sectional area of the specimen and the modulus of elasticity was calculated from the slope of the linear portion of the stress-strain curve. The ultimate tensile strength was determined from the maximum stress observed in the stress-strain curve and the elongation at break was calculated from the percentage of strain at the point where the specimen ruptured.

While choosing the most representative specimen, all specimens were compared based on their strain rate and test direction. A small MATLAB script (A.4) was used to find the regression line between specimens with the same strain rate. Ultimately, specimens with the same strain rate and tensile test direction were compared to each other. As shown in the comparison graphs below for longitudinal and transversal directions in Figures 6.15, 6.16, the results from the tensile tests are very close to each other. There were several specimens used in the experiment, but some of them exhibited different or undesirable behavior. Therefore, the S2A specimen was chosen for use in the model.
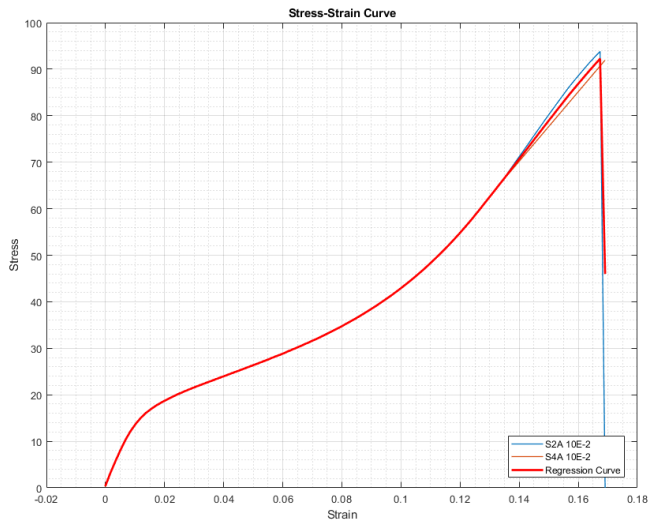
Figure 6.15: Longitudinal Specimens
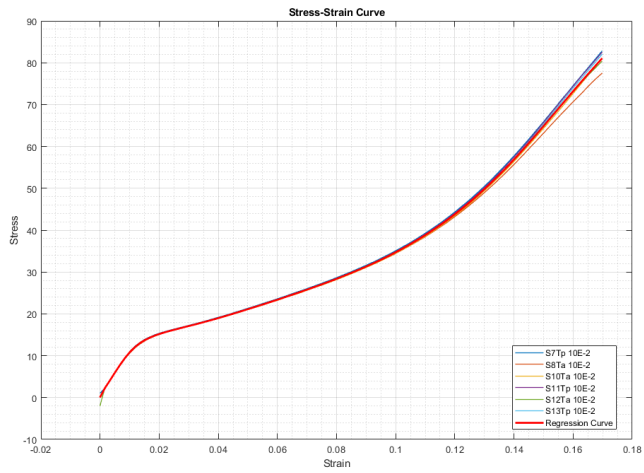
Figure 6.16: Transversal Specimens

Numerical Modelling

7.1 Modelling in ABAQUS

7.1.1 Background for the Modelling

As a background, the idea of the work is to look at how different models in ABAQUS Explicit can represent what we observed experimentally. We have been choosing to look at the elasto-plastic model with failure and the hyperfoam model with adding viscoelasticity. The material type was chosen as membrane for both models.

7.1.2 Elasto-plastic Model with Failure

The test setup is created as a starting point with the help of the real test and specimen preparation is which explains in Section 6. Analysing a non-linear model requires advanced techniques for membrane structural behaviour.

The ABAQUS model was created in regard of the real specimens' dimensions and behaviour. The purpose of creating the model was to make comparison between the real experimental and the simulation results. The name of the material type was not given before the experiment or creating simulation. The model was built based on the results of tensile test. The mesh size was decided according to the mesh size which was used on DIC software. The ABAQUS Model' material properties are given in Table 7.1 There were several models created during the process of finalizing the model. Different mesh sizes and specimen results were used and ultimately the most optimal and the representative specimen was chosen for numerical modeling out of 14 specimens. The mesh size was selected based on the

Table 7.1: Tensile test material properties from the test

Properties		Unit
Young's Modulus	1331,56	MPa
Poisson's Ratio	0.08	
Yield Strength	1,38E+01	MPa
Initial Length	150	mm
Initial Width	50	mm
Thickness	0.80	mm
Density	1E-09	g/cm^3

size obtained from DIC measurements to achieve the closest results. Various mesh sizes were tested, including 1 mm, 2.5 mm, 3 mm and 4 mm. In the end a mesh size of 2.5 mm was chosen.

The Young's modulus E (7.1) is calculated by dividing the true stress (σ) by the true strain (ε) in the linear portion of the stress-strain curve. Mathematically it can be expressed as:

$$E = \frac{Stress}{Strain} = \frac{\sigma}{\varepsilon}$$

(7.1)

The Young's modulus represents the stiffness or rigidity of a material and describes its ability to resist deformation under an applied load in the elastic domain. By calculating the Young's modulus from the stress-strain data, we can quantitatively assess the material's elasticity and its response to external forces.

All the material properties 7.1 were calculated with tensile test results and the calibrations were made according to them. The Poisson's ratio ν is relatively low for membrane materials compared to other types of materials. This characteristic can be attributed to the nature of the membrane material, which involves a coated fabric structure.

Equation of the Poisson's ratio shows in Equation 7.2. So, for the tensile test abaqus model, the Poisson's ratio is taken as 0.08. The stress-strain curve of the most representative specimens with the Poisson's ratio are presented together in Figure 7.1. By examining these two parameters on the same graph, correlations between the material's mechanical behavior and its lateral contraction characteristics can be observed. This comparative analysis enables the identification of potential relationships or differences between the material's stress-strain response and its behavior in terms of lateral deformation. The full Poisson ratio curves of the some of the specimens can be seen in Figure B.1.

$$\nu = -\frac{\varepsilon_{transversal}}{\varepsilon_{longitudinal}}$$

(7.2)

The stress triaxiality equation 7.3 provides a quantitative measure of the stress
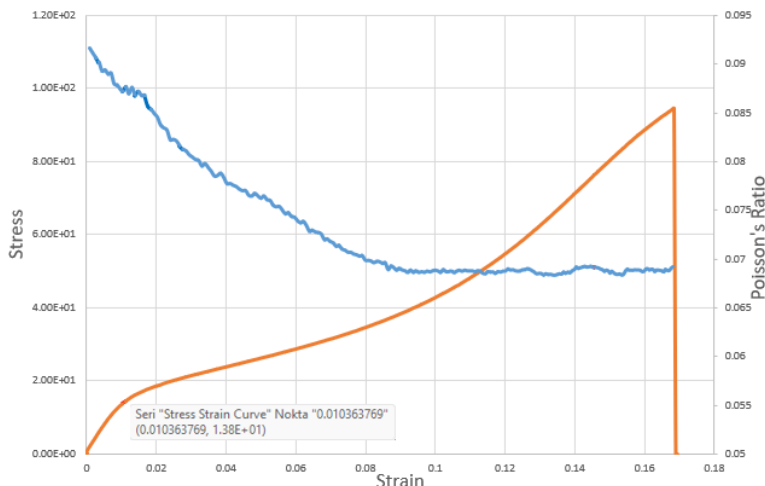
Figure 7.1: Stress Strain Curve and Poisson's Ratio

state in a material under different loading conditions. In the context of a uniaxial tensile test on a membrane material, where there are no additional forces or pressures applied, the stress triaxiality value is determined solely by the vertical load along the z-axis. The loads along the x and y axes are considered to be zero since there is no external load in those directions. The stress triaxiality value is an important parameter in analyzing material behavior and understanding its response to various loading conditions [73]:

$$\nabla_h = \frac{\sigma_I + \sigma_{II} + \sigma_{III}}{3 \cdot \sigma_{mises}} \tag{7.3}$$

where σ_I, σ_{II}, σ_{III} indicate the principal stress notions. Based on the load distribution along the axes, the stress triaxiality value for the model can be calculated using Equation 7.3. This calculation is possible because the load applied to the model is equivalent to the Von Mises stress value. In the case of uniaxial tensile tests, it is common practice to use a stress triaxiality value of 1/3 [73]. In simulating the model, specifying the fracture strain is crucial for accurately representing rupture initiation. The fracture strain which indicates the Von Mises equivalent strain at the onset of fracture plays a significant role in characterizing the material's ductility under loading. In ABAQUS, the fracture strain is determined within the ductile damage section of the simulation where the progression of damage and eventual fracture can be observed. By incorporating the fracture strain into the model, the simulation can effectively capture the material's behavior until the point of rupture. In cases where specific biaxial or compression test results are

unavailable, estimating the fracture strain can be challenging. However, it is still possible to approximate the fracture point by fitting the stress-strain curve obtained from experimental data.

By analyzing the experimental curve and identifying the point where fracture occurs, an approximate fracture strain can be determined. This fracture strain value can then be used in the simulation to represent the rupture behavior even though it may not be an exact match to the experimental fracture strain. In the experimental results, the fracture strain of the representative specimen was measured as 0.1685. However, during the simulation, the fracture strain value of 0.112 was chosen to improve the fitting to the stress-strain curves. This adjustment was made in order to achieve better agreement between the experimental and simulated curves. While the chosen fracture strain in the simulation may not match the exact value from the experiment, it was selected to enhance the overall accuracy of the curve fitting process.

(a) Dimensions of the model   **(b)** Boundary Conditions
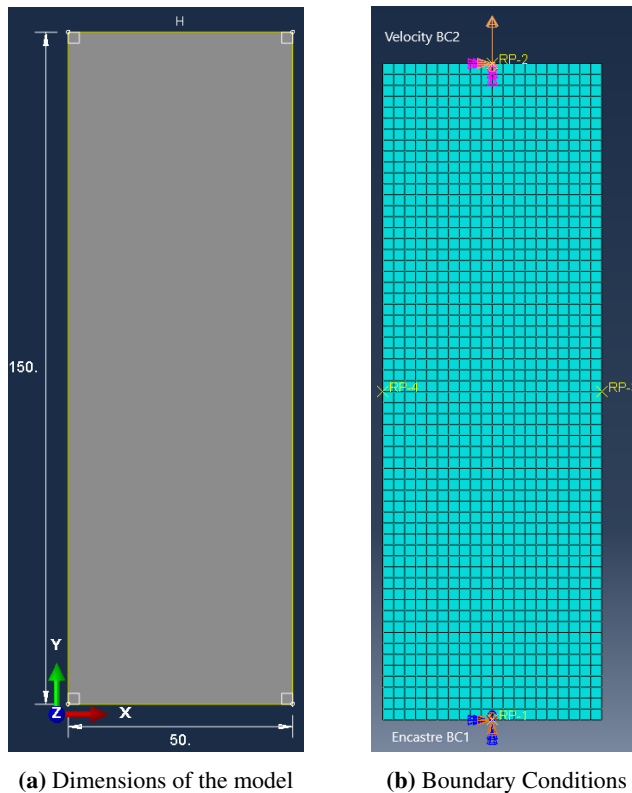
Figure 7.2: Elastoplastic Model Properties

In Abaqus, constraints were used to specify the boundary conditions and interactions between different parts or surfaces of a model. These constraints ensure that the model behaves as desired and accurately represents the physical behavior of the system [45]. For simulating the tensile test behavior of the material, there are two reference points: Reference Point 1 at the bottom end and Reference Point 2 at the top end. These reference points serve as constraints having connection with ends. Reference Point 1 is constrained to the bottom end, which means it is fixed and cannot move. This constraint represents the fixed boundary condition at the bottom of the specimen, where it is typically clamped or held in place during a tensile test. Reference Point 2 is constrained to the top end, but it is allowed to move with a velocity of 1.5 mm/s. This constraint represents the applied velocity or angular velocity at the top of the specimen, where the machine pulls the material at a specified velocity. By applying this constraint, the model simulates the tensile test behavior of the material, where the top end is subjected to controlled displacement. By incorporating these constraints in your Abaqus model, you can accurately simulate the tensile test behavior of the material.

For the boundary conditions, the bottom end condition was taken as encastre so it can not move. Because there is no force/velocity on the point. For the top end, the condition is taken as uniform velocity. To calculate the velocity of the machine pulling the material, the strain rate and the initial length of the specimen can be used. The strain rate is defined as the rate of change of strain with respect to time.

$$\varepsilon_{membrane} = \frac{\Delta\varepsilon}{\Delta t} \tag{7.4}$$

In this case, the strain rate was given as $10^{-2}s^{-1}$ and the initial length of the specimen (L_0) was 150 mm. To find the velocity, it is necessary to relate the strain rate to the machine's velocity. The velocity (v) can be calculated using the formula 7.5:

$$v = \varepsilon_{membrane} \cdot L_0 = 1E - 2 \cdot 150mm = 1.5mm/s \tag{7.5}$$

where L_0 is the initial length of the specimen.

Elasto-plastic Model Calibration

As stated previously, calibrating the tensile test simulation is a challenging task in the absence of bi-axial and compression experiments data. The difficulty arises from the complexity of predicting and understanding the behavior occurring within the thickness of the material. Without comprehensive data from these additional experiments, accurately capturing and modeling the intricate mechanical responses during the tensile test becomes a formidable task.

The material had a thickness of 0.8 mm, but its different behavior in the thick-

ness direction could not be measured. Therefore, the tensile simulation needs to calibrate with adjustment on the values of yield stress and plastic strain. Figure 7.3 illustrates the stress-strain curve obtained from the actual experimental results and the calibration of the model, which initially exhibited high stress values. The calibrated input data curve shown in Figure 7.3 indicates the values used for calibrating the elastoplastic model. After calibration, the model satisfies the necessary conditions and successfully achieves a close fit with the experimental stress-strain curve, as shown in the same figure. Those three curves show three different stress-strain values which are for the calibrated simulation data, experimental results data and calibrated simulation results.

To achieve convergence on the stress-strain curves, a coefficient C was utilized to
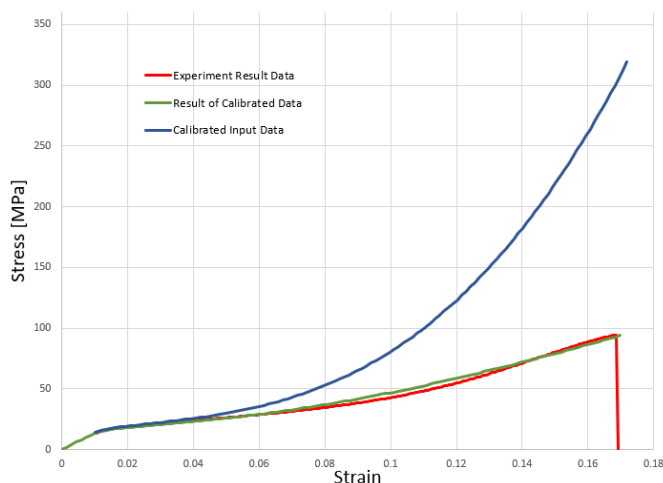
Figure 7.3: Elastoplastic model simulation calibration

calibrate the curve. The value of coefficient C depends on the behavior of the material and gradually increases until a satisfactory curve fit is obtained. C was taken as 30000. Equation 7.6 is employed to determine the optimal stress values for the curve. This equation assists in refining the stress-strain relationship and ensuring that the simulated curve closely matches the experimental data. By adjusting the coefficient C, the stress-strain curves can be fine-tuned to achieve convergence and accurately represent the material's behavior. All the calibrated stress values were increased by a constant factor of 2 in order to achieve a better fit at the beginning of the curve. This adjustment was made to ensure that the simulated stress-strain curve closely matched the experimental data in the early stages of deformation.

$$\sigma_{calibrated} = (\sigma_{abaqus}) + (C \cdot (\varepsilon_{new} - \varepsilon_{first})^3) \qquad (7.6)$$

In equation 7.6, σ_{abaqus} indicates the results of the elasto-plastic model before the calibration. The calibrated curve was based on the same plastic strain values, but it was necessary to subtract the initial strain value, denoted as σ_{first}, from the data. By subtracting this initial stress value, the focus is solely on the plastic deformation of the material and eliminating any contributions from the initial elastic response. This adjustment allows for a more accurate representation of the plastic strain behavior and helps to isolate the material's true plastic deformation characteristics during the simulation.

7.1.3 Hyperfoam Model Calibration from the Tensile Test

The purpose of the hyperfoam tensile test was to examine the behavior of a smaller-sized material under the same stress-strain conditions as the experimental data. The dimensions of the specimen were 30 mm in length and 10 mm in width. To ensure a consistent strain rate of $10^{-2}s^{-1}$, the test was conducted at a velocity of 0.3 mm/s, which was calculated based on Equation 7.7:

$$v = \varepsilon_{membrane} \cdot L_0 = 10^{-2} \cdot 30mm = 0.3mm/s \tag{7.7}$$

Figure 7.4 compares the hyperfoam tensile model with experimental data. The model closely matches the experimental stress-strain curve, indicating a good fit. For a comprehensive comparison of different models and experimental results, refer to Appendix B, featuring Figure B.2 demonstrating the consistency between the elastoplastic model, hyperfoam tensile model, and experimental results. The fitting procedure for the hyperfoam material with $N = 3$ was supported with the ABAQUS evaluate option and the hyperfoam coefficients were added in Table B.1.
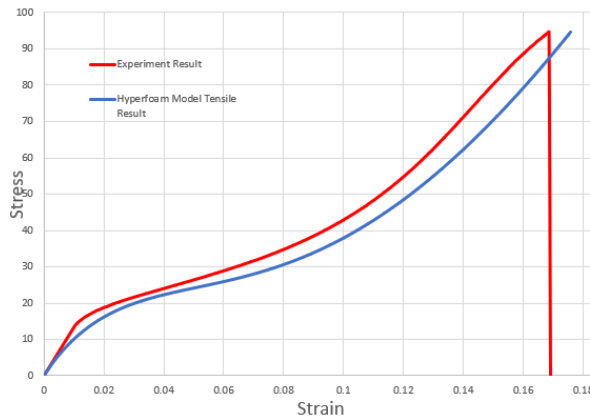
Figure 7.4: Stress Strain Curve: Hyperfoam model vs Experiment Result

7.1.4 Incorporating Viscoelasticity into the Hyperfoam Model

On the model, two boundary conditions were applied on the both ends, 10 MPa load were applied on the top end and nothing was applied on the bottom end because we want to keep the bottom end fixed. The mesh size was 0.5 mm due to the size of the model which was 30 mm length and 10 mm width with 0.8 mm thickness. The dimensions and mesh size can be seen in Figures 7.5.

Table 7.2: DMA Material Properties

Properties		Unit
Initial Length	30	mm
Initial Width	10	mm
Thickness	0.80	mm
Cyclic Load	10 ± 2	MPa

The same material properties were used for both experiments, ensuring consistency between the two. However, the dimensions of the models were adjusted to accommodate the respective test machines. In the ABAQUS modeling of the DMA test, the boundary conditions differed from those of the tensile test (see Figure 7.5b). The DMA test machine applied cyclic loads to the material and once the material reached a steady-state behavior, the corresponding values were recorded and presented in a table by the DMA software. The applied load on the model was determined based on the experimental input data where 10 MPa of applied stress corresponds to 7.95 N of load.

Hyperfoam Model Calibration with Added Viscoelasticity

During the calibration process of the Dynamic Mechanical Analysis (DMA) model, it is necessary to determine the Prony series coefficients for the viscoelastic material being studied. In ABAQUS, the viscoelastic behavior is modeled using a Prony series expansion as defined in Equation (7.8) which represents the dimensionless relaxation modulus of the material. This allows for an accurate representation of the material's viscoelastic response in the simulation. In DMA tests, the material sample is subjected to a sinusoidal stress or strain input and the resulting stress or strain response is measured. By utilizing the Prony series, the viscoelastic behavior of the material under these dynamic loading conditions can be effectively modeled. The Prony series captures the material's response by combining exponential functions with different relaxation times referred to as Prony terms [45].

(a) Dimensions of the model   **(b)** Boundary Conditions
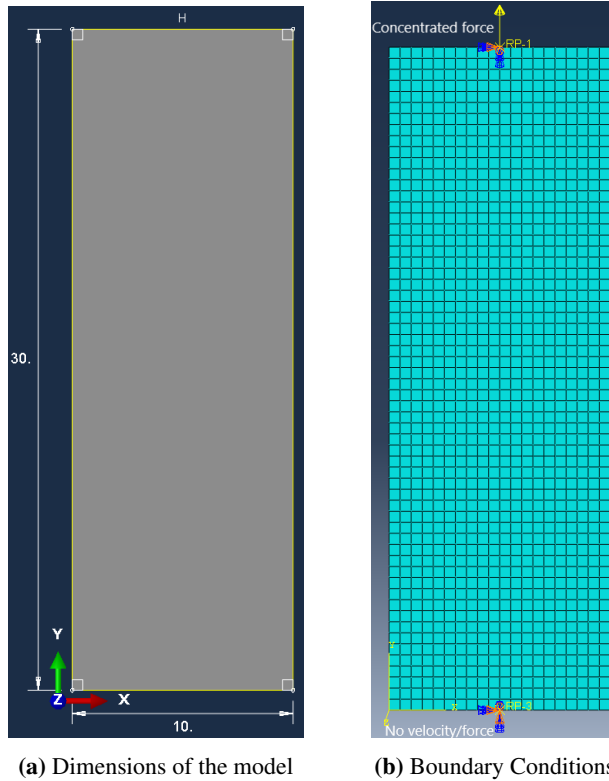
Figure 7.5: Dimensions of the model and the boundary conditions

$$G_R(f) = G_0 \left(1 - \sum_{i=1}^{N} \bar{g}_i{}^P (1 - e^{-t/\tau_i^f}) \right) \qquad (7.8)$$

The material constants denoted as N, $\bar{g}_i{}^P$ and τ_i^f where i = 1, 2, 3, ..., N, are inherent properties of the material. In my model, the value of G_0 was assigned as the maximum storage modulus obtained from the experimental data, representing the material's characteristic behavior. Only the storage modulus is considered in the model as it is the dominant component while the loss modulus is deemed negligible in comparison. By a factor of 30 or more, the loss modulus values are small in compared to the storage modulus values. This is also obvious in $tan\delta$ values that are getting close to zero in Table 6.3. Because storage modulus represents being dominant behavior, it is exceedingly difficult to obtain a decent estimate with a loss modulus curve. In this paper, just the storage modulus curve approximation was considered [13]. The number of parameters, τ_i, in the Prony series expansion depends on the desired number of terms in the model. For the Abaqus model,

three terms were utilized, although a greater number of terms can be employed if necessary. After three terms were utilized, Equation 7.8 is turned out:

$$G_R(f) = G_0 \left(1 - \bar{g_1}^P(1 - e^{-t/\tau_1^f}) - \bar{g_2}^P(1 - e^{-t/\tau_2^f}) - \bar{g_3}^P(1 - e^{-t/\tau_3^f})\right) \quad (7.9)$$

In equation 7.9 is used in the code in Appendix B.1. A fitting operation is carried out using the given code to get the Prony coefficients for a Prony series equation that models a material's viscoelastic behavior. The code creates an equation and a cost function for the fitting procedure after reading experimental data on storage modulus and frequency from an Excel file. The squared discrepancies between the experimental data and the predicted values from the Prony series equation was minimized iteratively by adjusting the fitting parameters using the 'fminsearch' function. Initial guesses for the fitting parameters are defined in the 'initial_params' array. For each page in the Excel file contains S1L, S8L and S11L specimens' experimental data. The fitted parameters G_0, g_1, tau_1, g_2, tau_2, g_3, and tau_3 are found based on the page numbers, respectively. The Prony coefficients may be calculated using this method, giving important information about the material's viscoelastic characteristics. The results are given in Table 7.3. Other prony coefficinets which were obtained for S8L and S11L is given in Figure B.2.

In ABAQUS, the rate-independent part of the material behavior, specifically the

Table 7.3: Prony series data for S1L Specimen

	g_i	tau_i
1	0.052623	0.075738
2	0.051902	1.2729
3	0.11114	34.6083

elastic moduli, needs to be specified. For small-strain linear elastic behavior, an elastic material model is used. For large-deformation behavior, either a hyperelastic or hyperfoam material model is employed. The rate-independent elasticity of these models can be defined using either instantaneous elastic moduli or long-term elastic moduli. The decision to use instantaneous or long-term moduli is merely a matter of convenience and does not affect the solution [45].

In the simulation, the mass scaling parameter plays a crucial role as it instructs Abaqus not to utilize the initial time step that is automatically calculated. Mass scaling allows for better control over the time step used in the analysis. Therefore, specifying the mass scaling value, the time step can be adjusted to ensure accurate and stable simulation results. This aspect can indeed be tricky, especially when considering dynamic motions of the specimen. In quasi-static simulations, such as the one described, it is possible to implement mass scaling effectively. If the simulation involves smaller frequencies or longer time series, adjusting the mass

scaling can be beneficial. As the time scale increases, using a larger mass scaling value can help maintain numerical stability and improve computational efficiency.

Figure 7.6 demonstrates the comparison between the DMA experiment results
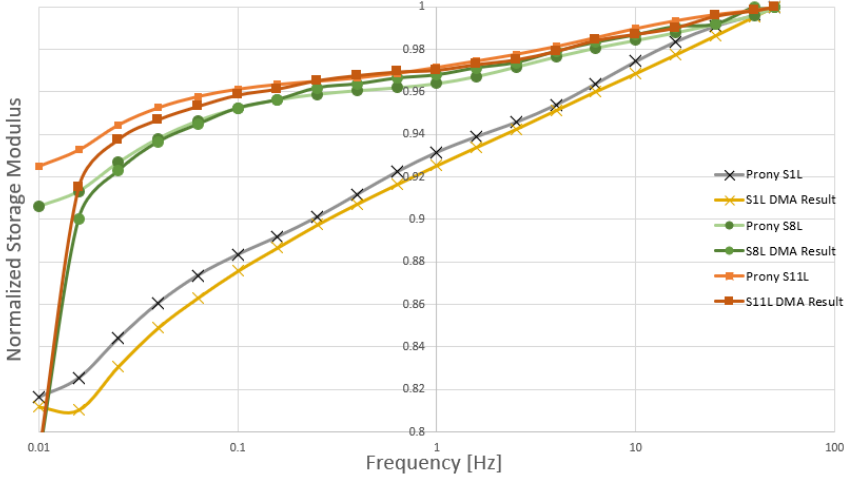
Figure 7.6: Comparison: Extended DMA specimens vs Prony code obtained results

and the results obtained from the Prony code. The storage modulus values, along with their corresponding frequencies, are provided in Table B.3. This analysis allows for an assessment of the accuracy and agreement between the experimental data and the simulation results obtained through the Prony code.

Chapter 8

Results and Discussion

8.1 Comparison with the Experiment Results

This chapter presents the results obtained from the simulations and experiments discussed in the previous sections. A thorough analysis and discussion are provided for each simulation, where the results are compared with the corresponding experimental data. The presentation of these results aims to demonstrate the findings and insights derived from the simulations emphasizing their relevance and importance in understanding the mechanical behavior of the materials under investigation.

8.1.1 Tensile Test

The engineering stress and strain data obtained from the tensile test were utilized in creating a numerical model using ABAQUS software. The resulting numerical model was then compared to the captured photos from the DIC software in three steps. This comparison provides valuable insights into the accuracy and effectiveness of the numerical model in simulating the mechanical behavior of the material, allowing for a comprehensive evaluation of its performance throughout the entire deformation process.
Figure 8.1 shows the comparison of the specific frames on the DIC software and on the elastoplastic ABAQUS simulation results.

89

(a) At yield strength   **(b)** In the middle   **(c)** Before fracture

(d) At yield strength   **(e)** In the middle   **(f)** Before fracture
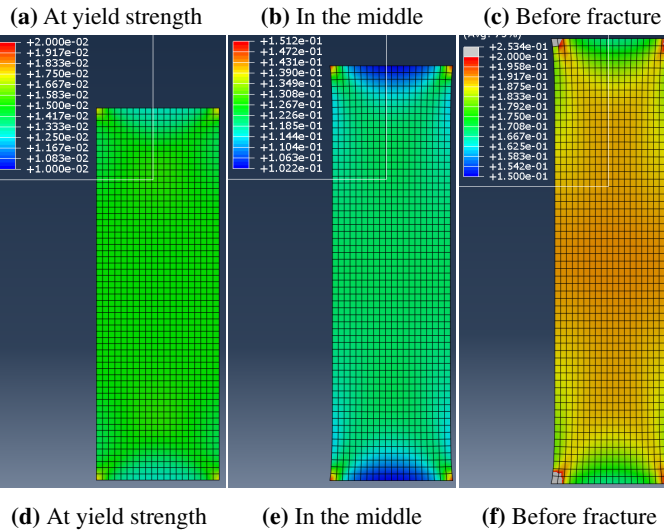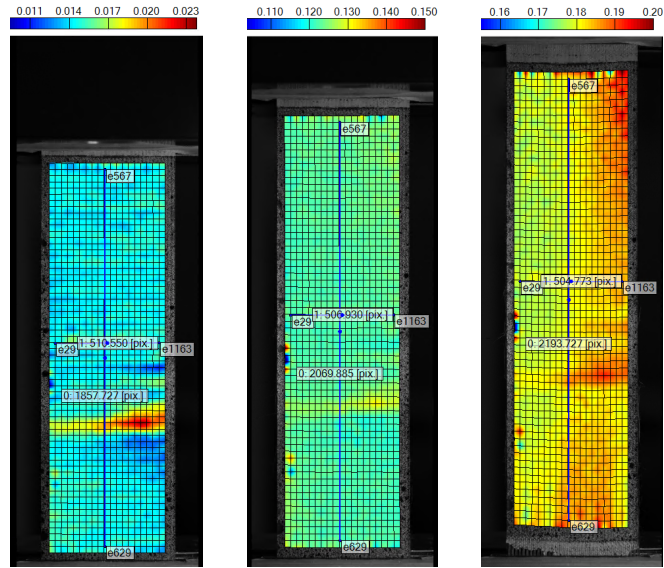
Figure 8.1: Strain distribution: Tensile Test vs Elasto-plastic model

Boundary issues were observed at the ends of the experimental specimens, particularly at high strain rates, resulting in discrepancies in the strain distribution. The absence of mesh application to the specimen's sides, despite using identical mesh sizes in the model and DIC software, further affected the accuracy of strain representation in those regions. The elastoplastic model demonstrated a satisfactory alignment with the results of the tensile test and the hyperfoam model tensile

results, as illustrated in Figure 8.2. This visual comparison serves as evidence for the agreement and similarity observed between the simulated data generated by the elastoplastic and hyperfoam models, and the experimental data obtained from the tensile test. Such a comprehensive assessment solidifies the accuracy and reliability of both the elastoplastic and hyperfoam models. The figure also indicates the specific point where the frames for the DIC analysis and the elastoplastic simulation were captured for Figure 8.1.

Certainly, in Appendix B, Figure B.2 was presented, specifically highlighting the comparison between the elastoplastic model and the experimental results of the tensile test. This separate figure allows for a clearer visualization.
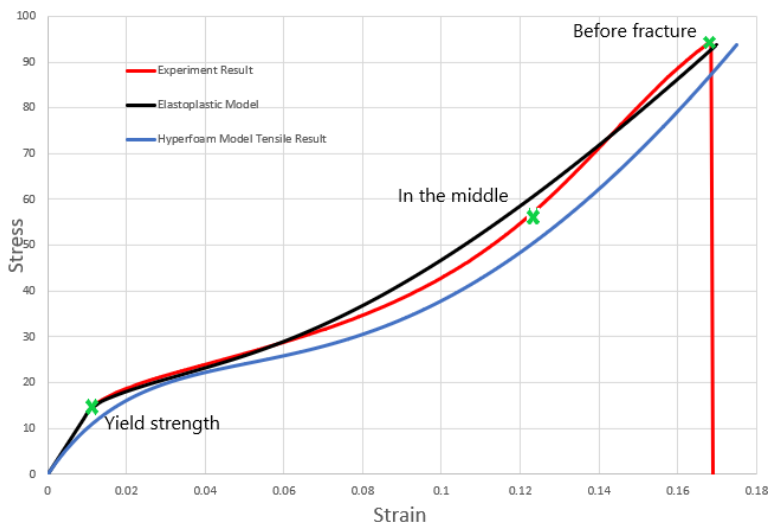
Figure 8.2: True Stress Strain: Elastoplastic, Hyperfoam Tensile vs Experiment Result

8.1.2   DMA Test

The hyperfoam model was calibrated using the Prony method, as described in Section 7.1.4.To compare the two models, both load-driven and displacement-driven models were developed. Both models exhibited a close fit with the experimental results from the Dynamic Mechanical Analysis (DMA), indicating their ability to accurately capture the viscoelastic behavior of the material.

To compare the load-driven and displacement-driven models, the Young's modulus was analyzed at various frequencies (0.01, 0.1, 1, 10, 50, and 100 Hz) using the ABAQUS software, as presented in Appendix C. This comparison specifically focuses on highlighting the differences between the load-driven and displacement-
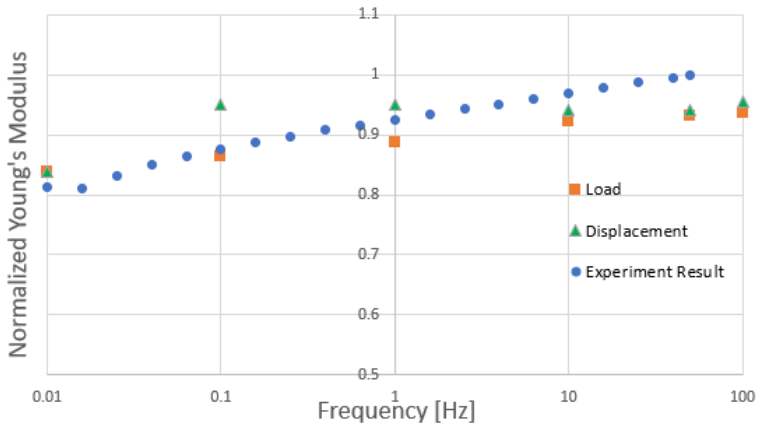
Figure 8.3: Experimental DMA vs Load-driven and Displacement-driven Models

driven models in terms of their Young's modulus predictions. By examining the results at different frequencies, insights can be gained into the distinct characteristics and performance of each model, enabling a more comprehensive understanding of their capabilities in simulating the material's behavior under different loading conditions.

8.2   Discussion

For the elastoplastic part, in Figure 8.1, a comparison of the strain distributions between the model and the specimen on the DIC software reveals a notable similarity. Figure 8.1c and 8.1f depict the state of the material just prior to fracture. Although not perfectly identical, the distributions demonstrate a close alignment of values.

In Figure 8.2, the curves exhibit a good fit, although it should be noted that the calibrated tensile simulation data consistently exceeds the experimental stress values, as shown in Figure 7.3. However, after calibration, the elastoplastic simulation results align well with the experimental curve, indicating a consistent correspondence between the strain distributions obtained from the DIC and ABAQUS software.

Regarding the viscoelasticity part, it is important to consider that the experiment in reality is load-driven. Therefore, it is expected to obtain a closer fit between the simulation and the experimental curve, as the viscoelastic behavior is better captured in load-driven tests. The load-driven, the displacement-driven and the experimental data are given together in Figure 8.3. The difference between the

load and the displacement-driven is that only have different boundary conditions in the model. Displacement is equivalent to the same mean stress.

In displacement-driven model, the displacement is under control and the deformation is imposed. The load-driven is getting amplified. The storage modulus is calculated from the result. When the load-driven is used, it is creep related. When the displacement-driven is used, it is relaxation. In the DMA test, the apparatus was load control so it has closer fit than the displacement-driven simulation. In the displacement-driven, the deformation is under control and the stress is relaxed over time because of the viscoelasticity. For the other way around, if there is load-driven, the stress will be always constant but since the material is creeping to have a constant stress, the strain needs to be increased over time. In terms of storage modulus values, the difference is small.

Chapter 9

Conclusion and Further Work

9.1 Conclusion

Finally, the results of the both simulations and the experiments fit decent on the graphs. The DMA experiments were simulated but it is not the exactly the same in reality, neither the tensile test experiment. However, they are close enough to share the comparison of the results in the Master's thesis.

In ABAQUS, there is no way to describe the behaviour and the criteria of the material completely in the available implemented material model. The reason is that if the hyperelastic model is using; there is no failure model implemented that can be combined with hyperfoam model, neither anisotropy. The elasto-plastic model can give good results with failure criteria but the elasto-plastic model can not be combined with viscoelasticity. On the other hand, the hyperfoam model can be combined with viscoelasticity but there is no failure in this model.

Finally, two models can be used to represent the material behaviour depending on the expected loading condtions.The elasto-plastic model can be used for expecting to excessive loads on the membrane, it is obvious that it will be failed and it won't go further. This is the elasto-plastic model. If there is a ULS case or a accidental load scenario on the membrane which will be experience to extreme strechting, then the elasto-plastic model can be recommended to use.

If the small cyclic loads or the deadweight loads are interested in to see on the membrane. The data will be much lower than the SLS, hyperelastic-viscoelastic model is recommended. Also, it can not have non-linear elasticity as well. The second model can take into account non-linear elasticity and viscoelasticity but no failure.

Certainly, the ABAQUS models can be modified with an UMAT code and it can be defined for all the properties together in one simulation model. Unfortunately, there is no time to use an UMAT code for the Master's thesis. The viscoelasticity can be also add to elasto-plastic model with an UMAT code but in the commercial software, there is no way to do that without an UMAT code.

The hyperfoam model was used instead of the hyperleastic model. With the hyperfoam model, a better results can be gotten on the small strains. If the graph has more point at the beginning than the optimization, the curve will be better optimized at the beginning and less at the end. To fixing this issue, more points can be added at the beginning of the curve. With the help of these additional points, a better fit for the beginning of the curve can be obtained.

Also, for the elastoplasticity, the ABAQUS software losses the anisotropic Young's Modulus and the anisotropic yield as well. The elasto-plastic model can also take this into account.

9.2 Recommendation for Further Work

Following recommendations can be taken into account for the further work:

- Bi-axial and shear tests are valuable additions to the uniaxial and DMA tests, improving the accuracy of simulations and reducing calibration time. These tests provide important data that can enhance the fit between simulated and experimental results, leading to a more comprehensive understanding of the material's mechanical behavior. Incorporating bi-axial and shear tests improves the reliability and applicability of simulations, ensuring a robust representation of the material's response to different loading conditions.

- The temperature difference can be considered for seeing the different behaviour of the membrane material on DMA test. In the this thesis, only the room temperature were used due to limited time.

- On long-term degradation of membrane structures in marine environments, it is recommended to investigate the mechanisms and rates of degradation caused by UV radiation, moisture, saltwater exposure, mechanical stresses, and biological growth. Additionally, exploring the durability of materials, effectiveness of protective coatings, and optimization of maintenance practices can contribute to developing more resilient and reliable membrane solar islands.

- Further work could involve developing a UMAT subroutine that can effectively combine elasto-plasticity and viscoelasticity in the model. This would

allow for more comprehensive and accurate simulations of materials exhibiting both types of behaviors.

- It would be valuable to consider the anisotropic behavior of the membrane material. This aspect was not accounted for in the current thesis.

Bibliography

[1] B. Philipp, R. Wüchner, and K.-U. Bletzinger, "Conception and design of membrane structures considering their non-linear behavior," in *Textiles composites and inflatable structures VI: proceedings of the VI International Conference on Textile Composites and Inflatable Structures, Barcelona, Spain. 9-11 October, 2013*, pp. 114–125, CIMNE, 2013.

[2] M. C. Beveridge, *Cage aquaculture*. John Wiley & Sons, 2008.

[3] G. Løland, "Current forces on, and water flow through and around, floating fish farms," *Aquaculture International*, vol. 1, no. 1, pp. 72–89, 1993.

[4] Y. Guo, S. Mohapatra, and C. G. Soares, "Review of developments in porous membranes and net-type structures for breakwaters and fish cages," *Ocean Engineering*, vol. 200, p. 107027, 2020.

[5] I. Collins, M. Hossain, W. Dettmer, and I. Masters, "Flexible membrane structures for wave energy harvesting: A review of the developments, materials and computational modelling approaches," *Renewable and Sustainable Energy Reviews*, vol. 151, p. 111478, 2021.

[6] Y. Guo, S. Mohapatra, and C. G. Soares, "Submerged breakwater of a flexible porous membrane with a vertical flexible porous wall over variable bottom topography," *Ocean Engineering*, vol. 243, p. 109989, 2022.

[7] J. Wang and P. D. Lund, "Review of recent offshore photovoltaics development," *Energies*, vol. 15, no. 20, p. 7462, 2022.

[8] R. Nagananthini, R. Nagavinothini, and P. Balamurugan, "Floating photovoltaic thin film technology—a review," *Intelligent Manufacturing and Energy Sustainability*, pp. 329–338, 2020.

[9] K. Trapani, *Flexible floating thin film photovoltaic (PV) array concept for marine and lacustrine environments*. PhD thesis, Laurentian University of Sudbury, 2014.

[10] S. Ferrari, "Long lasting membranes for aquaculture," Sep 2019.

[11] A. J. Nolte, J. Y. Chung, C. S. Davis, and C. M. Stafford, "Wrinkling-to-delamination transition in thin polymer films on compliant substrates," *Soft Matter*, vol. 13, no. 43, pp. 7930–7937, 2017.

[12] L. Meng and M. Wu, "Study on stress relaxation of membrane structures in the prestress state by considering viscoelastic properties of coated fabrics," *Thin-Walled Structures*, vol. 106, pp. 18–27, 2016.

[13] M. A. Tapia-Romero, M. Dehonor-Gómez, and L. E. Lugo-Uribe, "Prony series calculation for viscoelastic behavior modeling of structural adhesives from dma data," *Ingeniería, investigación y tecnología*, vol. 21, no. 2, 2020.

[14] W. Flügge, *Stresses in shells*. Springer Science & Business Media, 2013.

[15] L. P. Kollar and G. Tarjan, *Mechanics of civil engineering structures*. Woodhead Publishing, 2020.

[16] S. Z. Golroodbari and W. v. S., "Simulation of performance differences between offshore and land-based photovoltaic systems," *Progress in Photovoltaics: Research and Applications*, vol. 28, pp. 873 – 886, 2020.

[17] J. Schlaich and M. Schlaich, "Lightweight structures," *Widespan roof structures*, vol. 178, 2000.

[18] A. L. Marbaniang, S. Dutta, and S. Ghosh, "Tensile membrane structures: An overview," *Advances in Structural Engineering*, pp. 29–40, 2020.

[19] C. G. Huntington, *Tensile fabric structures: design, analysis, and construction*. American Society of Civil Engineers, 2013.

[20] R. Bradshaw, D. Campbell, M. Gargari, A. Mirmiran, and P. Tripeny, "Special structures: past, present, and future," *Journal of structural engineering*, vol. 128, no. 6, pp. 691–709, 2002.

[21] B. H. Topping and P. Iványi, *Computer aided design of cable membrane structures*. Saxe-Coburg Publications, 2008.

[22] P. Rice, "Lightweight structures: Introduction," *The Arup Journal*, vol. 15, pp. 2–6, 1980.

[23] M. Seidel, *Tensile surface structures: a practical guide to cable and membrane construction*. John Wiley & Sons, 2009.

[24] E. Ekinci, I. Nowikowa, and A. Ehrmann, "Experimental study of gluing as a joining method for garments," in *AIP Conference Series*, pp. 25–10, 2017.

[25] D. A. Grewell, A. Benatar, and J. B. Park, "Plastics and composites welding handbook," *München*, vol. 10, 2003.

[26] J. Knippers, J. Cremers, M. Gabler, and J. Lienhard, *Construction manual for polymers+ membranes: materials, semi-finished products, form finding, design*. Walter de Gruyter, 2012.

[27] A. S. of Civil Engineers, *Tensile Membrane Structures*. American Society of Civil Engineers, 2016.

[28] M. Mollaert and B. Forster, *European design guide for tensile surface structures*. TensiNet, 2004.

[29] J. BIGER, "Recommandations pour la conception des ouvrages permanents de couverture textile," *Annales du bâtiment et des travaux publics (Paris)*, no. 4, pp. 5–16, 1997.

[30] D. I. für Normung e.V. (DIN), "Air-supported structures; structure design, construction and operation," *DIN 4134*, 1983.

[31] O. M. Faltinsen and Y. Shen, "Wave and current effects on floating fish farms," *Journal of Marine Science and Application*, vol. 17, no. 3, pp. 284–296, 2018.

[32] T. Malek, *Structural and hydrodynamic analysis of a gas-filled membrane structure submerged in water*. PhD thesis, Middlesex Polytechnic, 1984.

[33] H. Moe, A. Fredheim, and O. S. Hopperstad, "Structural analysis of aquaculture net cages in current," *Journal of Fluids and Structures*, vol. 26, no. 3, pp. 503–516, 2010.

[34] E. Radzinski, "Choosing the correct raw material for aquaculture cage netting," *International Aqua Feed*, Nov 2018.

[35] K. Trapani and M. Redón Santafé, "A review of floating photovoltaic installations: 2007–2013," *Progress in Photovoltaics: Research and Applications*, vol. 23, no. 4, pp. 524–532, 2015.

[36] K. Trapani and D. L. Millar, "Floating photovoltaic arrays to power the mining industry: A case study for the mcfaulds lake (ring of fire)," *Environmental Progress & Sustainable Energy*, vol. 35, no. 3, pp. 898–905, 2016.

[37] I. Kougias, S. Szabo, F. Monforti-Ferrario, T. Huld, and K. Bódis, "A methodology for optimization of the complementarity between small-hydropower plants and solar pv systems," *Renewable Energy*, vol. 87, pp. 1023–1030, 2016.

[38] T. O. Olsen, "Fish farming in floating structures," in *WCFS2019*, pp. 191–208, Springer, 2020.

[39] T. Kristiansen and O. M. Faltinsen, "Modelling of current loads on aquaculture net cages," *Journal of Fluids and Structures*, vol. 34, pp. 218–235, 2012.

[40] A. Al-Yacouby, E. R. B. A. Halim, and M. Liew, "Hydrodynamic analysis of floating offshore solar farms subjected to regular waves," in *Advances in Manufacturing Engineering*, pp. 375–390, Springer, 2020.

[41] J. Noorzaei, S. I. Bahrom, M. S. Jaafar, W. A. M. Thanoon, and S. Mohammad, "Simulation of wave and current forces on template offshore structures," *Suranaree J Sci Technol*, vol. 12, no. 3, pp. 193–210, 2005.

[42] S. R. Massel, *Ocean waves breaking and marine aerosol fluxes*, vol. 38. Springer Science & Business Media, 2007.

[43] P. R. Thies, J. Flinn, and G. H. Smith, "Reliability assessment and criticality analysis for wave energy converters," in *Uppsala University*, Proceedings of the 8'th European Wave and Tidal Energy Conference, 2009.

[44] A. Shukla, G. Ravichandran, and Y. Rajapakse, *Dynamic failure of materials and structures*, vol. 1. Springer, 2010.

[45] M. Smith, *ABAQUS/Standard User's Manual, Version 6.9*. United States: Dassault Systèmes Simulia Corp, 2009.

[46] M. Li, K. Zhu, G. Qi, Z. Kang, and Y. Luo, "Wrinkled and wrinkle-free membranes," *International Journal of Engineering Science*, vol. 167, p. 103526, 2021.

[47] A. Sahu, N. Yadav, and K. Sudhakar, "Floating photovoltaic power plant: A review," *Renewable and sustainable energy reviews*, vol. 66, pp. 815–824, 2016.

[48] M. El-Reedy, "Offshore structure platform design," *Offshore Structures; Elsevier BV: Amsterdam, The Netherlands*, pp. 93–211, 2012.

[49] S. Oliveira-Pinto and J. Stokkermans, "Marine floating solar plants: An overview of potential, challenges and feasibility," in *Proceedings of the Institution of Civil Engineers-Maritime Engineering*, vol. 173, pp. 120–135, Thomas Telford Ltd, 2020.

[50] N. Stranghoner, Uhlemann, *et al.*, "Prospect for european guidance for the structural design of tensile membrane structures," in *Joint Research Center*, 2016.

[51] R. Houtman, "Materials used for architectural fabric structures," in *Fabric Structures in Architecture*, pp. 101–121, Elsevier, 2015.

[52] D. R. Askeland, P. P. Phulé, W. J. Wright, and D. Bhattacharya, *The science and engineering of materials*. Springer, 2003.

[53] H. Bögner-Balz, R. Blum, and J. Köhnlein, "Structural behaviour of fabrics and coatings for architectural fabric structures," in *Fabric structures in architecture*, pp. 123–157, Elsevier, 2015.

[54] A. Lyons, *Materials for architects and builders*. Routledge, 2014.

[55] S. Ferrari, "Flexible semi closed cage systems (sccs)," Sep 2018.

[56] L. Duckers, "Reinforced rubber membranes for the clam wave energy converter," in *The Ninth International Offshore and Polar Engineering Conference*, OnePetro, 1999.

[57] M. A. Meyers and K. K. Chawla, *Mechanical behavior of materials*. Cambridge university press, 2008.

[58] B. Zhao, J. Hu, W. Chen, J. Chen, and Z. Jing, "A nonlinear uniaxial stress-strain constitutive model for viscoelastic membrane materials," *Polymer Testing*, vol. 90, p. 106633, 2020.

[59] E. Wiechert, *Ueber elastische Nachwirkung...* PhD thesis, Hartungsche buchdr., 1889.

[60] J. Uhlemann, *Elastic constants of architectural fabrics for design purposes*. PhD thesis, Duisburg, Essen, Universität Duisburg-Essen, Diss., 2016, 2016.

[61] ASTM, "Standard test method for coated and laminated fabrics for architectural use," *ASTM D4851-07*, 2015.

[62] T. Shi, J. Hu, W. Chen, and C. Gao, "Biaxial tensile behavior and strength of architectural fabric membranes," *Polymer Testing*, vol. 82, p. 106230, 2020.

[63] J. Xu, Y. Zhang, Q. Yu, and L. Zhang, "Analysis and design of fabric membrane structures: A systematic review on material and structural performance," *Thin-Walled Structures*, vol. 170, p. 108619, 2022.

[64] M. E. Son, *The design and analysis of tension fabric structures*. PhD thesis, Massachusetts Institute of Technology, 2007.

[65] C. Liu and D. Glovinsky, "Secrets of longevity: How membrane properties affect long-term performance," *Journal-American Water Works Association*, vol. 112, no. 3, pp. 56–61, 2020.

[66] J. Aw, H. Zhao, A. Norbury, L. Li, G. Rothwell, and J. Ren, "Effects of poisson's ratio on the deformation of thin membrane structures under indentation," *physica status solidi (b)*, vol. 252, no. 7, pp. 1526–1532, 2015.

[67] H. Asadi, J. Uhlemann, N. Stranghoener, and M. Ulbricht, "Sensitivity assessment of pvc coated pet woven fabrics under different weathering impacts," in *Proceedings of IASS Annual Symposia*, vol. 2020, pp. 1–13, International Association for Shell and Spatial Structures (IASS), 2020.

[68] H. Asadi, J. Uhlemann, N. Stranghoener, and M. Ulbricht, "Artificial weathering mechanisms of uncoated structural polyethylene terephthalate fabrics with focus on tensile strength degradation," *Materials*, vol. 14, no. 3, p. 618, 2021.

[69] E. Yousif and A. Hasan, "Photostabilization of poly (vinyl chloride)–still on the run," *Journal of Taibah University for Science*, vol. 9, no. 4, pp. 421–448, 2015.

[70] W. J. Lewis, *Tension structures: form and behaviour*. Thomas Telford, 2003.

[71] P. Beccarelli, *Biaxial testing for fabrics and foils: Optimizing devices and procedures*. Springer, 2015.

[72] N. Group, "High-force dma gabo eplexor ht series up to 1500°c dynamic-mechanical testing systems analyzing and testing." Company Website, 2021.

[73] W. Soboyejo, *Mechanical properties of engineered materials*, vol. 152. CRC press, 2002.

Appendix A

A.1 Longitudinal Tensile Test Specimens Stress-strain Curve
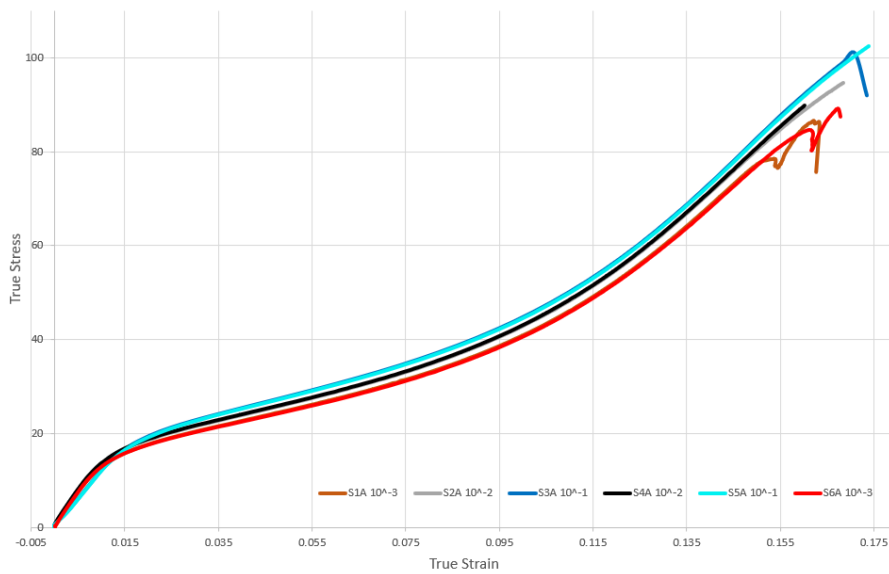
Figure A.1: Stress-Strain for all strain rates only longitudinal specimens

A.2 True vs Engineering Stress Strain Curves
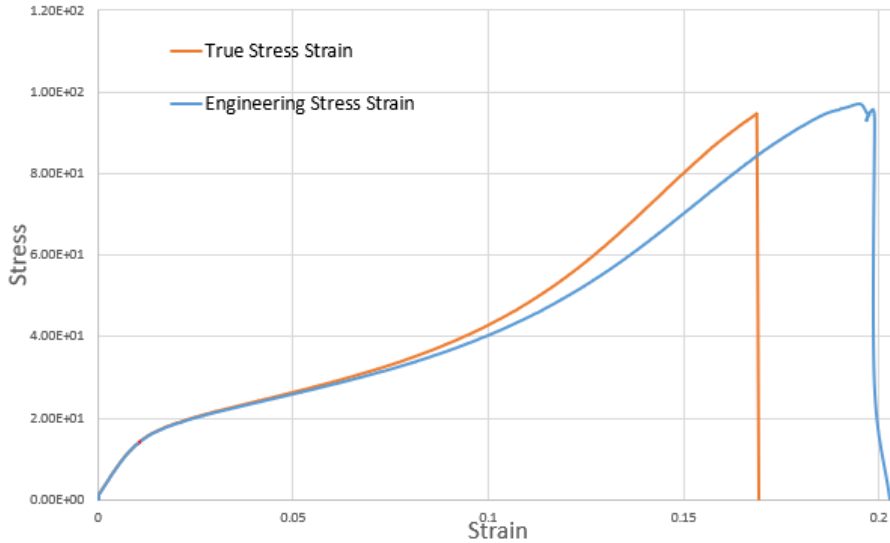
Figure A.2: True vs Engineering Stress Strain Graph for S2A Specimen

A.3 The rest of the DMA Experiment Results

Table A.1: DMA Results of the specimen S2

No	Stress Static [MPa]	L_0 [mm]	L_m [mm]	Stress Dynamic [MPa]	f [Hz]	T [^oC]	tanδ	E' [MPa]	E" [MPa]	$|E^*|$ [MPa]
1	39.8505	30.0835	34.27	2.01856	0.1	23.8609	0.048775	1.78E+03	86.67196	1.78E+03
2	39.9369	32.9175	34.6887	2.07161	0.15849	23.7395	0.050362	2.01E+03	101.3248	2.01E+03
3	39.9446	33.1673	34.8795	2.05708	0.25119	23.7702	0.046559	2.06E+03	95.9561	2.06E+03
4	39.9098	33.3142	34.9938	2.05435	0.39811	23.8461	0.04571	2.09E+03	95.46133	2.09E+03
5	39.9253	33.4106	35.0735	1.99394	0.63096	23.8459	0.044358	2.11E+03	93.50435	2.11E+03
6	39.9188	33.4778	35.1305	1.99456	1	23.7855	0.044949	2.12E+03	95.12005	2.12E+03
7	39.9382	33.5249	35.1719	2.0364	1.58489	23.8001	0.044719	2.13E+03	95.09152	2.13E+03
8	39.9614	33.5588	35.2023	2.02623	2.51189	23.8459	0.04448	2.13E+03	94.95597	2.14E+03
9	39.9549	33.5857	35.2259	2.01334	3.98107	23.8613	0.038093	2.15E+03	81.8508	2.15E+03
10	39.933	33.6055	35.2456	2.00451	6.30957	23.8761	0.038365	2.16E+03	82.98504	2.16E+03
11	39.9278	33.623	35.2602	1.99515	10	23.9064	0.041992	2.17E+03	91.27826	2.18E+03
12	39.9278	33.6417	35.2741	1.99336	15.8489	23.8917	0.043278	2.19E+03	94.59231	2.19E+03
13	39.9588	33.6487	35.2834	1.98994	25.1189	23.892	0.04654	2.19E+03	101.8594	2.19E+03
14	39.9523	33.6656	35.2901	1.9959	39.8107	23.9064	0.048709	2.21E+03	107.637	2.21E+03
15	39.9317	33.666	35.2912	2.00802	50	23.891	0.052407	2.21E+03	115.993	2.22E+03

Table A.2: DMA Results of the specimen S4

No	Stress Static [MPa]	L_0 [mm]	L_m [mm]	Stress Dynamic [MPa]	f [Hz]	T [^oC]	tanδ	E' [MPa]	E" [MPa]	$|E^*|$ [MPa]
1	9.96987	30.1351	30.4005	1.99726	0.1	24.6056	0.051347	1.14E+03	58.45031	1.14E+03
2	9.99123	30.2688	30.5113	2.01684	0.15849	24.7881	0.056483	1.12E+03	63.53638	1.13E+03
3	9.98723	30.2961	30.5447	1.99575	0.25119	24.9394	0.052998	1.14E+03	60.55546	1.14E+03
4	9.99123	30.3078	30.5588	1.99994	0.39811	24.9247	0.051645	1.16E+03	59.86334	1.16E+03
5	9.99257	30.3146	30.5661	1.99449	0.63096	24.8945	0.049897	1.17E+03	58.59046	1.18E+03
6	9.98322	30.3186	30.5705	2.00067	1	24.7892	0.049293	1.19E+03	58.56305	1.19E+03
7	10.0099	30.3195	30.5729	1.99629	1.58489	24.8185	0.048536	1.20E+03	58.29518	1.20E+03
8	9.98589	30.3216	30.5739	1.99694	2.51189	24.834	0.048289	1.21E+03	58.61155	1.22E+03
9	9.98322	30.3218	30.5743	1.99667	3.98107	24.8035	0.047383	1.23E+03	58.14758	1.23E+03
10	9.98189	30.3217	30.5743	2.0006	6.30957	24.8185	0.048703	1.24E+03	60.34709	1.24E+03
11	9.97788	30.3209	30.574	1.99295	10	24.8487	0.048878	1.25E+03	61.22758	1.25E+03
12	9.99391	30.3199	30.574	1.99095	15.8489	24.8035	0.051121	1.27E+03	64.68589	1.27E+03
13	9.98723	30.3199	30.5736	1.99102	25.1189	24.7884	0.054951	1.28E+03	70.24891	1.28E+03
14	10.0099	30.3183	30.5731	1.98595	39.8107	24.7577	0.059004	1.29E+03	76.32223	1.30E+03
15	9.97922	30.3181	30.5721	2.00649	50	24.758	0.063293	1.30E+03	82.22767	1.30E+03

Table A.3: DMA Results of the specimen S8L

No	Stress Static [MPa]	L_0 [mm]	L_m [mm]	Stress Dynamic [MPa]	f [Hz]	T [^oC]	tanδ	E' [MPa]	E" [MPa]	$|E^*|$ [MPa]
1	39.8681	30.0577	34.062	1.98879	0.01	25.0162	0.042202	1.77E+03	74.75509	1.77E+03
2	39.9378	32.9276	34.4978	1.99102	0.01585	25.32	0.042679	2.02E+03	86.38552	2.03E+03
3	39.9645	33.1568	34.6961	2.0538	0.02512	25.1528	0.040844	2.07E+03	84.73455	2.08E+03
4	39.9565	33.297	34.817	2.00224	0.03981	25.1527	0.038945	2.11E+03	81.99078	2.11E+03
5	39.9686	33.3882	34.8976	2.00624	0.0631	25.2896	0.038261	2.12E+03	81.25988	2.13E+03
6	39.9498	33.4518	34.9539	2.00739	0.1	25.3352	0.037786	2.14E+03	80.89906	2.14E+03
7	39.9418	33.4931	34.9948	2.0069	0.15849	25.32	0.038027	2.15E+03	81.75116	2.15E+03
8	39.9391	33.5295	35.0255	2.00767	0.25119	25.32	0.036835	2.16E+03	79.65034	2.16E+03
9	39.9498	33.5521	35.044	2.04489	0.39811	25.411	0.03772	2.17E+03	81.71694	2.17E+03
10	39.9404	33.5666	35.0628	2.03964	0.63096	25.3658	0.038181	2.17E+03	82.95009	2.17E+03
11	39.9378	33.5848	35.0724	2.00723	1	25.4114	0.038338	2.18E+03	83.42041	2.18E+03
12	39.9445	33.5907	35.0841	2.0376	1.58489	25.3808	0.037942	2.18E+03	82.8437	2.18E+03
13	39.9471	33.597	35.0902	2.02705	2.51189	25.3505	0.038278	2.19E+03	83.79169	2.19E+03
14	39.9364	33.6011	35.0938	2.01776	3.98107	25.32	0.033376	2.20E+03	73.45512	2.20E+03
15	39.9512	33.6072	35.0984	2.00469	6.30957	25.3347	0.033777	2.21E+03	74.66346	2.21E+03
16	39.9592	33.6091	35.1	2.01346	10	25.32	0.036413	2.22E+03	80.77122	2.22E+03
17	39.9418	33.6134	35.102	2.01344	15.8489	25.3046	0.037671	2.23E+03	83.89718	2.23E+03
18	39.9337	33.6136	35.1025	1.99291	25.1189	25.2588	0.040762	2.23E+03	90.88377	2.23E+03
19	39.9699	33.6089	35.1012	1.99151	39.8107	25.2747	0.043165	2.25E+03	97.03024	2.25E+03
20	39.9753	33.6162	35.1013	1.99454	50	25.2443	0.047206	2.25E+03	106.1236	2.25E+03

Table A.4: DMA Results of the specimen S9

No	Stress Static [MPa]	L_0 [mm]	L_m [mm]	Stress Dynamic [MPa]	f [Hz]	T [^oC]	tanδ	E' [MPa]	E" [MPa]	$|E^*|$ [MPa]
1	49.8499	30.0596	34.7703	2.00934	0.1	23.6485	0.035751	2.07E+03	74.09432	2.07E+03
2	49.9077	33.2432	35.1627	2.07279	0.15849	23.7395	0.042703	2.36E+03	100.7063	2.36E+03
3	49.9359	33.4326	35.2974	1.99337	0.25119	23.7699	0.039715	2.40E+03	95.39979	2.40E+03
4	49.944	33.5395	35.3774	2.05345	0.39811	23.8155	0.039302	2.43E+03	95.31021	2.43E+03
5	49.9292	33.6092	35.4308	1.99726	0.63096	23.8459	0.038525	2.44E+03	94.1509	2.45E+03
6	49.9251	33.6591	35.4675	2.05543	1	23.8912	0.039205	2.45E+03	96.23096	2.46E+03
7	49.9574	33.6922	35.4933	1.99894	1.58489	23.8917	0.03836	2.47E+03	94.68915	2.47E+03
8	49.9708	33.716	35.5109	2.00725	2.51189	23.9221	0.038373	2.48E+03	95.08805	2.48E+03
9	49.9735	33.7324	35.5239	2.01781	3.98107	23.891	0.031701	2.50E+03	79.098	2.50E+03
10	49.9695	33.7508	35.5358	2.0015	6.30957	23.8914	0.032088	2.51E+03	80.51884	2.51E+03
11	49.952	33.7615	35.5434	1.99382	10	23.8609	0.036058	2.52E+03	90.85354	2.52E+03
12	49.9386	33.7714	35.5502	1.99705	15.8489	23.8004	0.037105	2.53E+03	93.87286	2.53E+03
13	49.9359	33.7813	35.5512	1.99682	25.1189	23.7854	0.040345	2.55E+03	102.7287	2.55E+03
14	49.9399	33.786	35.5567	2.01281	39.8107	23.7702	0.041748	2.56E+03	106.819	2.56E+03
15	49.9601	33.7936	35.5561	1.99619	50	23.7399	0.045655	2.55E+03	116.6346	2.56E+03

Table A.5: DMA Results of the specimen S10

No	Stress Static [MPa]	L_0 [mm]	L_m [mm]	Stress Dynamic [MPa]	f [Hz]	T [^oC]	tanδ	E' [MPa]	E" [MPa]	$|E^*|$ [MPa]
1	49.866	30.0404	34.7639	2.00944	0.1	24.3479	0.035194	2.07E+03	72.90098	2.07E+03
2	49.943	33.2318	35.1629	2.07204	0.15849	24.2863	0.041958	2.36E+03	98.97845	2.36E+03
3	49.9576	33.4235	35.2997	1.99313	0.25119	24.302	0.03884	2.40E+03	93.15088	2.40E+03
4	49.9258	33.5283	35.3821	2.05119	0.39811	24.2866	0.039065	2.42E+03	94.45355	2.42E+03
5	49.9298	33.6043	35.4396	1.99637	0.63096	24.2869	0.038247	2.43E+03	93.09956	2.44E+03
6	49.9616	33.6479	35.4778	1.99314	1	24.3016	0.039088	2.44E+03	95.41199	2.44E+03
7	49.9231	33.6832	35.5046	2.00091	1.58489	24.3019	0.038193	2.46E+03	93.80156	2.46E+03
8	49.9351	33.7071	35.525	2.02828	2.51189	24.2261	0.038148	2.46E+03	94.02481	2.47E+03
9	49.951	33.7332	35.5407	2.01922	3.98107	24.2869	0.042013	2.48E+03	104.1601	2.48E+03
10	49.9417	33.7447	35.5531	2.00157	6.30957	24.2866	0.031865	2.49E+03	79.44488	2.49E+03
11	49.9351	33.7621	35.5631	1.9956	10	24.2714	0.035848	2.50E+03	89.72744	2.50E+03
12	49.9696	33.7741	35.5711	2.01565	15.8489	24.2714	0.036883	2.51E+03	92.67627	2.51E+03
13	49.9337	33.782	35.5759	1.99106	25.1189	24.2866	0.0399	2.52E+03	100.389	2.52E+03
14	49.947	33.7844	35.5784	1.99457	39.8107	24.2714	0.042264	2.54E+03	107.3427	2.54E+03
15	49.9311	33.7931	35.5808	2.00648	50	24.2563	0.045957	2.55E+03	117.0245	2.55E+03

Table A.6: DMA Results of the specimen S11L

No	Stress Static [MPa]	L_0 [mm]	L_m [mm]	Stress Dynamic [MPa]	f [Hz]	T [^oC]	tanδ	E' [MPa]	E" [MPa]	$|E^*|$ [MPa]
1	49.8587	30.0524	34.7579	2.00641	0.01	25.3654	0.034702	2.04E+03	70.79593	2.04E+03
2	49.9388	33.4662	35.2443	2.06377	0.01585	25.2899	0.039695	2.37E+03	93.92537	2.37E+03
3	49.9655	33.6638	35.4202	1.99826	0.02512	24.9706	0.037077	2.42E+03	89.88966	2.43E+03
4	49.9388	33.7813	35.5161	2.04711	0.03981	24.8945	0.035723	2.45E+03	87.47226	2.45E+03
5	49.9642	33.8555	35.5798	2.04392	0.0631	24.9553	0.0347	2.46E+03	85.53206	2.47E+03
6	49.9775	33.9096	35.624	2.00428	0.1	25.0004	0.0347	2.48E+03	86.00883	2.48E+03
7	49.9735	33.95	35.6549	2.0487	0.15849	25.0011	0.034879	2.49E+03	86.71081	2.49E+03
8	49.9468	33.9763	35.6776	2.00509	0.25119	24.8792	0.033563	2.50E+03	83.78437	2.50E+03
9	49.9482	34.0031	35.696	2.00431	0.39811	25.0162	0.034808	2.50E+03	87.10464	2.50E+03
10	49.9415	34.0185	35.708	2.04363	0.63096	25.0311	0.034941	2.51E+03	87.5896	2.51E+03
11	49.9749	34.0286	35.7174	2.00137	1	25.0768	0.035482	2.51E+03	89.02004	2.51E+03
12	49.9642	34.0345	35.723	2.03494	1.58489	24.9859	0.035357	2.52E+03	88.953	2.52E+03
13	49.9482	34.0426	35.7276	2.00807	2.51189	24.94	0.035667	2.52E+03	89.94064	2.52E+03
14	49.9709	34.0448	35.7295	2.01839	3.98107	25.0006	0.038975	2.53E+03	98.68219	2.53E+03
15	49.9268	34.0514	35.7318	2.00162	6.30957	24.9856	0.030003	2.55E+03	76.36483	2.55E+03
16	49.9428	34.0568	35.7331	2.01313	10	24.9555	0.033788	2.55E+03	86.25048	2.55E+03
17	49.9629	34.0572	35.7341	1.99866	15.8489	24.9698	0.034987	2.56E+03	89.58385	2.56E+03
18	49.9495	34.0571	35.7338	2.01551	25.1189	24.9403	0.037229	2.57E+03	95.85199	2.58E+03
19	49.9241	34.0586	35.7321	1.99985	39.8107	24.955	0.040594	2.58E+03	104.7963	2.58E+03
20	49.9375	34.0584	35.7312	1.99812	50	24.879	0.043017	2.59E+03	111.2408	2.59E+03

Table A.7: DMA Results of the specimen S12

No	Stress Static [MPa]	L_0 [mm]	L_m [mm]	Stress Dynamic [MPa]	f [Hz]	T [^oC]	tanδ	E' [MPa]	E" [MPa]	$|E^*|$ [MPa]
1	39.8629	30.0801	33.8177	2.01952	0.1	22.5996	0.042808	1.95E+03	83.50115	1.95E+03
2	39.9048	32.5905	34.1467	1.98928	0.15849	22.6607	0.044577	2.19E+03	97.54784	2.19E+03
3	39.9251	32.7866	34.2744	1.99845	0.25119	22.7059	0.041494	2.23E+03	92.65718	2.23E+03
4	39.959	32.8884	34.3445	2.05052	0.39811	22.6302	0.041415	2.26E+03	93.41402	2.26E+03
5	39.9305	32.9505	34.3903	2.04617	0.63096	22.6909	0.040829	2.27E+03	92.83067	2.28E+03
6	39.9292	32.9971	34.4215	2.00109	1	22.7062	0.04122	2.29E+03	94.21795	2.29E+03
7	39.9671	33.0261	34.4436	2.0052	1.58489	22.7518	0.040906	2.30E+03	94.05194	2.30E+03
8	39.9373	33.0503	34.4594	2.03054	2.51189	22.6909	0.041099	2.31E+03	94.88428	2.31E+03
9	39.963	33.068	34.4706	2.01856	3.98107	22.7213	0.044041	2.32E+03	102.394	2.33E+03
10	39.9454	33.0858	34.4798	2.00512	6.30957	22.7213	0.035913	2.34E+03	84.05312	2.34E+03
11	39.9373	33.0935	34.4853	1.9986	10	22.7362	0.039235	2.35E+03	92.27922	2.35E+03
12	39.936	33.1019	34.4899	2.01105	15.8489	22.7213	0.040793	2.36E+03	96.40038	2.37E+03
13	39.9522	33.1105	34.4932	2.01059	25.1189	22.6912	0.043351	2.38E+03	103.1166	2.38E+03
14	39.9603	33.1102	34.4935	1.99761	39.8107	22.7059	0.046293	2.39E+03	110.6838	2.39E+03
15	39.9698	33.1165	34.4949	2.0064	50	22.7063	0.048901	2.40E+03	117.3782	2.40E+03

Table A.8: DMA Results of the specimen S13

No	Stress Static [MPa]	L_0 [mm]	L_m [mm]	Stress Dynamic [MPa]	f [Hz]	T [^oC]	tanδ	E' [MPa]	E" [MPa]	$|E^*|$ [MPa]
1	9.98383	30.0564	30.2922	2.00422	0.1	23.4355	0.045289	1.24E+03	56.38143	1.25E+03
2	10.0013	30.1562	30.3752	1.9996	0.15849	23.5114	0.050322	1.23E+03	61.71593	1.23E+03
3	9.98786	30.1742	30.3973	2.00303	0.25119	23.5267	0.047187	1.24E+03	58.68019	1.24E+03
4	9.98249	30.1817	30.4065	1.99611	0.39811	23.5726	0.0462	1.26E+03	58.19623	1.26E+03
5	9.91672	30.1865	30.4097	1.99792	0.63096	23.6332	0.044247	1.28E+03	56.45282	1.28E+03
6	9.99188	30.1881	30.4133	1.99283	1	23.5881	0.044573	1.29E+03	57.42069	1.29E+03
7	9.97309	30.1902	30.4146	1.99747	1.58489	23.5571	0.044225	1.30E+03	57.56503	1.30E+03
8	9.99725	30.1906	30.4157	1.99728	2.51189	23.5876	0.044137	1.31E+03	58.00167	1.32E+03
9	9.98652	30.1907	30.4158	1.99576	3.98107	23.5571	0.043539	1.33E+03	57.77925	1.33E+03
10	9.92746	30.1909	30.4147	2.00149	6.30957	23.5873	0.045172	1.34E+03	60.46899	1.34E+03
11	9.98652	30.1904	30.4156	1.99263	10	23.6026	0.045968	1.35E+03	62.10586	1.35E+03
12	9.99859	30.1894	30.4151	1.99015	15.8489	23.5726	0.048294	1.36E+03	65.87443	1.37E+03
13	9.97846	30.1887	30.4145	2.0061	25.1189	23.5877	0.052744	1.38E+03	72.58861	1.38E+03
14	9.99323	30.1878	30.414	1.98985	39.8107	23.5877	0.057819	1.39E+03	80.48333	1.39E+03
15	9.91941	30.1876	30.4117	1.99252	50	23.6027	0.061034	1.40E+03	85.39126	1.40E+03

A.4   Matlab Code for Regression Study

```matlab
nInterp = 100;
lw = 2;
filename = 'regression_axial.xlsx';
[~,nSheet] = xlsfinfo(filename);
nSheet = length(nSheet);
data = cell(nSheet,1);
for i = 1:nSheet
    data(i) = {xlsread(filename,sprintf('Sheet%d',i))
        };
end
data = [data{:}];
stress = data(:,1:2:2*nSheet);
strain = data(:,2:2:2*nSheet);
strain_interp = linspace(min(strain,[],'all'),max(
    strain,[],'all'),nInterp);
stress_interp = zeros(nInterp,nSheet);
for i = 1:nSheet
    stress_interp(:,i) = interp1(strain(:,i),stress(:,
        i),...
         strain_interp,'linear','extrap');
end
mean_stress = mean(stress_interp,2);
plot(strain_interp,stress_interp,'LineWidth',1);
hold on;
plot(strain_interp,mean_stress,'red','LineWidth',lw);
hold off;
grid on;
grid minor;
% Add labels and title to the plot
xlabel('Strain');
ylabel('Stress');
title('Stress-Strain Curve');
% Add legend to the plot
legend('S2A 10E-2', 'S4A 10E-2','Regression Curve');
```

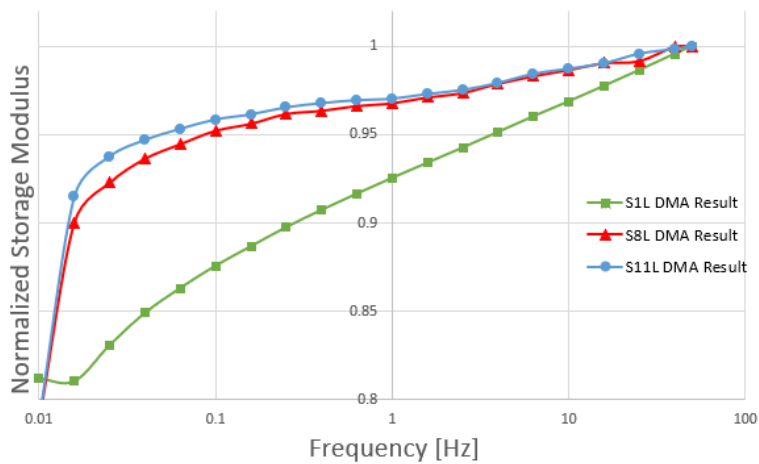## A.5 Only the Extended Frequency DMA Specimen from 0.01 to 50 Hz

Figure A.3: Extended Frequency DMA Specimens Comparison

Appendix B

B.1 Matlab Code for Prony Series

```matlab
% Define the Prony series equation
prony_eqn = @(params, f) params(1)*(1 - params(2)*(1 -
    exp(-1./(params(3)*f))) - params(4)*(1 - exp(-1./(
   params(5)*f))) - params(6)*(1 - exp(-1./(params(7)*
   f)))));

% Define the cost function for the fitting procedure
cost_fun = @(params, storage_modulus, frequency) sum((
    storage_modulus - prony_eqn(params, frequency)).^2)
   ;


% Define the file name and sheet names
file_name = 'DMTA_data.xlsx';
sheet_names = {'Sheet1', 'Sheet2', 'Sheet3'};

% Loop over the sheet names and fit the Prony series
   equation to each sheet
for i = 1:length(sheet_names)
    % Load data from the Excel file
    data = readmatrix(file_name, 'Sheet', sheet_names{
        i});
```

```matlab
    storage_modulus = data(:, 1);
    frequency = data(:, 2);

    % Define initial guesses for the fitting
        parameters
initial_params = [max(storage_modulus),  0.05, 0.075,
    0.05, 1.27, 0.11, 30];

    % Perform the fitting procedure using the '
        fminsearch' function
    fitted_params = fminsearch(@(params) cost_fun(
        params, storage_modulus, frequency),
        initial_params);

    % Display the fitted parameters for the current
        sheet
    disp(['Sheet name: ', sheet_names{i}]);
    disp(['G0 = ', num2str(fitted_params(1))]);
    disp(['g1 = ', num2str(fitted_params(2))]);
    disp(['tau1 = ', num2str(fitted_params(3))]);
    disp(['g2 = ', num2str(fitted_params(4))]);
    disp(['tau2 = ', num2str(fitted_params(5))]);
    disp(['g3 = ', num2str(fitted_params(6))]);
    disp(['tau3 = ', num2str(fitted_params(7))]);
end
```
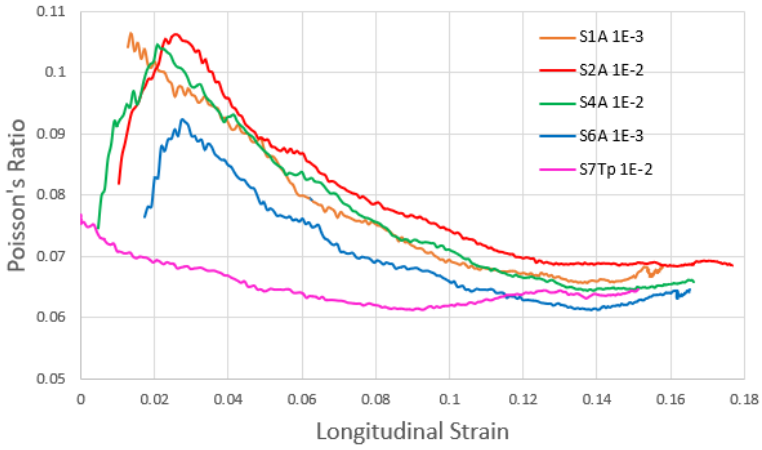
B.2 Poisson's Ratio of the material

Figure B.1: Poisson's Ratio of the some of the specimens

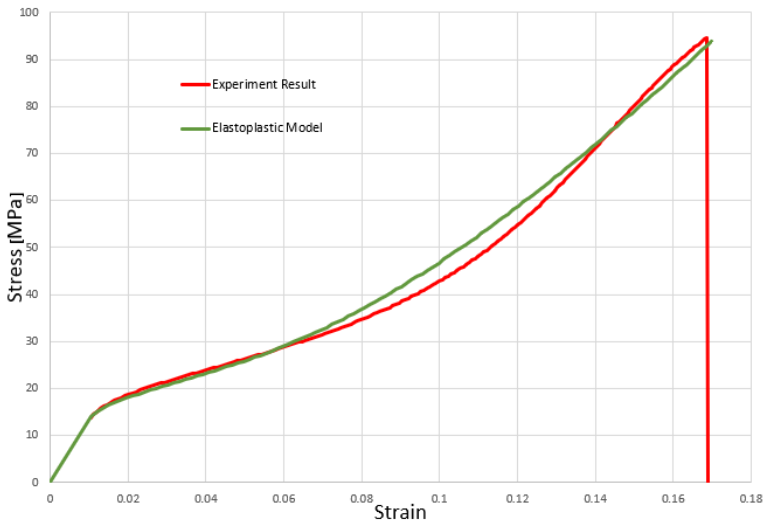## B.3 Comparison: Elastoplastic Model vs Hyperfoam Tensile vs Tensile Test Result

Figure B.2: Comparison between the elastoplastic model with the real tensile test data

B.4 The Hyperfoam Model Fitted Parameters

Table B.1: The hyperfoam coefficients from ABAQUS evaluate option

I	μ_I	α_I	ν_I
1	-1989.59	-10.14	8E-02
2	601.736	2.60	8E-02
3	2005.91	-25.00	8E-02

B.5 Prony Coefficients for S8L and S11L from the code

Table B.2: Prony series data for S8L and S11L Specimens

Specimen	S8L		S11L	
Coefficient	g_i	tau_i	g_i	tau_i
1	0.02698	0.2191	0.019211	0.074997
2	0.019259	0.015981	0.015988	0.52232
3	0.084487	44.7555	0.16286	166.3885

B.6 Storage Modulus and Frequency Data from Prony Equation

Table B.3: Prony Data from the code

S1L		S8L		S11L	
Storage Modulus	Frequency [Hz]	Storage Modulus	Frequency [Hz]	Storage Modulus	Frequency [Hz]
1051.49	0.01	1771.38	0.01	2040.12	0.01
1049.58	0.01585	2024.08	0.01585	2366.19	0.01585
1076.09	0.02512	2074.61	0.02512	2424.4	0.02512
1099.62	0.03981	2105.29	0.03981	2448.65	0.03981
1117.85	0.0631	2123.82	0.0631	2464.91	0.0631
1134.17	0.1	2140.98	0.1	2478.61	0.1
1148.38	0.15849	2149.82	0.15849	2486.02	0.15849
1162.39	0.25119	2162.37	0.25119	2496.35	0.25119
1175.03	0.39811	2166.42	0.39811	2502.42	0.39811
1186.92	0.63096	2172.53	0.63096	2506.81	0.63096
1198.46	1	2175.95	1	2508.91	1
1209.61	1.58489	2183.41	1.58489	2515.88	1.58489
1220.68	2.51189	2189.02	2.51189	2521.65	2.51189
1232.1	3.98107	2200.82	3.98107	2531.94	3.98107
1243.58	6.30957	2210.47	6.30957	2545.22	6.30957
1254.53	10	2218.2	10	2552.73	10
1265.87	15.8489	2227.09	15.8489	2560.48	15.8489
1277.47	25.1189	2229.6	25.1189	2574.67	25.1189
1289.34	39.8107	2247.9	39.8107	2581.55	39.8107
1295.12	50	2248.1	50	2585.97	50

Appendix C

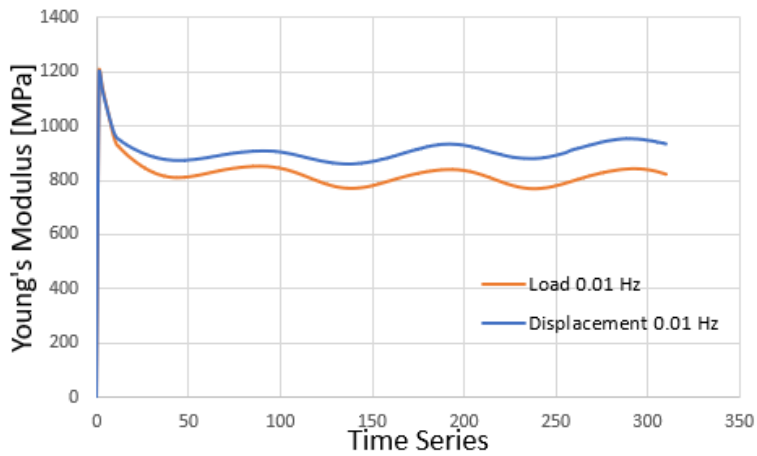## C.1 Comparison: Load-driven vs Displacement-driven Hyperfoam Models

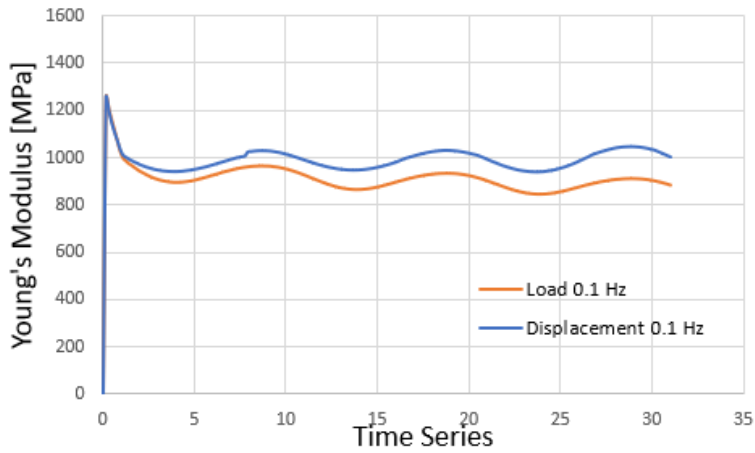**Figure C.1:** Load-driven and Displacement-driven at 0.01 Hz

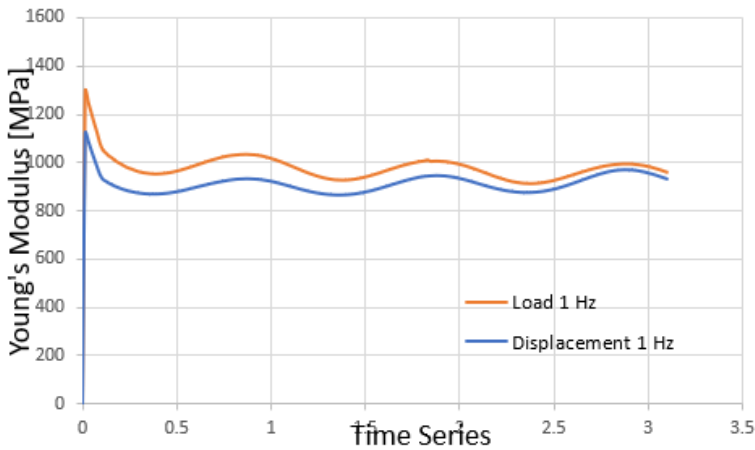**Figure C.2:** Load-driven and Displacement-driven at 0.1 Hz

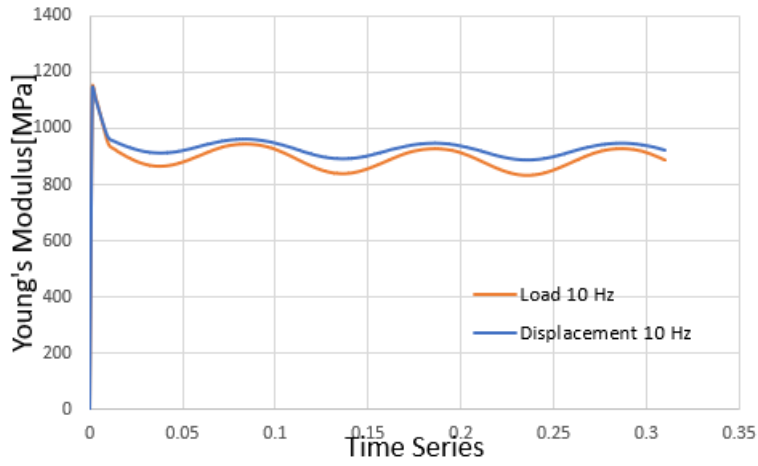

Figure C.3: Load-driven and Displacement-driven at 1 Hz

Figure C.4: Load-driven and Displacement-driven at 10 Hz

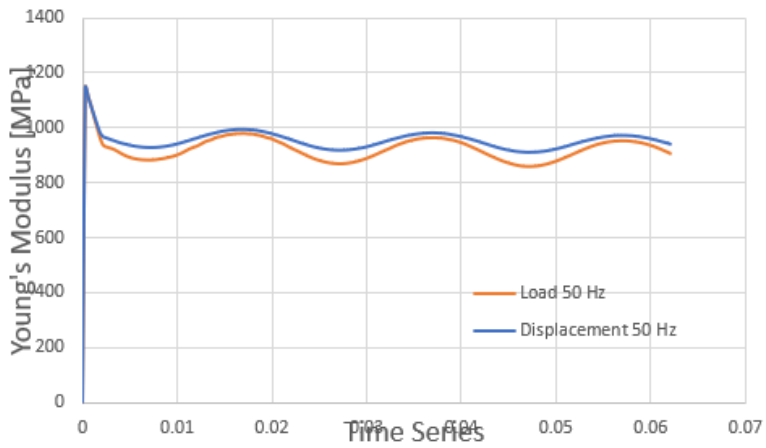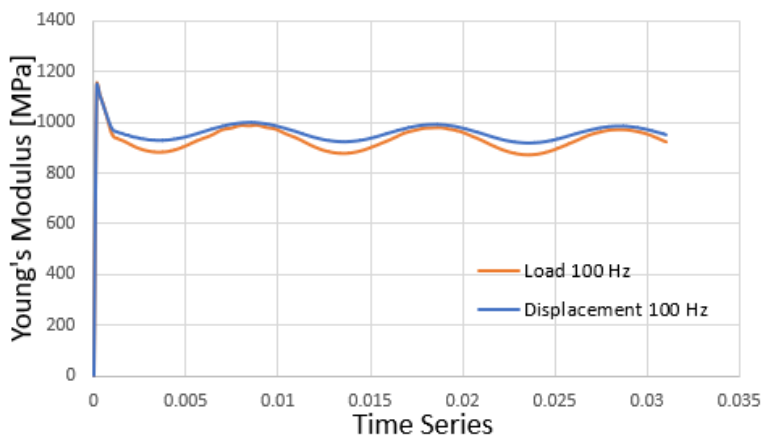**Figure C.5:** Load-driven and Displacement-driven at 50 Hz

Figure C.6: Load-driven and Displacement-driven at 100 Hz